PFC/RR-84-17 DOE/ET/51013-137

SAFETY AND PROTECTION FOR LARGE SCALE SUPERCONDUCTING MAGNETS - FY1984 REPORT

by

R.J. Thome, R.D. Pillsbury, Jr., J.V. Minervini,
J.M. Tarrh, H.D. Becker, W.R. Mann, U.R. Christensen,
M. Pelovitz, W.G. Langton, P. Rezza, and W. Beck

November 1984

Submitted to Idaho National Engineering Laboratory

TABLE OF CONTENTS

TABLE OF CONTENTS CONT.

LIST OF FIGURES

LIST OF FIGURES CONT.

LIST OF FIGURES CONT.

LIST OF TABLES

ACKNOWLEDGMENTS

The authors would like to express their appreciation to A.M. Dawson for editing and B.A. Keesler and D. Marble for report preparation.

1.0 INTRODUCTION

The Fusion Program is moving rapidly into design and construction of systems using magnets with stored energies in the range of hundreds of megajoules to gigajoules. For example, the toroidal field coil system alone for TFCX would store about 4 GJ and the mirror system MFTF-B would store about 1.6 GJ. Safety and protection analyses of the magnet subsystems become progressively more important as the size and complexity of the installations increase. MIT has been carrying out a program for INEL oriented toward safety and protection in large scale superconducting magnet systems. The program involves collection and analysis of information on actual magnet failures, analyses of general problems associated with safety and protection, and performance of safety oriented experiments. This report summarizes work performed in FY84.

In last year's report, we summarized effort in three areas that were continued this year. These are covered in Sections 2.0, 3.0 and 4.0 which present the new results, but which are self-contained for the sake of convenience.

Section 2.0 considers the parameters which influence the conversion of the stored magnetic energy to kinetic energy of ruptured components in the event of a major structural failure. Last year's specific results are summarized and were extended this year to the more general result which defines a surface in parameter space that separates systems into groups that either allow or prevent a substantial fraction of the initial stored energy to be converted to kinetic energy.* The important parameters are

*R.J. Thome, R.D. Pillsbury, Jr., W.G. Langton and W.R. Mann, "Magnetic to Kinetic Energy Conversion Following Structural Failure," presented at Applied Superconductivity Conference, San Diego, CA, September 1984.

shown to be the relative winding ultimate strength, the coupling coefficient to a secondary circuit, and the ratio of the time scale for component acceleration to the time scale for ohmic dissipation. The conclusions are: (a) a protective circuit reaction involving resistive dissipation following a major structural failure is unlikely to be effective on a fast enough time scale in high current density windings; (b) windings with low enough current densities can absorb the total load following structural failure, thus limiting the kinetic energy conversion process, although this might involve substantial yielding and deformation of the winding; and (c) protective circuits involving inductive energy transfer can respond fast enough to limit the kinetic energy conversion process in high or low current density configurations and are effective provided they are well coupled to the primary circuit.

Section 3.0 extends last year's effort in study of the advantages of protecting toroidal field coil systems with multiple circuits. The more general results* are presented in five figures and two tables which relate the maximum discharge voltages in two and three circuit systems to the coupling coefficient and relate the out-of-plane forces in a three circuit system to the number of coils in the system and the normalized major radius. A specific example based on an early TFCX TF coil design is given. The primary disadvantages of multiple circuits are the increased circuit complexity and potential for out-of-plane forces. These are offset by the substantial reduction in maximum discharge voltages, as well as other design options which become available when multiple circuits are used.

*R.J. Thome, J.M. Tarrh, R.D. Pillsbury, Jr., W.R. Mann and W.G. Langton, "Protection of Toroidal Field Coils Using Multiple Circuits," presented at Engineering Problems of Fusion Research, Philadelphia, PA, December 1983, IEEE Cat. No. 83CH1916-6 NPS, pp. 2059-2063.

Section 4.0 completes our studies relative to the structural failure of a large magnetohydrodynamic (MHD) magnet in December 1982. The event led to brittle-fracture failures in most of the structural components, significant displacements (on the order of a meter) of some of the magnet iron frame components, and similar deformation of the winding with some conductor fracture. Our FY1983 report contains a detailed description of the magnet system, a summary of the failure, and the results of a preliminary structural failure analysis. This section contains a brief introductory summary of the magnet system and cause of failure, and an update of the previous analysis to document work performed during FY1984.

A preliminary study of fault load conditions was carried out for three of the options under consideration for TFCX. The specific characteristics of the cases are defined in Section 5.0 and the alteration in electromagnetic loads under specific TF and PF fault conditions are compared. In many instances, loads are nontrivial, but are believed to be manageable through proper structural and protection circuit design. They indicate a need for ultimate specification of a list of credible faults and their consideration in the design process. Sixteen fault conditions were considered relative to usual operating conditions at the start of burn. Other points in the start-up, burn and shut-down scenario require analysis at a later stage in design and could yield fault factors which meet or exceed the ranges given. The number of conditions which require consideration is an order of magnitude larger. The process is straightforward, but tedious, and requires development of codes which can allow a large number of cases to be treated without the interactions now required for transcription and reduction of inputs and outputs.

Relatively small scale, safety-related experiments which have been conducted during FY1984 are summarized in Section 6.0. These involved tests on a small "football" shaped coil wound with a Nb_3Sn internally cooled cabled superconductor (ICCS) and tests on a sample ICCS termination. The football-shaped coil was tested to measure current, voltage, and pressure during a quench. During the tests the coil pressure was calculated to be 59 psia which is within a factor of 2 of the extrapolated maximum measured pressure of 34 psia. This indicates that a simple expression for maximum pressure rise during a quench provides a conservative estimate for cable-in-conduit conductors. In another test, an ICCS termination was fabricated and tested to investigate failure behavior due to conductor overheating. The conductor was energized to 1000 amperes at room temperature; it burned through in 3.5 seconds. The conductor failed at the weakest point in the test section. The adiabatic heating curve for copper was used to estimate the time to burnout and was found to be conservative within a factor of 2 of the actual value.

In March 1984, the FBNML experienced a major liquid helium dewar failure in a small storage dewar in one of the laboratory rooms. Section 7.0 describes the dewar failure, its probable causes, and some safety precautions that should always be taken. In addition, a basic thermodynamic analysis of dewar pressurization is given that provides insight into safe dewar operation.

Safety and protection analyses of subsystems become progressively more important as the stored energy increases with each successive generation of superconducting magnets. If the multigigajoule magnets for future

fusion facilities are to be operated reliably and safely, a thorough understanding of this area is essential. This program is contributing to this understanding through the insight gained in fundamental analyses and small scale testing.

2.0 MAGNETIC TO KINETIC ENERGY CONVERSION FOLLOWING STRUCTURAL FAILURE

R.J. Thome, R.D. Pillsbury, Jr., W.G. Langton and W.R. Mann

2.1 Foreword and Abstract

This effort was begun in FY83 and extended in FY84 to produce the more general formulation represented by Fig. 2.4. Results were prepared for presentation at the 1984 Applied Superconductivity Conference, San Diego and will appear in the Proceedings to be published by the IEEE. The contents of the paper are given in this chapter which is a self-contained summary of the FY83 and FY84 work.

A magnet failure which is potentially catastrophic in the sense that structural components fracture and the winding suffers extensive plastic deformation can be "safe" under special conditions. It may be desirable to limit operating current densities to levels at which the winding could act to limit magnetic to kinetic energy conversion. A solenoid model was used to analyze and determine the important governing parameters in the failure and discharge process. The conclusions are: (a) a protective circuit reaction involving resistive dissipation following a major structural failure is unlikely to be effective on a fast enough time scale in high current density windings; (b) windings with low enough current densities can absorb the total load following structural failure, thus limiting the kinetic energy conversion process, although this might involve substantial yielding and deformation of the winding; (c) protective circuits involving inductive energy transfer can respond fast enough to limit the kinetic energy conversion process in high or low current density configurations and are effective provided they are well coupled to the primary circuit.

2.2 Introduction

In late 1982, a massive structural failure occurred in a large MHD type magnet.[1,2] The magnet utilized about 8.4×10^4 kg of copper conductor, 5.4×10^4 kg of aluminum structure, and 5×10^5 kg of steel in a flux return frame. The failure occurred at a field level of 4.1 T and led to brittle fractures in most of the structural components, significant displacements of some portions of the iron frame, and substantial deformation of the winding with some conductor fracture. The magnet failure was catastrophic in the sense that most structural components were broken and the winding suffered extensive plastic deformation. However, operating procedures prevented possible injury to personnel and the rugged nature of the winding limited deformations to large but safe values, and restrained conversion of magnetic to kinetic energy of failed components.

Instrumentation data implied that component fracture and displacements occurred on a time scale of a few to 10's of milliseconds (which implies fractured component velocities of the order of 50 mph). Data show that status monitoring equipment initiated an automatic shutdown on a 100 ms time scale and that several manual shutdown signals were initiated within ~ 2 seconds. A fraction of the magnetic field decreased suddenly due to the flux redistribution associated with winding expansion, then remained on for 10's of seconds as the remaining energy was dissipated safely. This "remaining energy" has been estimated at $\sim 70\%$ of the initial magnetic field energy and was unavailable for conversion to kinetic energy primarily because the winding had sufficient cross section to carry the load in its deformed state without rupture while the energy dissipated resistively.

This experience is relevant to superconducting magnet design since we continually attempt to increase the winding pack current density because of cost, availability of new materials, and restrictions on space imposed by other subsystems. As we strive for high current density, we should recognize that we may be moving into a regime where the winding can no longer restrain the magnetic to kinetic energy conversion process in the event of a major structural failure. This implies the possible need for different structural design criteria for high current density designs where the winding would not be able to assume a deformed, but "fail-safe" configuration.

The following section presents an analysis of a simple model to illustrate the time scales and important parameters in the event of a major structural failure. A general plot is given which illustrates the relevance of winding cross section (current density), the ineffectiveness of resistive dissipation on a short time scale and the effectiveness of an inductively coupled secondary provided the coupling coefficient is sufficiently high. The analysis is applied to two hypothetical superconducting solenoids to illustrate the dependence on current density.

2.3 Model Description and Results

Figure 2.1 shows a long thin solenoid consisting of a coil, an external structure, and an internal passive shell which might be a winding bobbin or a secondary winding. The coil produces a magnetic field B_o within the bore and has a radial build t_c and length ℓ_o. The magnetic field produces an outward radial pressure, $B_o^2/(2\ \mu_o)$ which is reacted by hoop tension F_c in the coil and F_s in the structure. The structure is assumed to be composed of a series of alternating strong and weak links where the latter are the conceptual equivalent of fasteners, welds or other stress concentrators in the structural material.

The stress and strain in the materials are determined by a force balance, geometric compatibility, and the constitutive relations for the materials. Assume the ideal elastic/plastic stress-strain curves given in Fig. 2.2a which show the yield strengths for the structure and coil materials (σ_{wy} and σ_{cy}, respectively) and the ultimate strain capability of the coil corresponding to winding rupture (ε_u). Figure 2.2a also illustrates a typical design point without weak links ($t_w = t_s$) where the coil and structure have the same strain and operate at some fraction of their respective yield strengths. Figure 2.2b, on the other hand, shows a possible condition when links are present which are weak enough (i.e., t_w is small enough in the model) so that the links are loaded beyond yield and stretch plastically.

Assume that the coil is repeatedly charged and discharged and that, after a number of cycles, the weak links fail with the materials in the charged state, c, s and w, at time = $t = 0^-$. At $t = 0$ the entire electromagnetic load transfers to the coil and subsequent events depend

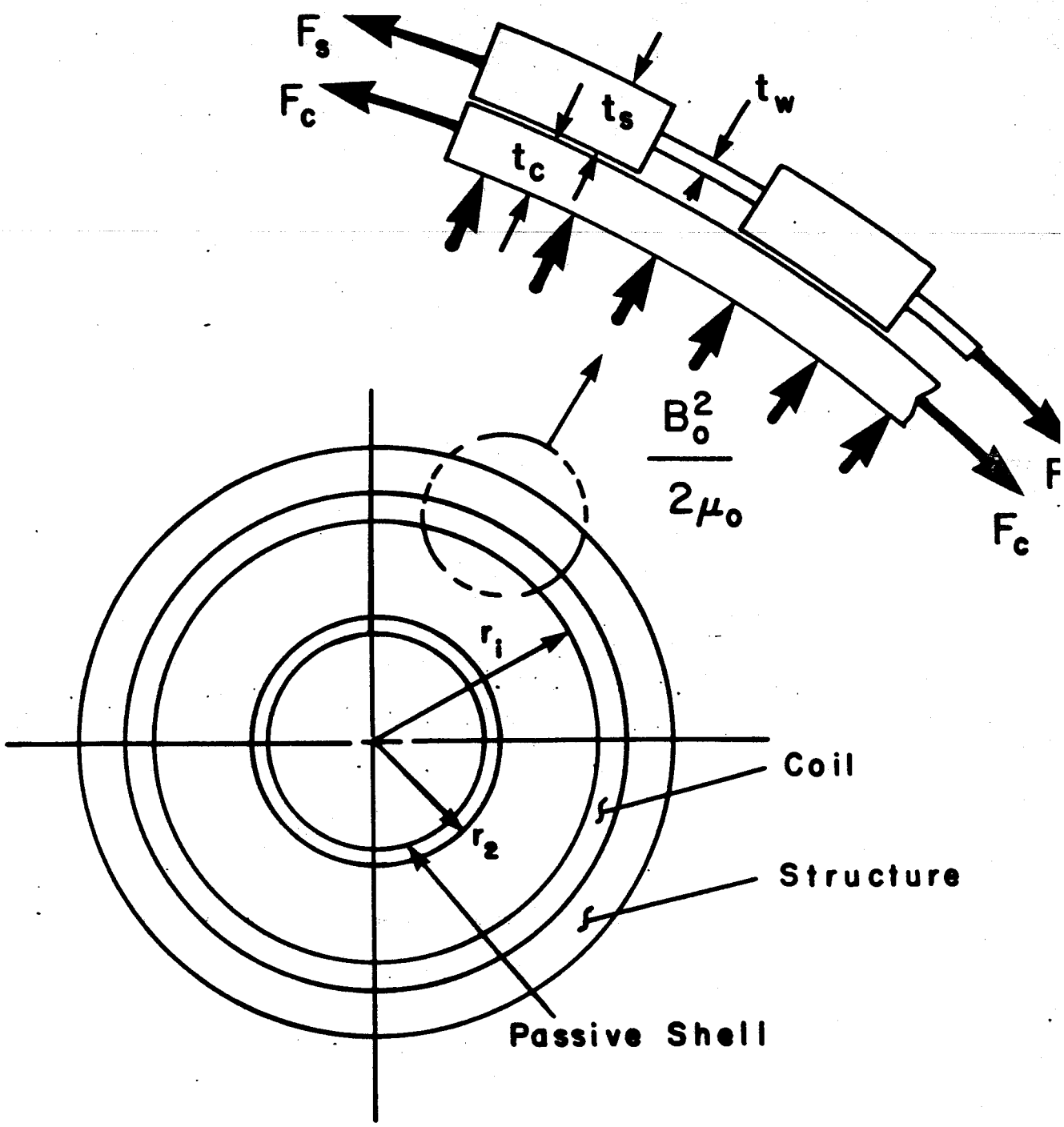

Fig. 2.1 Idealized Model of Solenoid with External Structure having Weak Links

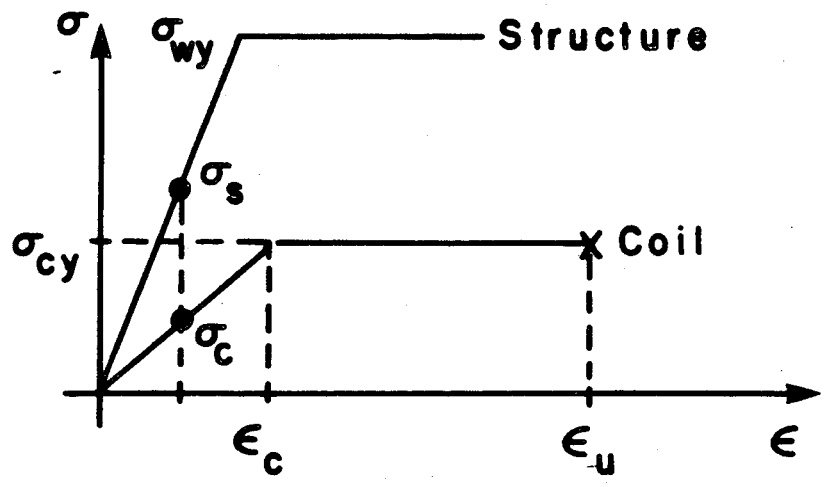

Fig. 2.2a Ideal elastic-plastic stress-strain curves for the coil and structure and typical design without "weak" links

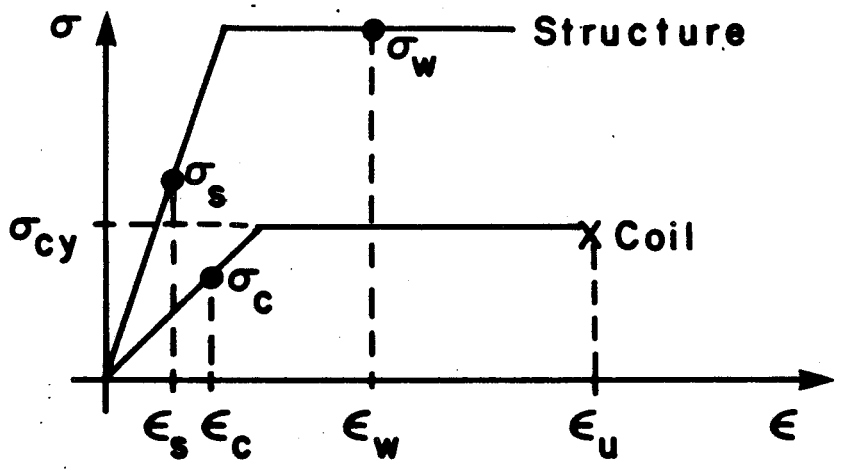

Fig. 2.2b Possible design with "weak" links

strongly on whether the load is of sufficient magnitude and maintained for a long enough time interval to strain the coil material into the plastic range and up to its ultimate strain, ε_u, at which point the coil material also ruptures. If the latter occurs, the remaining magnetic energy is available to accelerate the components outward.

For simplicity, the weak links will be assumed to break simultaneously and uniformly around the periphery. Figure 2.3 then illustrates the force balance in which the electromagnetic load is accelerating the mass outwards, but is restrained by the hoop tension in the coil. The force balance may be written as follows:

$$(B^2/2/\mu_o)\, r\, \ell_o\, d\theta + f(I_2) - 2F_{cr} \sin(d\theta/2) = (M_t\, d\theta/2/\pi)(d^2r/dt^2) \qquad (2.1)$$

where: M_t = total mass of coil and structure, $f(I_2)$ = force due to current in passive secondary winding.

As the coil expands radially, its cross section necks down such that $t_{cr} = t_c r_i/r$ where: t_c = initial coil thickness when at radius, r_i, and t_{cr} = coil thickness when expanded to a radius r.

The restraining force, F_{cr}, provided by the coil depends on whether the coil material is in the elastic range, plastic range or beyond its ultimate strain. Following the nomenclature in Fig. 2.2b, this becomes

$$F_{cr} = \begin{cases} E_c\,(r/r_i-1)\,t_c\,\ell_o, & \text{if } (r/r_i-1) < \sigma_{cy}/E_c \\ \sigma_{cy}\,t_c\,\ell_o, & \text{if } (r/r_i-1) > \sigma_{cy}/E_c \\ 0, & \text{if } (r/r_i-1) > \varepsilon_u \end{cases} \qquad (2.2)$$

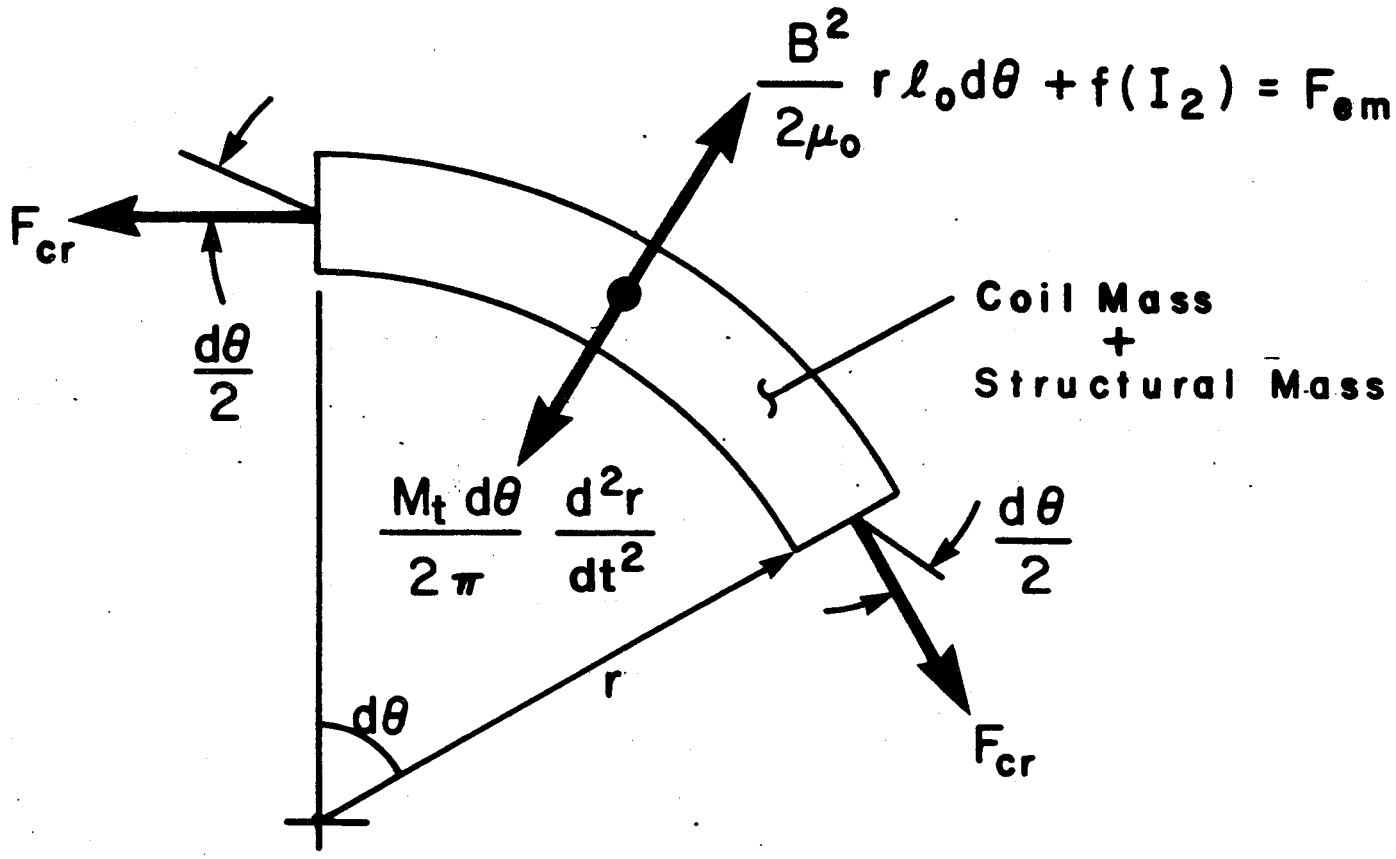

Fig. 2.3 Element of coil and structure being accelerated radially by the electromagnetic force, F_{em}, and restrained by the hoop tension, F_{cr}, in the coil.

The electromagnetic force is determined by B which is dependent on the current in the coil, the current in the secondary, and the circuit characteristics. Assume the circuit to be the coil with an initial inductance, L_o, in series with a resistor R(t) which can be later specified to characterize a superconducting coil with a discharge resistor or a conventional resistive coil. The circuit equations are given by

$$d(LI)/dt + IR(t) + d(MI_2)/dt = 0 \qquad (2.3)$$

where: M = mutual inductance between the original winding and the second circuit or electrically conducting body; I_2 = current in second circuit;

$$L_2(dI_2/dt) + d(MI)/dt + I_2R_2 = 0 \qquad (2.4)$$

where: L_2 = self inductance of second circuit; R_2 = resistance of the second circuit.

If the winding and passive shell are infinitely long, then: (a) I_2 in the shell will create no field at the coil, hence $f(I_2) = 0$ in (2.1); and (b) M is not a function of r or t. Furthermore, if the time constant for the secondary (L_2/R_2) is assumed to be long compared to the characteristic time for the transient, τ_o, then the above equations can be combined and cast in the following dimensionless form.

$$(\eta^2 - k^2)\frac{dI_n}{d\tau} + 2I_n\,\eta\,\frac{d\eta}{d\tau} + (\tau_o/\tau_d)I_n\eta^2 = 0 \qquad (2.5)$$

$$\eta\, I_n^2 - F_o\gamma = \frac{d^2\eta}{d\tau^2} \qquad (2.6)$$

where: $\eta = r/r_i$

$k^2 = M^2/(L_o L_2)$ = coupling coefficient

$I_n = I/I_o$

I_o = initial current

$\tau = t/\tau_o$

$$\tau_o = \sqrt{\frac{M_t r_i}{2 \pi r_i \ell_o B_o^2/(2 \mu_o)}}$$

L_o = initial inductance of coil

R_o = characteristic resistance = L_o/τ_o

$\tau_d = L_o/R_i$

R_i = initial coil resistance

$$\gamma = \begin{cases} E_c/\sigma_{cy} (\eta - 1) & \text{if } (\eta - 1) < \sigma_{cy}/E_c \\ 1 & \text{if } (\eta - 1) > \sigma_{cy}/E_c \\ 0 & \text{if } (\eta - 1) > \varepsilon_u \end{cases}$$

$$F_o = \frac{\sigma_{cy} t_c \ell_o}{\left(\frac{B_o^2}{2\mu_o}\right) r_i \ell_o}$$

The independent variable in Eqs. (2.5) and (2.6) is τ, the normalized time; the dependent variables are η, the normalized radius, and I_n, the normalized current; τ_d is the characteristic discharge time for the coil alone; γ is a function of η which determines if the restraining force supplied by the coil is in the elastic or plastic range or if the coil has been strained beyond rupture. F_o is a parameter determined by the characteristics of the coil structural system. It is a measure of the maximum load carrying capabilities of the coil at yield relative to the initial magnetic load. The characteristic time, τ_o, is a measure

of the time required to accelerate the entire mass of the system a distance r_i under the unrestrained action of the total magnetic force initially available.

The governing equations are nonlinear, but can be written in finite difference form and integrated forward in time to determine I_η and η. The initial conditions ($\tau = 0$) are that $I_\eta = 1$, $\eta = 1 + \varepsilon_c$ and $d\eta/d\tau = 0$. Note that the character of the system response will be critically dependent on: (a) the magnitude of F_0, because $F_0 > 1$ implies that the winding has sufficient strength without structure to carry the entire initial load without yield; (b) k^2, because this determines the amount of the initial stored energy which is trapped by the secondary and is unavailable for conversion to kinetic energy even if rupture occurs; and (c) (τ_0/τ_d) because this governs the rate of energy dissipation in the coil circuit and thus reduces the amount available for further winding deformation and/or conversion to kinetic energy.

Once σ_{cy}/E_c and ε_u are selected we would like to choose F_0, k^2 and (τ_0/τ_d) such that the coil would not strain beyond ε_u even if the structure failed. The surface separating final conditions with strain $< \varepsilon_u$ from those with strain $> \varepsilon_u$ for the thin solenoid model is given in Fig. 2.4 which is based on $\varepsilon_u = 0.2$ and $E_c/\sigma_{cy} = 900$ (the latter is considered typical for a winding composite). In this figure, a system with a point, F_0, k^2, (τ_0/τ_d), which lies inside the surface will have its winding strained beyond ε_u and ruptured following structural failure whereas a system whose point lies outside the surface will not exceed ε_u. In the latter case, the winding may or may not deform plastically depending on the location of the point, but the design point is "safe" in that the magnetic

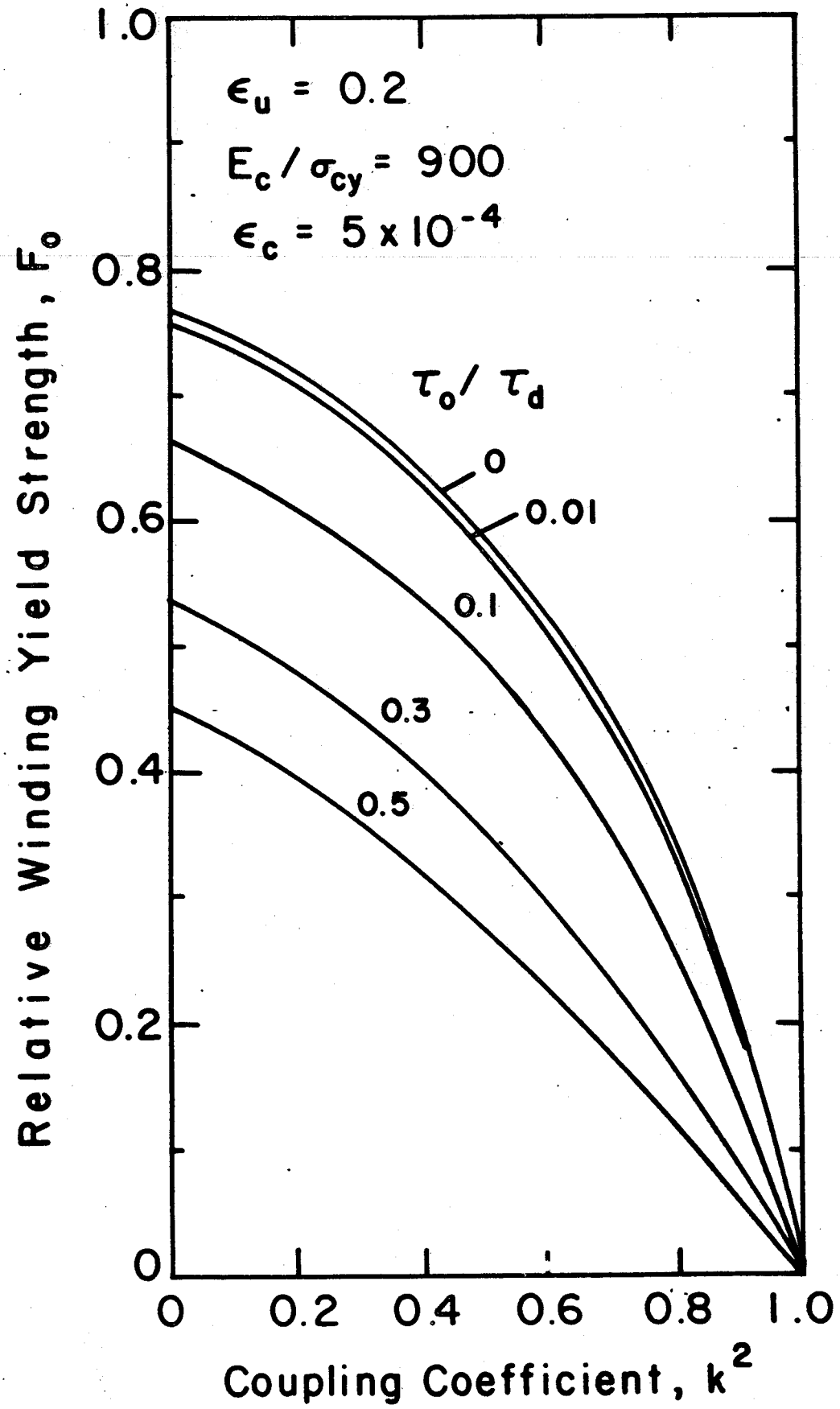

Fig. 2.4 Surface in [F_o, k^2, (τ_o / τ_d)] space for an infinite solenoid; windings will not rupture for design points outside the surface even if the structure fails.

energy will not be converted to kinetic energy of fractured winding components. If the secondary is present ($k^2 \neq 0$) then it must, of course, be capable of carrying the load associated with the magnetic energy it traps.

Figure 2.4 shows that an F_0 less than 1 is still acceptable even if k^2 and $(\tau_0/\tau_d) = 0$ because of the energy absorption capability of the winding as it deforms. This value will depend on E_c/σ_{cy} and ε_u. It also shows that (τ_0/τ_d) must be greater than about 0.1 in order for resistive dissipation to have a significant impact. Since τ_0 may be expected to be of the order of 10 ms, this implies a required discharge time constant of the order of 100 ms with zero reaction delay. In a large system, a discharge at that rate would probably correspond to an unacceptably high voltage. As a result we conclude that resistive dissipation cannot be considered a primary means for justifying a design at reduced F_0. Inductive coupling to a secondary, on the other hand, reacts virtually instantaneously and is effective provided the coupling coefficient is sufficiently high.

The difference in system behavior can be illustrated with the two hypothetical cases in Table 2.1 which have the same initial field and bore size but different winding current densities. Case 1 is for a moderate to high current density and Case 2 is for a high current density. They lead to substantially different values for t_c. The structural build, t_s, is based on a stress $\sigma_s = 2.76 \times 10^8$ N/m^2 (4×10^4 psi). The total mass is that of the structure based on a steel density of 7.8×10^3 kg/m^3 and the winding based on 8.9×10^3 kg/m^3 with a packing factor of 0.7 applied to the latter. If an operating current level of 2×10^4 A is chosen then the inductance and stored energy per unit length can be shown to be 0.625 H/m

TABLE 2.1

HYPOTHETICAL SOLENOID CHARACTERISTICS

CASE	1	2
Magnetic Field, [T]	10	10
Bore Radius, [m]	1.0	1.0
Winding Current Density, $[10^7 A/m^2]$	1.86	3.3
Winding Radial Build, t_c [m]	0.482	0.241
Structural Build, t_s [m]	0.182	0.168
Total Mass Per Unit Length, M/ℓ_o, [kg/m]	3.39×10^4	2.51×10^4
Operate Current, [kA]	20	20
Inductance Per Unit Length, L_o/ℓ_o, [H/m]	0.625	0.625
Stored Energy Per Unit Length, E/ℓ_o, [J/m]	1.25×10^8	1.25×10^8
Winding Modulus/Yield Stress, E_c/σ_{cy}	900	900
Winding Strain, ε_c	5×10^{-4}	5×10^{-4}
Characteristic Time, τ_o [s]	1.17×10^{-2}	9.28×10^{-3}
Relative Winding Strength, F_o	1.0	0.562
Winding Ultimate Strain, ε_u	0.2	0.2

and 125 MJ/m, respectively. The ratio of winding modulus to yield strength was assumed to be 900 and the ultimate winding strain at fracture was assumed to be 20%. In both cases the initial strain in the winding at the operating current level was taken as 5×10^{-4}. The characteristic time, τ_o, is about 10 ms for each case. This is representative of the time required for the magnetic energy to accelerate the system mass and is quite rapid. The yield stress for the winding was assumed to be $\sigma_{cy} = 0.7 (2 \times 10^4) = 1.4 \times 10^4$ psi. This value, together with some of the characteristics found earlier, allow F_o to be found. Since it is unity for Case 1 and substantially less than one for Case 2, we expect different responses in the event of a structural failure. Case 1 may be shown to deform plastically, but, because $F_o = 1$, the winding will not rupture even if $k^2 = 0$ and $(\tau_o/\tau_d) = 0$ and it is, therefore, "safe."

Figures 2.5, 2.6 and 2.7 show the response for Case 2 following a structural failure at t = 0. The abscissa in each figure is time normalized to τ_o. Figure 2.5 shows the current in the coil normalized to the initial current and the transient which results for four different values of (τ_o/τ_d). The case of $(\tau_o/\tau_d) = 0$ corresponds a zero resistance situation and increasing (τ_o/τ_d) implies circuitry with successively larger resistances (quench or dump resistors). Note that the transient is well underway in only two times the characteristic time, τ_o. The normalized radial displacement is shown in Fig. 2.6 over the same time period and illustrates substantially different reactions depending on the value of (τ_o/τ_d). Higher values of (τ_o/τ_d) generate a condition where sufficient energy is dissipated rapidly enough in the resistance to limit the deformation. However, low values result in a deformation which is

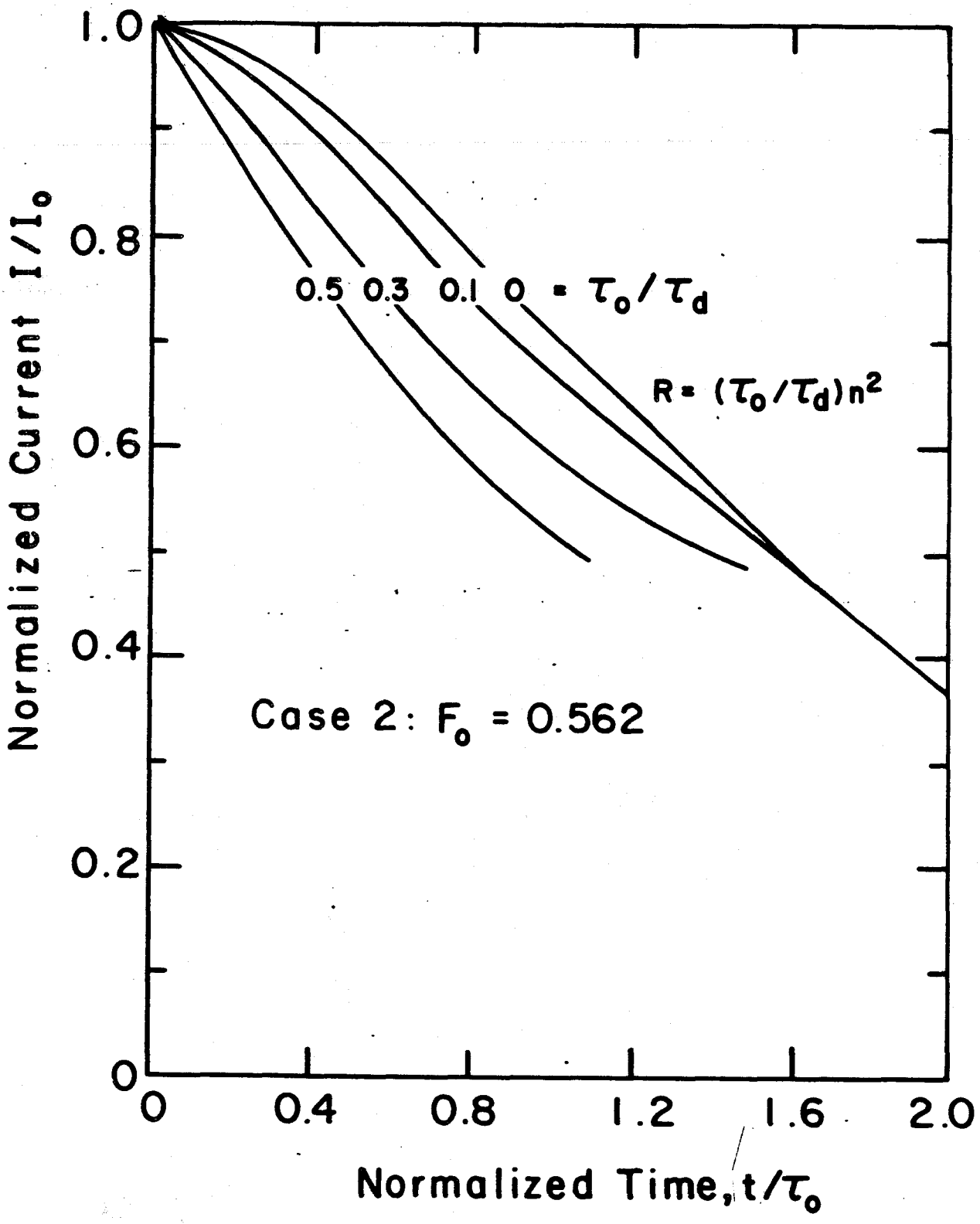

Fig. 2.5 Normalized current vs time for Case 2 and selected values of (τ_o / τ_d).

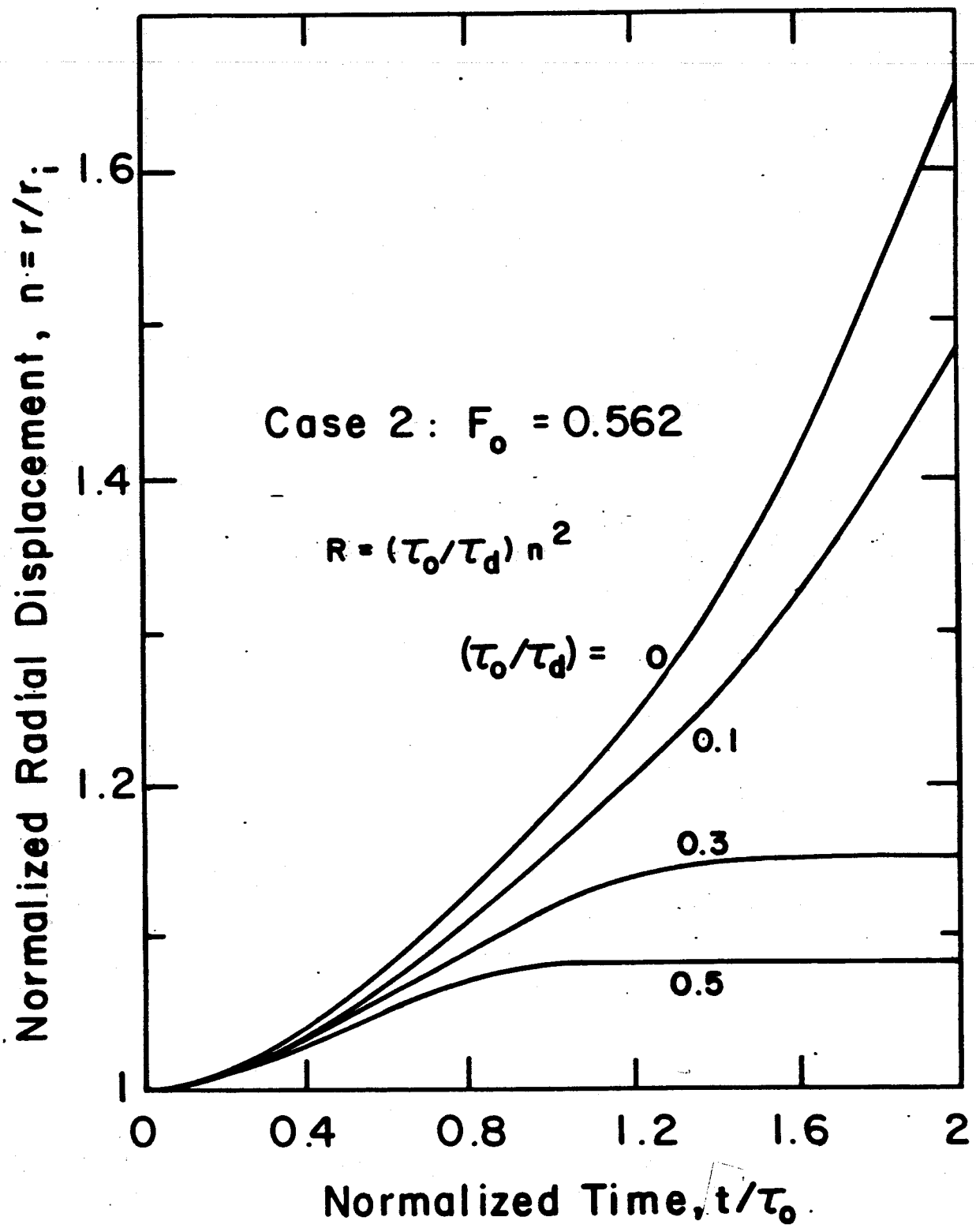

Fig. 2.6 Normalized radial displacement vs time for Case 2 and selected values of (τ_o/τ_d).

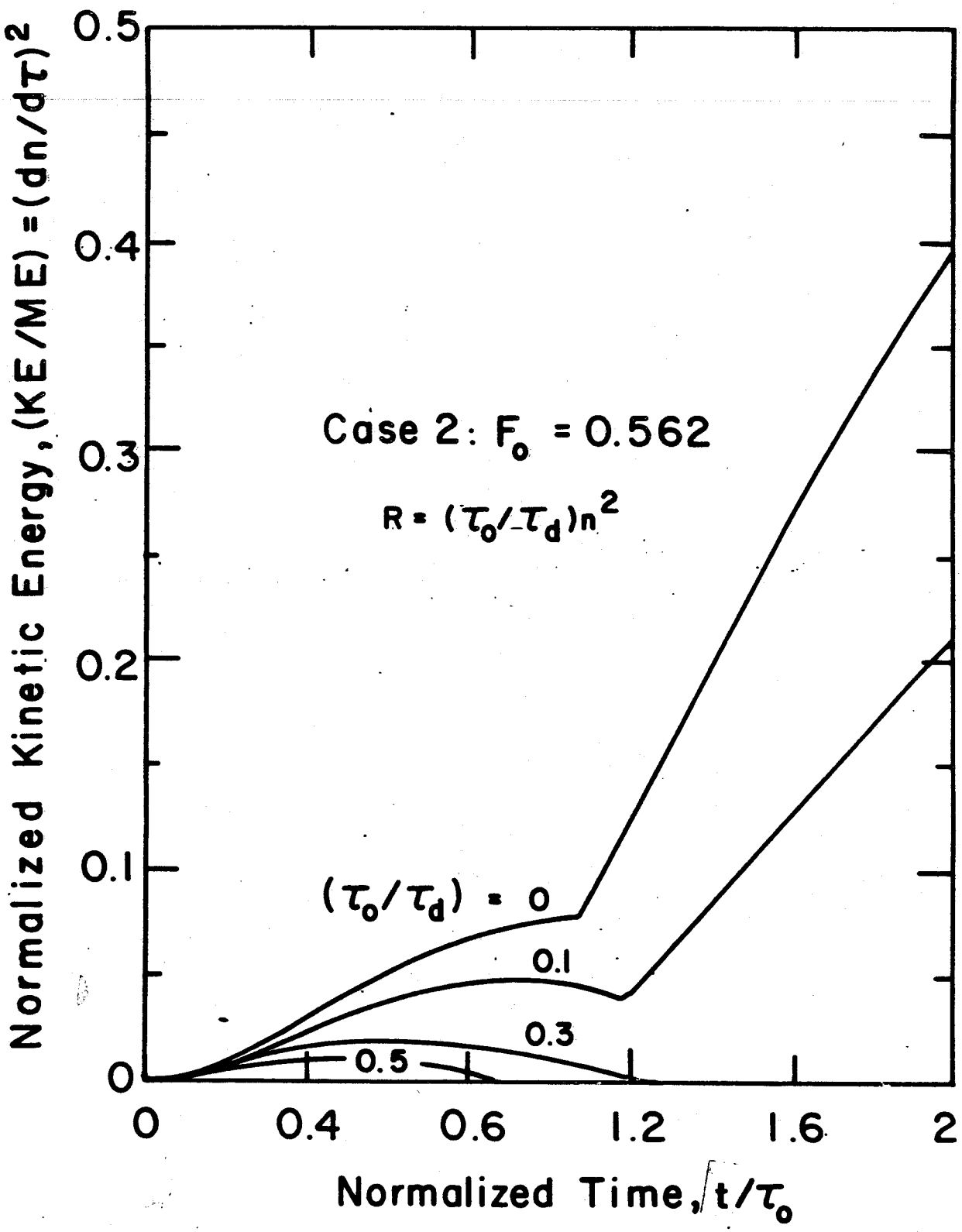

Fig. 2.7 Normalized kinetic energy vs time for Case 2.

not limited. The critical condition occurs when the ultimate winding strain, ε_u, is exceeded. In these examples, $\varepsilon_u = 0.2$; therefore, if conditions are such that $\eta \approx 1 + \varepsilon_u \approx 1.2$ we would expect the winding to rupture and no restraint on conversion of the remaining magnetic energy to kinetic. This is shown in Fig. 2.7 which is a plot of the instantaneous kinetic energy per unit length normalized to the magnetic energy per unit length initially stored at $t = 0^-$. For high enough (τ_0/τ_d) the kinetic energy starts at zero, rises to a maximum and decreases to zero. However, if the energy is not dissipated fast enough, that is, if (τ_0/τ_d) is low enough, then the coil ruptures and the unrestrained magnetic to kinetic energy conversion occurs. Note that the sudden change in slope in Fig. 2.7 occurs at the time when the radial displacement in Fig. 2.6 passes through $\eta \approx 1.2$ where the ultimate winding strain is exceeded.

Case 2 illustrates that the unrestrained conversion of magnetic to kinetic energy can be averted even if $F_0 < 1$, provided the usual discharge time constant is of the same order as τ_0. In many cases, however, this would require unrealistically high voltages and unrealistically fast circuit response times since τ_0 is likely to be small. As a result we suspect that in many cases, a response involving resistive dissipation alone is not feasible. The inductive initiation of current in a secondary, however, can occur virtually instantaneously provided $L_2/R_2 >> \tau_0$. If the coupling coefficient to the secondary were high enough, then the winding would not strain beyond ε_u even if $(\tau_0/\tau_d) = 0$ and $F_0 <= 1$. As an example, Fig. 2.4 shows that winding rupture for Case 2 and $(\tau_0/\tau_d) = 0$ will not occur provided $k^2 > 0.54$. The secondary must of course be able to carry the load associated with the magnetic energy it traps.

2.4 Conclusions

Although the geometry in the previous section is simple it allows the important parameters to become apparent and the following conclusions to be drawn: (a) a protective circuit reaction involving dissipation in resistive elements following a major structural failure is unlikely to be effective on a fast enough time scale to limit the magnetic to kinetic energy conversion process in magnets using high current density windings; (b) protective circuits involving inductive energy transfer can respond fast enough to limit the kinetic energy conversion process in high or low current density configurations and can be effective if the coupling coefficient is high enough; (c) windings with low enough current densities can absorb the total load following structural failure, thus limiting the kinetic energy conversion process, although this might involve substantial yielding and deformation of the winding.

We would expect that the pressures exerted by the desire for cost reduction together with our developing knowledge of how to build windings which are less (cryo-)stable will drive us into higher current density designs. We should also recognize that this may eventually move us into a regime where structural design criteria should be different from cases where the winding itself has enough cross section to be much more "fail-safe."

2.5 References for Chapter 2

1. H. Becker, J.M. Tarrh and P.G. Marston, "Failure of a Large Cryogenic MHD Magnet", Journal de Physique, Colloque C1, Tome 45, January 1984.

2. R.J. Thome, J.M. Tarrh, R.D. Pillsbury, et al., "Safety and Protection of Large Scale Superconducting Magnets -- FY83 Report", PFC/RR-83-33, December 1983.

3.0 PROTECTION OF TOROIDAL FIELD COILS USING MULTIPLE CIRCUITS

R.J. Thome, J.M. Tarrh, R.D. Pillsbury, Jr., W.R. Mann and W.G. Langton

3.1 Foreword and Abstract

This effort was begun in FY83 and extended in FY84 to produce the more general results given in Figures 3.1-3.5 and Tables 3.1-3.2. Methods were also applied to an early version of TFCX and are given in Figure 3.6 and Table 3.3. These results were presented at the Engineering Problems of Fusion Research Conference in Philadelphia, PA, December 1983 and published in the proceedings for that conference. The contents of the paper are given in this chapter which is a self-contained summary of the FY83 and FY84 work.

The protection of toroidal field (TF) coils using multiple circuits is described. The discharge of a single-circuit TF system is given for purposes of definition. Two-circuit TF systems are analyzed and the results presented analytically and graphically. Induced currents, maximum discharge voltages, and discharge time constants are compared to the single-circuit system. Three-circuit TF systems are analyzed. In addition to induced currents, maximum discharge voltages, and time constants, several different discharge scenarios are included. The impact of having discharge rates versus final maximum coil temperatures as requirements are examined. The out-of-plane forces which occur in the three-circuit system are analyzed using an approximate model. The analysis of multiple circuit TF systems is briefly described and results for a Toroidal Fusion Core Experiment (TFCX) scale device are given based on computer analysis.

The advantages and disadvantages of using multiple-circuit systems are summarized and discussed. The primary disadvantages of multiple circuits are the increased circuit complexity and potential for out-of-plane

forces. These are offset by the substantial reduction in maximum discharge voltages, as well as other design options which become available when using multiple circuits.

3.2 Discharge of Single-Circuit Systems

Consider first a single-circuit TF coil system, for purposes of definition. Let there be a total of 2N TF coils connected in series, having a total inductance L_0 and carrying an initial current i_0. If the initial total magnetic stored energy $E_0 = L_0 i_0^2/2$ is discharged into a resistance R_0, then the current will exponentially decay to zero from its initial value of i_0 with a time constant τ_0 equal to L_0/R_0. The maximum discharge voltage for this case is given by $V_0 = i_0 R_0$, which occurs at the beginning of the transient. This can be expressed as

$$V_0 = i_0(L_0/\tau_0) = \frac{2E_0}{i_0\tau_0} \qquad (3.1)$$

If the discharge is initiated to limit the joule heating and consequent temperature rise which would occur during a coil quench, the final maximum conductor temperature T_f can be determined, dependent on the detailed assumptions that are made. To simplify the analysis and presentation of the results, it is assumed that the local heating is adiabatic, that the resistance of the normal region is small compared to the resistance of the discharge resistor, and that there is no delay time between the initiation of local heating and the discharge transient. With these assumptions, it can be shown [1] that for a given conductor, the following condition will result in the same final maximum conductor temperature, T_f.

$$i_0^2\tau_0 = \text{constant} \qquad (3.2)$$

For example, (3.2) states that if an initial current greater than i_0 is used, the discharge time constant τ_0 must be reduced (by increasing R_0) to maintain the same final maximum conductor temperature.

3.3 Discharge of Two-Circuit Systems

Consider the same system of 2N TF coils described in the previous section. However, assume that alternate coils are now connected in two separate circuits such that the first, third, fifth,.., 2N-1st coils comprise the first circuit while the second, fourth, sixth,.., 2Nth coils comprise the second circuit . If both circuits carry an initial current i_0, then prior to a discharge the conditions are identical to those of the single-circuit system. However, if the first circuit of the two-circuit system is discharged while the second circuit remains charged, the discharge characteristics are very different from those of the single-circuit system.

The first characteristic to consider is the distribution of currents. If the first circuit is discharged, the current in the second circuit will increase to maintain constant flux linkage. Using elementary circuit theory, it can be shown that when the first circuit is fully discharged, the current in the second circuit will have increased by a factor (1+k), where

$$k = M_{12}/(L_1 L_2)^{1/2} = M/L \qquad (3.3)$$

since $M_{12} = M_{21} = M$ and $L_1 = L_2 = L$ because each circuit has an equal number of identical coils. The parameter k is the familiar coupling coefficient, which can range in value from 0 to 1. Thus if there is no inductive coupling, $M = 0$, $k = 0$, and the current in the second circuit is

unchanged by the discharge of the first circuit.

However, if strong coupling exists, the current in the second circuit can be increased significantly. Depending on design details, the increased current can be used to drive the conductors in the coils of the second circuit beyond their critical current values, forcing them to go normal. An evaluation would be required for a specific design to determine whether the ability to initiate normal regions and distribute the energy dissipation more uniformly throughout the system would be favorable under selected fault conditions.

The second critical discharge characteristic to consider is the maximum voltage to which the coils would be subjected, in comparison to V_0 in (3.1). Because the maximum voltage depends on the value of the discharge resistance chosen, two cases are of interest. For the first case, the discharge resistances are chosen to yield the same time constant τ_0 for the discharge transient as the single-circuit system. For the second and more appropriate case, the discharge resistances are chosen to yield the same final maximum conductor temperature, in accordance with the condition expressed by (3.2).

For the first case of having the same time constant τ_0 for the discharge transient, it can be shown by using elementary circuit theory that the maximum voltage for the first circuit discharged is equal to $V_0(1-k)/2$. Thus the maximum voltage required to discharge the first of two circuits is less than half of that which would be required to discharge the system if it were connected in a single circuit. This is because less than half the total energy must be removed as a result of the inductive coupling. In fact, it can be shown that the fractional energy dissipated is equal

to the normalized maximum discharge voltage for the first circuit. This can be expressed as

$$(E_0 - E)/E_0 = V/V_0 \qquad (3.4)$$

where E is the energy remaining after discharge of the first circuit.

If the second circuit was discharged with the same time constant τ_0, the required maximum voltage would be $V_0/2$. This is assumed to occur after the first circuit is fully discharged and opened so that there is no induced current during discharge of the second circuit. The option of leaving the first circuit closed will be considered in future work.

The case which requires the same final maximum conductor temperature, T_f, is a more appropriate design condition. It can be shown that the maximum voltage for the first circuit discharged is equal to $V_0(1-k)/2$, the same as in the first case. This is shown plotted as the Circuit 1 curve in Fig. 3.1, where the maximum discharge voltage is normalized to V_0. Note that this curve also represents the fractional energy dissipated.

However, when discharging the second circuit, a smaller discharge time constant is required to limit the temperature rise. A higher maximum voltage of $V_0(1+k)^2/2$ is therefore required. This is shown plotted as the Circuit 2 curve in Fig. 3.1, again normalized to V_0. As shown in the figure, this may be either greater than or less than the maximum voltage required for discharge of the single-circuit system, depending on k. The time constant for this case is given by $\tau_0/(1+k)^2$.

A summary of the discharge characteristics for the two-circuit system is given in Table 3.1.

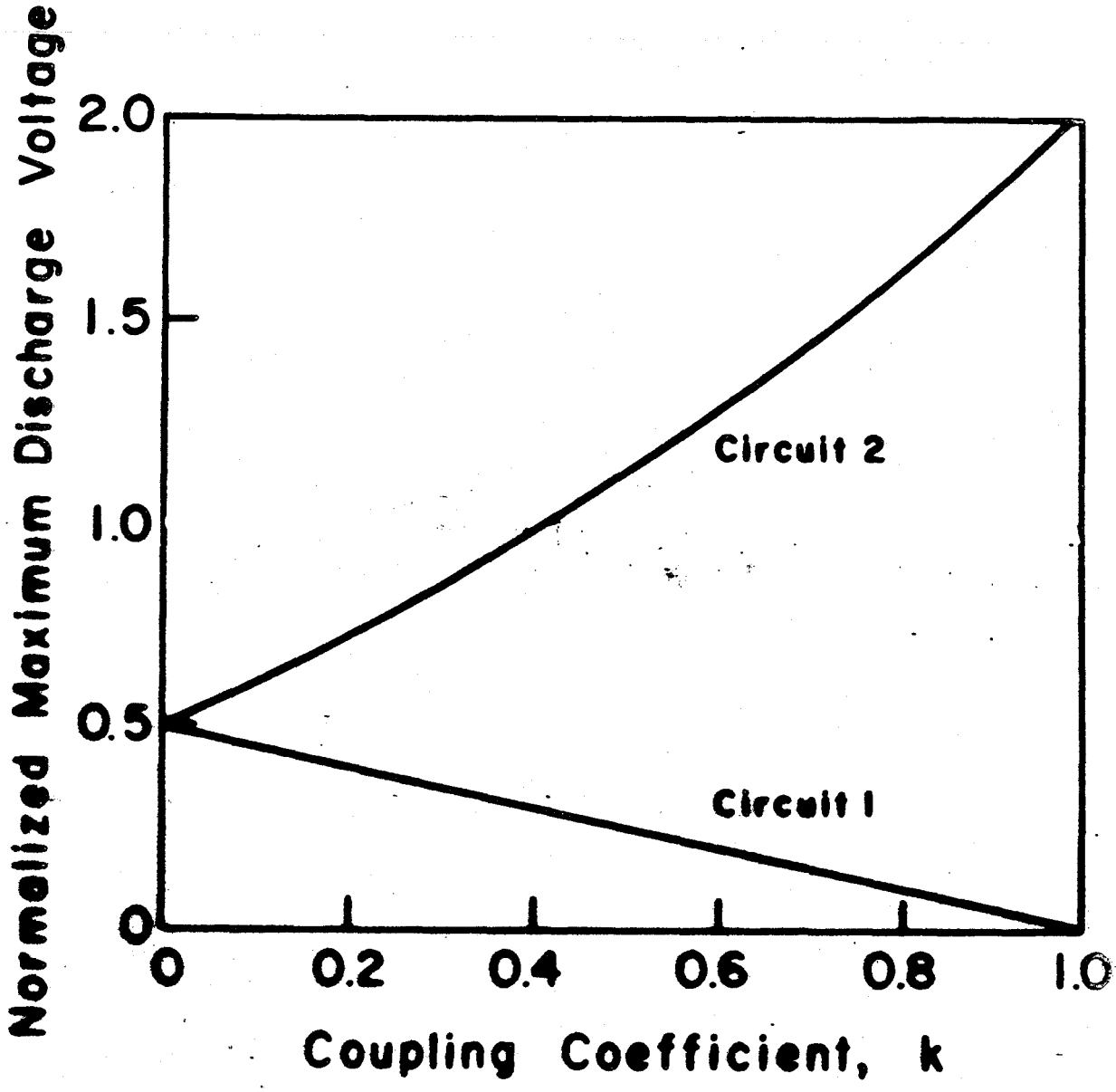

Fig. 3.1 Normalized maximum discharge voltage as functions of the coupling coefficient for a system having two circuits.

Table 3.1 Characteristics of Two-Circuit Systems

PARAMETER	CIRCUIT 1	CIRCUIT 2
Normalized Current, i/i_0		
initial value	1	1
after discharge of 1	0	1+k
after discharge of 2	0	0
Normalized Max. Voltage, V/V_0		
for $\tau = \tau_0$	$(1-k)/2$	$1/2$
for $T_{max} = T_f$	$(1-k)/2$	$(1+k)^2/2$
Normalized Time Constant, τ/τ_0		
for $T_{max} = T_f$	1	$1/(1+k)^2$

3.4 Discharge of Three-Circuit Systems

Consider the same system of 2N TF coils described in the previous section. However, it is now required that 2N be a multiple of 3 so that an equal number of identical coils can be included in each of three circuits. The first circuit will contain the first, fourth, .., 2N-2nd coils, the second circuit will contain the second, fifth, .., 2N-1st coils, and the third circuit will contain the third, sixth, .., 2Nth coils. If all circuits carry an initial current i_0, then prior to a discharge the conditions are identical to those of the single-circuit system. The analysis is similar to that for the two-circuit system. Because of the identical coils and symmetry, the self inductances of each of the three circuits are equal ($L_1 = L_2 = L_3 = L$), the mutual inductances are equal ($M_{12} = M_{21} = M_{13} = M_{31} = M_{23} = M_{32} = M$), and the coupling coefficients are equal ($k_{12} = k_{21} = k_{13} = k_{31} = k_{23} = k_{32} = k = M/L$).

In addition to the circuit complexity inherent in the three-circuit system, there are several features which should be noted. First, one has

the option of discharging all three circuits sequentially, or of discharging two circuits simultaneously. The results for a sequential discharge are described herein, as are the results for a simultaneous discharge of Circuits 2 and 3 following the complete discharge of Circuit 1.

The second basic feature which should be noted is that when one circuit has been discharged but two remain charged, azimuthal symmetry no longer exists. In traversing the toroid azimuthally, the pattern is: off, on, on, off, on, on, etc. This asymmetry leads to out-of-plane forces. The results of an analysis of these forces using an approximate model of the TF coils are included.

3.5 Discharge Currents and Voltages (3 Circuits)

Discharge characteristics for the three-circuit system are summarized in Table 3.2. These include normalized currents, maximum voltages, and discharge time constants, all expressed as functions of the coupling coefficient, k. Again, discharged circuits are assumed to be fully discharged and open circuited to avoid induced currents when the remaining circuits are discharged.

Normalized currents in Circuits 2 and 3 following discharge of Circuit 1 are increased by the same amount, as shown in Table 3.2. This is due to the inductive coupling and symmetry of the configuration. The amount of the increase, however, is less than that which occurs in the two-circuit system for a given coupling coefficient. Therefore, there is more flexibility available for choosing whether or not to use this inductively driven current increase as a mechanism for initiating normal regions to distribute the energy dissipation more uniformly throughout the system.

For the maximum voltages, three cases are summarized in Table 3.2: (1) sequential discharges with $\tau = \tau_0$, (2) sequential discharges with final maximum coil temperatures equal to T_f, and (3) discharge of Circuit 1 followed by the simultaneous discharge of Circuits 2 and 3, with all having final maximum coil temperatures equal to T_f. The assumptions associated with equation (3.2) are used to establish the conditions required to obtain T_f. Note that T_f is the same value, if (3.2) is satisfied, but the actual value is unspecified in this analysis because it depends on other parameters which are not discussed herein, such as the conductor design details.

Table 3.2. Characteristics of Three-Circuit Systems

PARAMETER	CIRCUIT 1	CIRCUIT 2	CIRCUIT 3
Normalized Current, i/i_0			
initial value	1	1	1
after discharge of 1	0	$\frac{1+2k}{1+k}$	$\frac{1+2k}{1+k}$
after discharge of 2	0	0	$1+2k$
after discharge of 3	0	0	0
Normalized Max. Voltage, V/V_0			
for $\tau = \tau_0$	$\frac{(1-k)}{3(1+k)}$	$\frac{(1-k)}{3}$	$\frac{1}{3}$
for $T_{max} = T_f$	$\frac{(1-k)}{3(1+k)}$	$\frac{(1-k)}{3}\left(\frac{1+2k}{1+k}\right)^2$	$\frac{(1+2k)^2}{3}$
for $T_{max} = T_f$ and discharge of 2 and 3 together	$\frac{(1-k)}{3(1+k)}$	$\frac{1}{3}\left(\frac{1+2k}{1+k}\right)^2$	$\frac{1}{3}\left(\frac{1+2k}{1+k}\right)^2$
Normalized Time Constant, τ/τ_0 for sequential discharge	1	$\left(\frac{1+k}{1+2k}\right)^2$	$\left(\frac{1}{1+2k}\right)^2$
for discharge of 2 and 3 together	1	$\left(\frac{1+k}{1+2k}\right)^2$	$\left(\frac{1+k}{1+2k}\right)^2$

Plots of the normalized maximum discharge voltages are given in Fig. 3.2 as functions of the coupling coefficient for Case 2 (sequential discharges with $T_{max} = T_f$) and Case 3 (discharge of Circuit 1 followed by simultaneous discharge of Circuits 2 and 3, all with $T_{max} = T_f$). Note that the Circuit 1 discharge is the same for both cases. Again, consistent with (3.4), the fractional energy dissipated during discharge of Circuit 1 is equal to the normalized maximum discharge voltage. Figure 3.2 shows that the use of multiple circuits can provide a substantial reduction in the circuit voltages to ground, particularly if the coupling is low or if Circuits 2 and 3 are discharged simultaneously when using a three circuit system.

The normalized time constants given in Table 3.2 are plotted in Fig. 3.3 as functions of the coupling coefficient. Only two curves are needed because the time constant for the simultaneous discharge of Circuits 2 and 3 is equal to the time constant for Circuit 2 in the sequential discharge, and the time constant for Circuit 1 is τ_0.

3.6 Force Considerations (3 Circuits)

When one circuit of a three-circuit system is discharged, azimuthal symmetry no longer exists. This results in out-of-plane forces on the TF coils. As a means for estimating the rough order of magnitude of these forces, an approximate model of the TF coils has been analyzed. The model, described by Boris and Kuckes [2] and Thome and Tarrh [3], consists of 2N straight current filaments of infinite length carrying currents in the z direction at the locations of the TF coil inner legs ($r = a_1$) and 2N straight current filaments carrying currents in the opposite direction at the locations of the TF outer legs ($r = a_2$). If R is defined as the

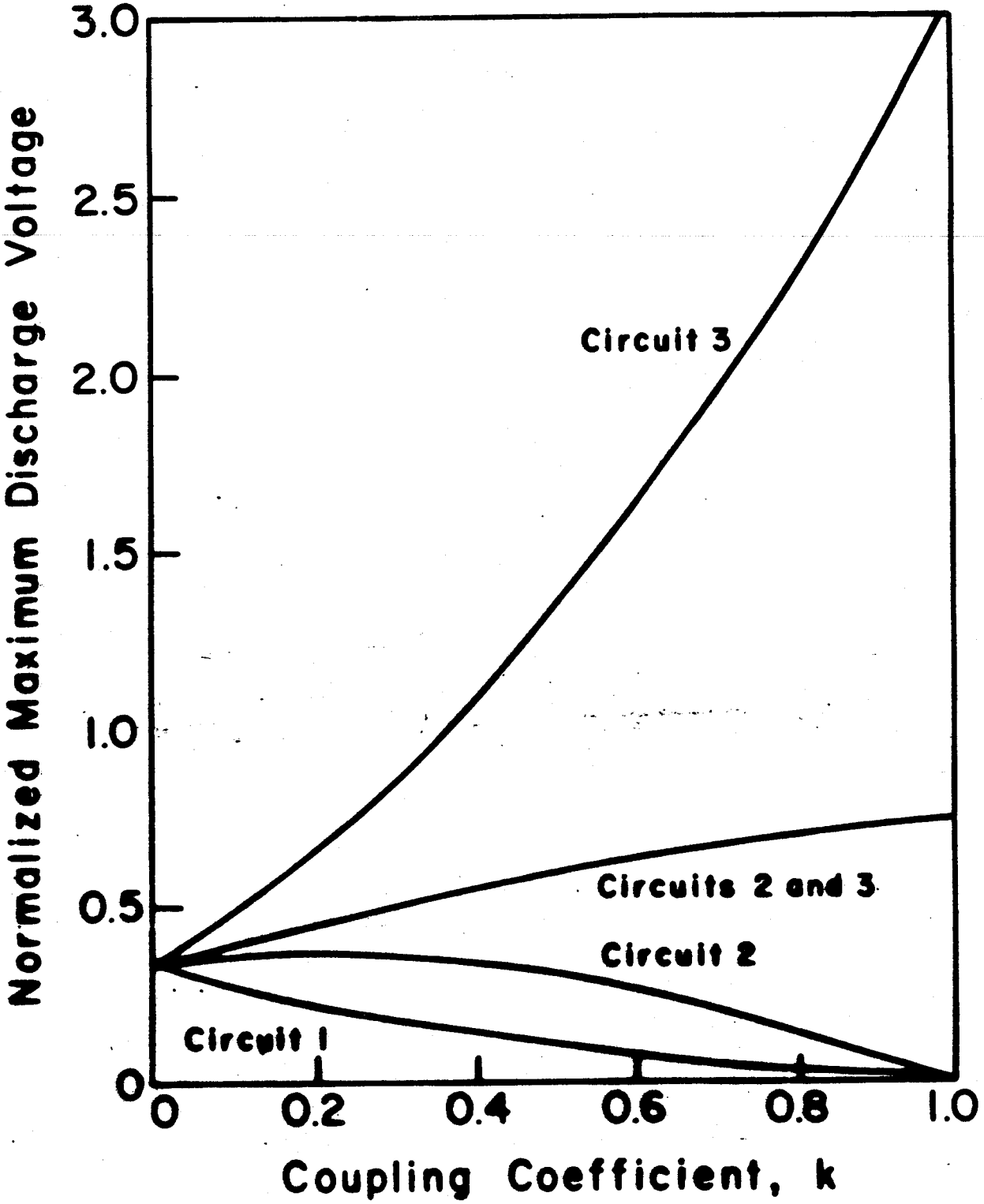

Fig. 3.2 Normalized maximum discharge voltages as functions of the coupling coefficient for a system having three circuits, discharged under conditions of equal final temperatures.

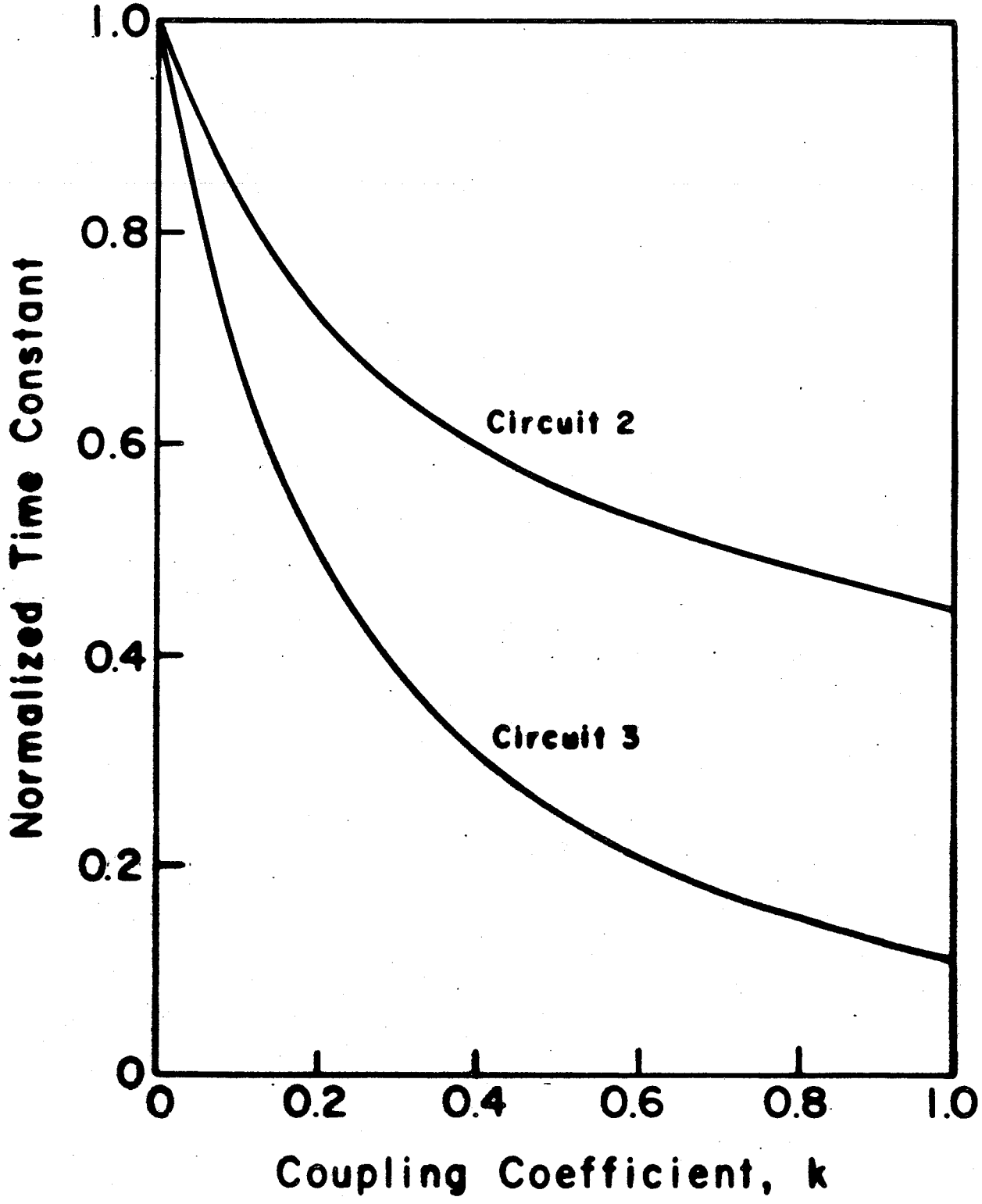

Fig. 3.3 Normalized discharge time constants as functions of the coupling coefficient for a system having three circuits which are discharged sequentially under conditions of equal final temperatures.

average of a_1 and a_2, which is the major radius of the toroid, while $(a_2-a_1)/2 = a$ is defined as the minor radius of the toroid, then the normalized out-of-plane forces on both legs can be expressed analytically as functions of R/a for various numbers of coils for three-circuit systems.

The results of this analysis are plotted in Figs. 3.4 and 3.5, which contain the forces on the inner and outer legs, respectively. These arise from the radial component of field at the leg locations. In both plots the normalizing quantity is the centering force on the inboard leg when all circuits are energized, using the approximate model. When Circuit 1 is discharged, the out-of-plane force is an attraction between the coils of Circuits 2 and 3 which increases as the number of coils is increased. As shown in the figures, the out-of-plane force on the inner leg is < 20% of the centering force, while on the outer leg the out-of-plane force is < 14% of the centering force.

Note that for the two-circuit system, symmetry is maintained if Circuit 1 is discharged. Thus the two-circuit system has the advantage over the three-circuit system of having no net out-of-plane loads due to TF coil interactions.

3.7 Discharge of Multiple-Circuit Systems

An analysis similar to those presented in the previous sections has been performed for multiple-circuit systems containing as many as nine separate circuits. To maintain the simplicity of the analysis, it was assumed that the total number of TF coils was an integral multiple of the total number of circuits. Thus each circuit in the multiple-circuit system is assumed to contain an equal number of identical coils for a given

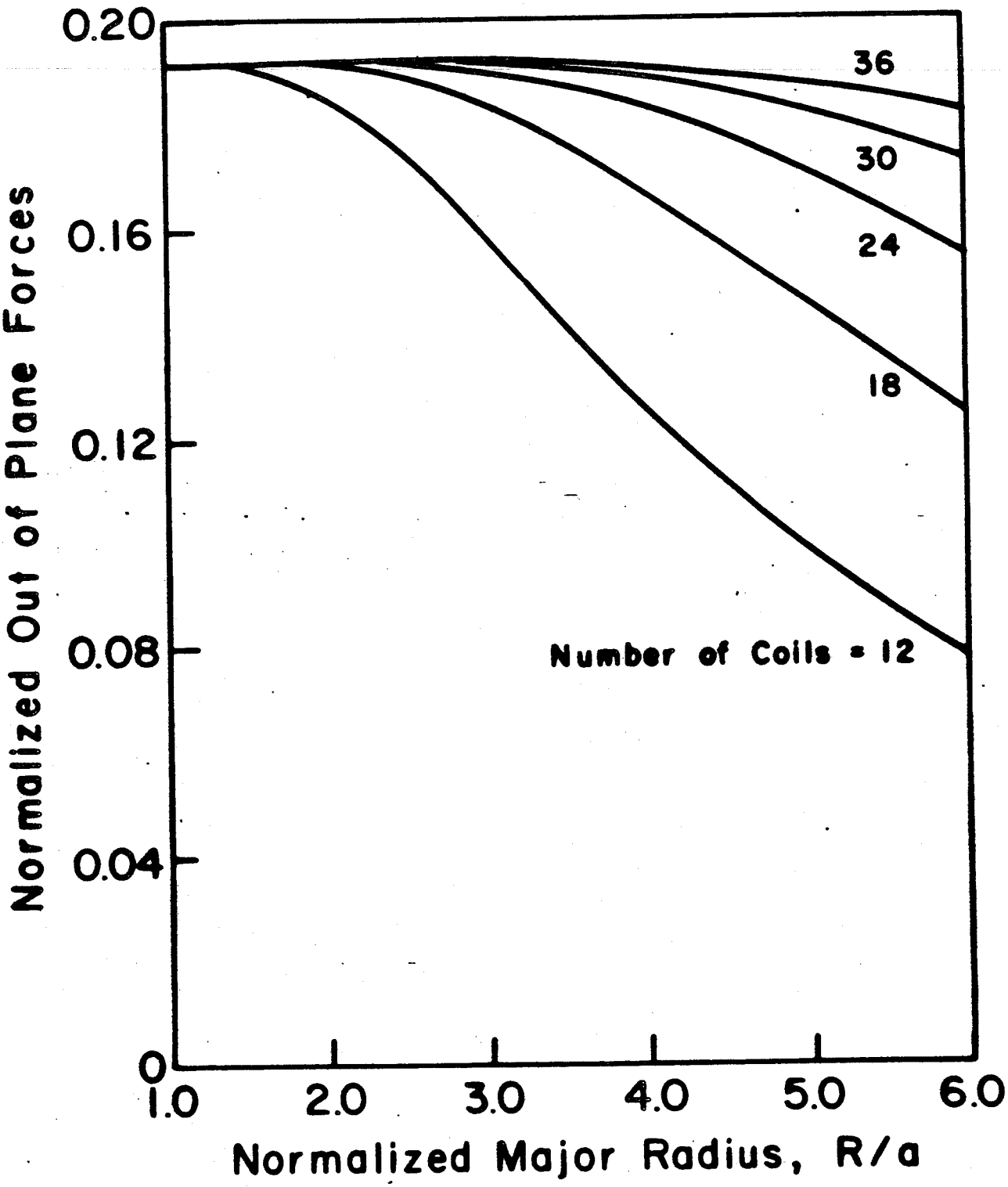

Fig. 3.4 Approximate normalized out-of-plane forces on the inboard leg as functions of the normalized major radius for various numbers of coils in a system having three circuits.

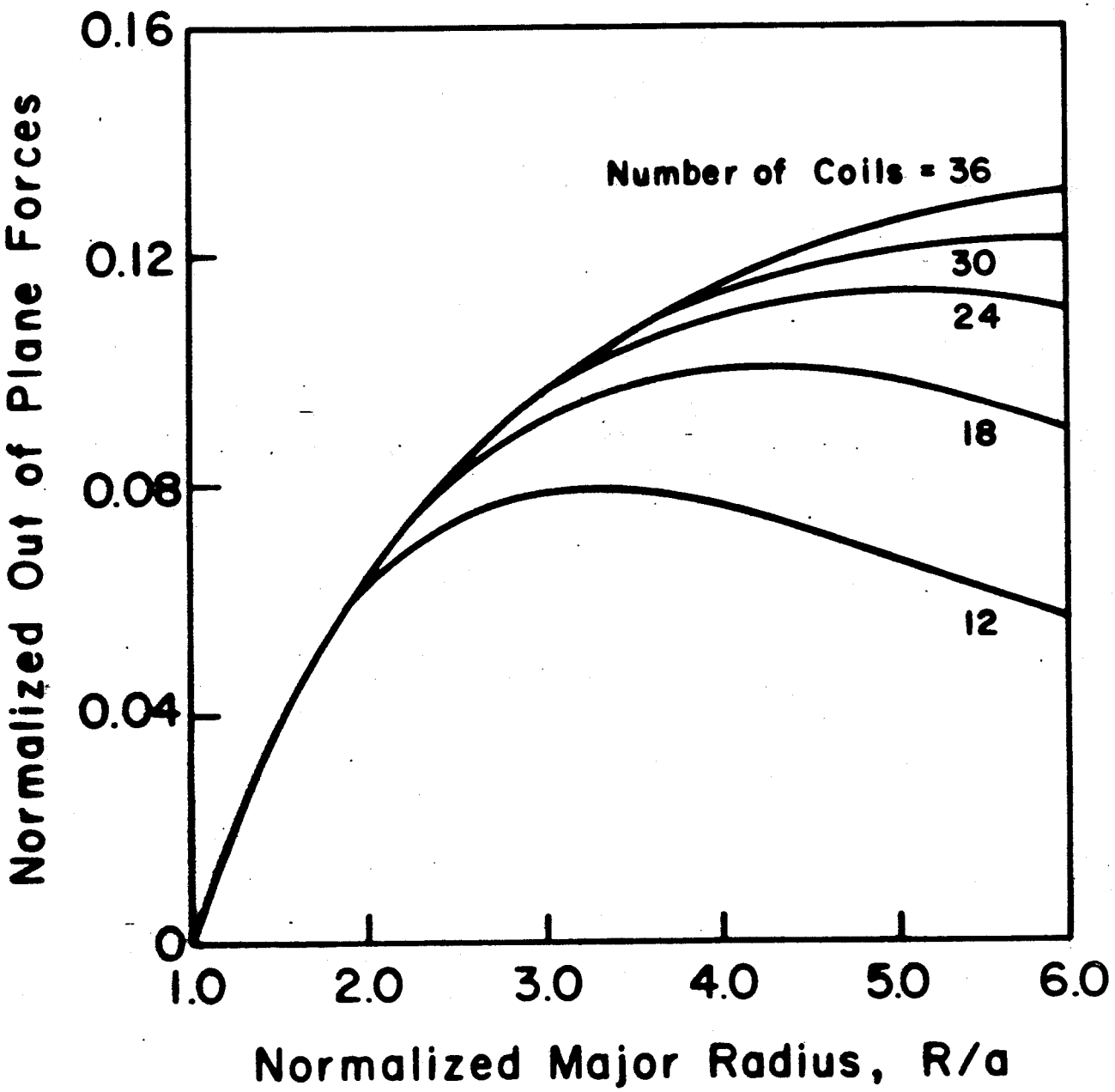

Fig. 3.5 Approximate normalized out-of-plane forces on the outboard leg as functions of the normalized major radius for various numbers of coils in a system having three circuits.

case. The discharge characteristics for the first circuit in the multiple-circuit system are presented. The requirements on, and discharge characteristics of, the remaining circuits are the subject of ongoing systems analysis.

A computer program has been written to examine the discharge characteristics for specific cases, based on the analysis. The program has been applied to the TF configuration given in Fig. 3.6, which is an early version of the TFCX TF coils. For this application, from 1 to 8 circuits were considered. In addition to the 16 coil TF set described in Fig. 3.6, a 12 coil set was analyzed by using the same dimensions shown in the figure, but with the ampere turns per coil increased by the ratio of 16/12. The self and mutual inductances for a given number of multiple circuits were obtained by computing the self and mutual inductances for and between individual coils in the complete set, then collapsing the inductance matrix based on the number of multiple circuits. The general formulation and procedure for this calculation, as well as the analysis of the discharge characteristics, are available [1] and will not be reproduced here due to space limitations.

Results of this analysis applied to the TFCX configuration are given in Table 3.3. Spaces in the table are left blank where the basic assumptions on joining coils into separate circuits can not be met. Thus there are no results for the case of 16 TF coils and three circuits, for example, because the 16 coils can not be evenly divided among the 3 circuits. The discharge characteristics given are for discharge of the first circuit only.

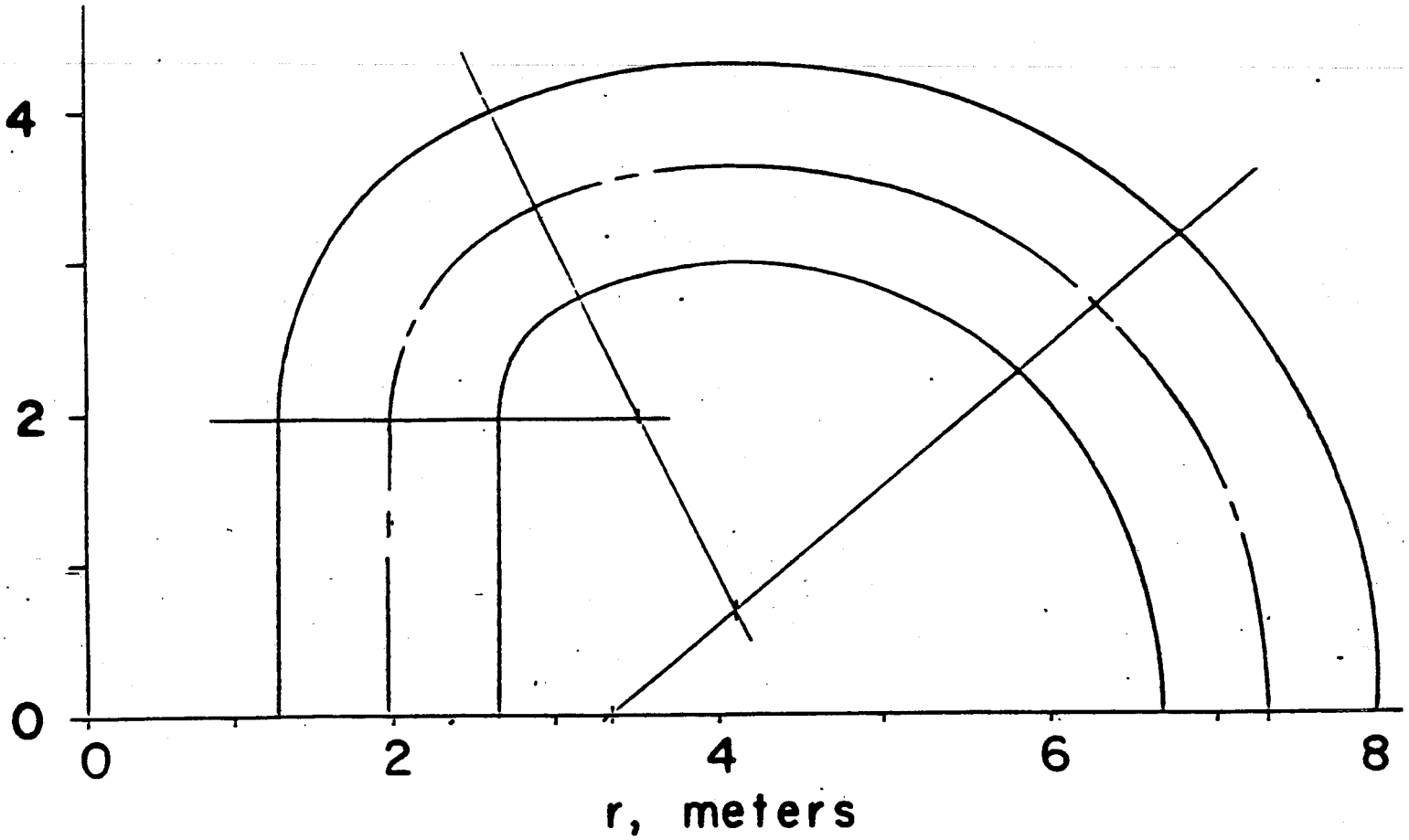

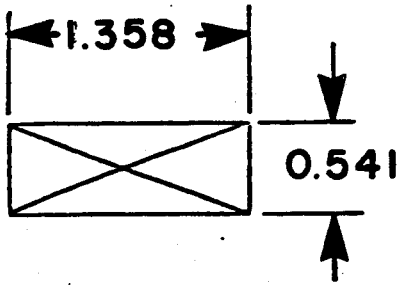

Fig. 3.6 Sketch of a typical TF coil for TFCX, which includes 16 TF coils, each having a thickness of 0.541 m.

Table 3.3. Characteristics of TFCX

PARAMETER	NO. OF COILS	NUMBER OF CIRCUITS 1	2	3	4	6	8
Normalized Current, i/i_0	12	0	1.6	1.3	1.29	1.28	-
	16	0	1.74	-	1.36	-	1.35
Normalized Voltage, V/V_0	12	1.00	0.20	0.13	0.10	0.06	-
	16	1.00	0.13	-	0.06	-	0.03
Norm. Toroidal Field, B/B_0	12	0	0.80	0.87	0.90	0.94	-
	16	0	0.87	-	0.94	-	0.97

The normalized current parameter given is the current in the circuit adjacent to the discharged circuit, normalized to the current prior to discharge. The current in the adjacent circuit is given because this is the circuit most strongly influenced, due to the closer coupling to the discharged circuit. The most significant current increase occurs for two circuits, while for three or more circuits the current increase does not depend strongly on the number of circuits.

The normalized maximum voltage parameter given is also equal to the fractional energy removed during the discharge of the first circuit, in accordance with (3.4). As the number of circuits is increased, the fractional energy removed and the maximum voltage to ground both decrease, with the most dramatic decrease occurring for two to three circuits in comparison to one.

The normalized toroidal field parameter is the ratio of the final average toroidal field to the initial field level. The table indicates that 80% or more of the initial field level is maintained for the 12 coil system with two or more circuits when one is discharged, and that 87% or more is maintained for the 16 coil set.

3.8 Summary and Conclusions

The use of multiple TF coil circuits has been shown to have advantages and disadvantages. The primary disadvantage is the increased circuit complexity. While having two circuits may be only moderately more complex than one, the complexity (and consequent reliability considerations) involved with having three or more circuits is considerably increased. The second major disadvantage of having three or more circuits is the resulting out-of-plane forces when one circuit is discharged. For the single and two-circuit systems, there are no unbalanced out-of-plane loads due to TF coil interactions.

The major advantage of multiple TF coil circuits is the reduction of maximum discharge voltages to ground. Relative to the single-circuit system, using two circuits can significantly reduce the discharge voltages, while further reductions can be achieved by using three or more circuits.

A second advantage of multiple circuits is that one may have the option of using the inductively-driven coil current increase as a mechanism for initiating normal regions and spreading the energy dissipation. For two-circuit systems, it appears that with only moderate coupling the initiation of normal regions would be unavoidable due to the level of the increased current. However, with three or more circuits, it appears that one would have the choice of whether or not to use this mechanism.

3.9 References for Chapter 3

1. R.J. Thome, et al., "Safety and Protection for Large Scale Superconducting Magnets - FY1983 Report", PFC/RR-83-33, December 1983.

2. J.P. Boris and A.F. Kuckes, "Closed Expressions for the Magnetic Field in Two-Dimensional Multipole Configurations," Nuclear Fusion, Vol. 8, pp. 323-328, 1968.

3. R.J. Thome and J.M. Tarrh, MHD and Fusion Magnets: Field and Force Design Concepts. New York: John Wiley, 1982, Ch. 3, pp. 158-160.

4.0 HPDE MAGNET FAILURE - J.M. Tarrh and H.D. Becker

4.1 Introduction

In December of 1982 a large magnetohydrodynamic (MHD) magnet for the High Performance Demonstration Experiment (HPDE) at the Arnold Engineering Development Center (AEDC) suffered a catastrophic structural failure, which led to brittle-fracture failures in most of the structural components, significant displacements (on the order of a meter) of some of the magnet iron frame components, and similar deformation of the winding with some conductor fracture. Our FY83 report contains a detailed description of the magnet system, a summary of the failures, and the results of a preliminary structural failure analysis.[1] This chapter contains a brief introductory summary of the magnet system and cause of failure, and an update of the preliminary analysis to document work performed during FY84.

4.2 Summary

The HPDE employed a large (active bore approximately 1 m square x 7 m long) iron-bound copper magnet designed to operate in either of two modes: (1) as a 3.7 T (continuous) water cooled magnet, or (2) as a 6 T (long pulse) nitrogen-precooled, cryogenic magnet. In either mode, coolant would flow through conventional hollow copper conductor windings. A unique force containment structure (FCS) was designed for the magnet. An aluminum alloy (2219) was selected on the basis of thermal considerations (77 to 350 K operating temperature range; coefficient of thermal expansion permitting dimensional matching to the coil) and cost.

Figures 4.1 through 4.3 show, respectively, a photograph prior to the failure of the magnet including the outer thermal enclosure, the general distribution of the design Lorentz forces on the coil windings, and the force containment structure (FCS). Components of the FCS were fastened together with high strength keys and bolts.

The FCS design analyses identified multiple load paths for support of the total longitudinal force. The effects of tolerances on the interactions among FCS components increased the complexity of the structural analysis. Although the design was conservative with respect to support of the longitudinal loads, the analysis overlooked the effects of transverse loads (in the saddle region) on the longitudinal force support elements.

Figures 4.4 and 4.5 graphically depict the effects of the transverse saddle loads on the longitudinal tension members (LTM) and on the collars. As a result of these transverse loadings, the calculated combined stresses in the fingers of the LTM (where they are notched to penetrate the faceplate) were on the order of 130 ksi which is well in excess of the measured ultimate strength of the 2219 aluminum alloy (at 77 K). These stresses occurred at a field level of 4 T, which is approximately half the design load. Stresses in the collar fingers were on the same order.

The magnet failed at a field level of 4.1 T as a result of design defects that were not detected during the FCS design analyses. For a more detailed discussion of the design and analysis of the failure, including a discussion of failure scenarios, see Reference 1.

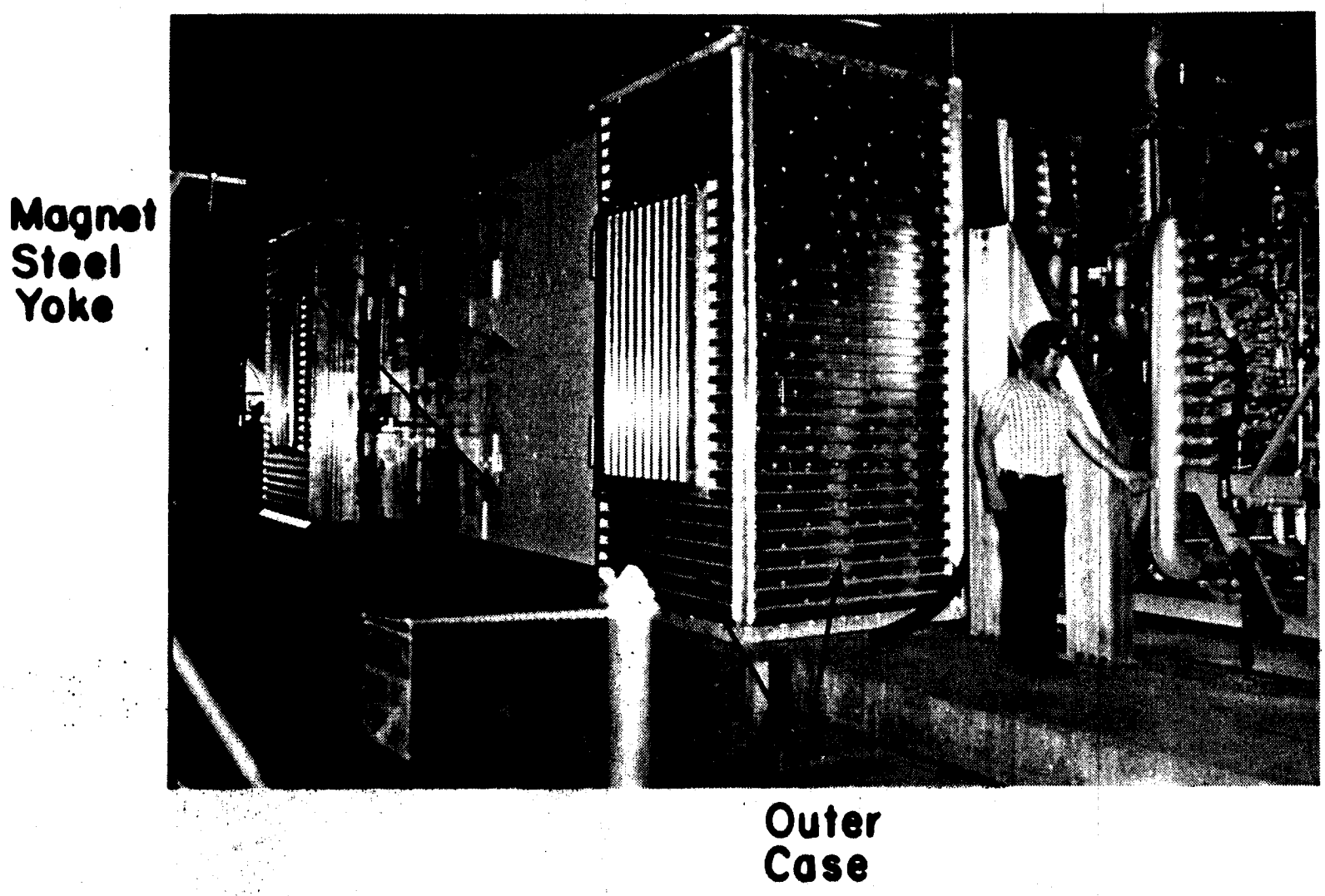

Figure 4.1 Overall view of the assembled magnet system.

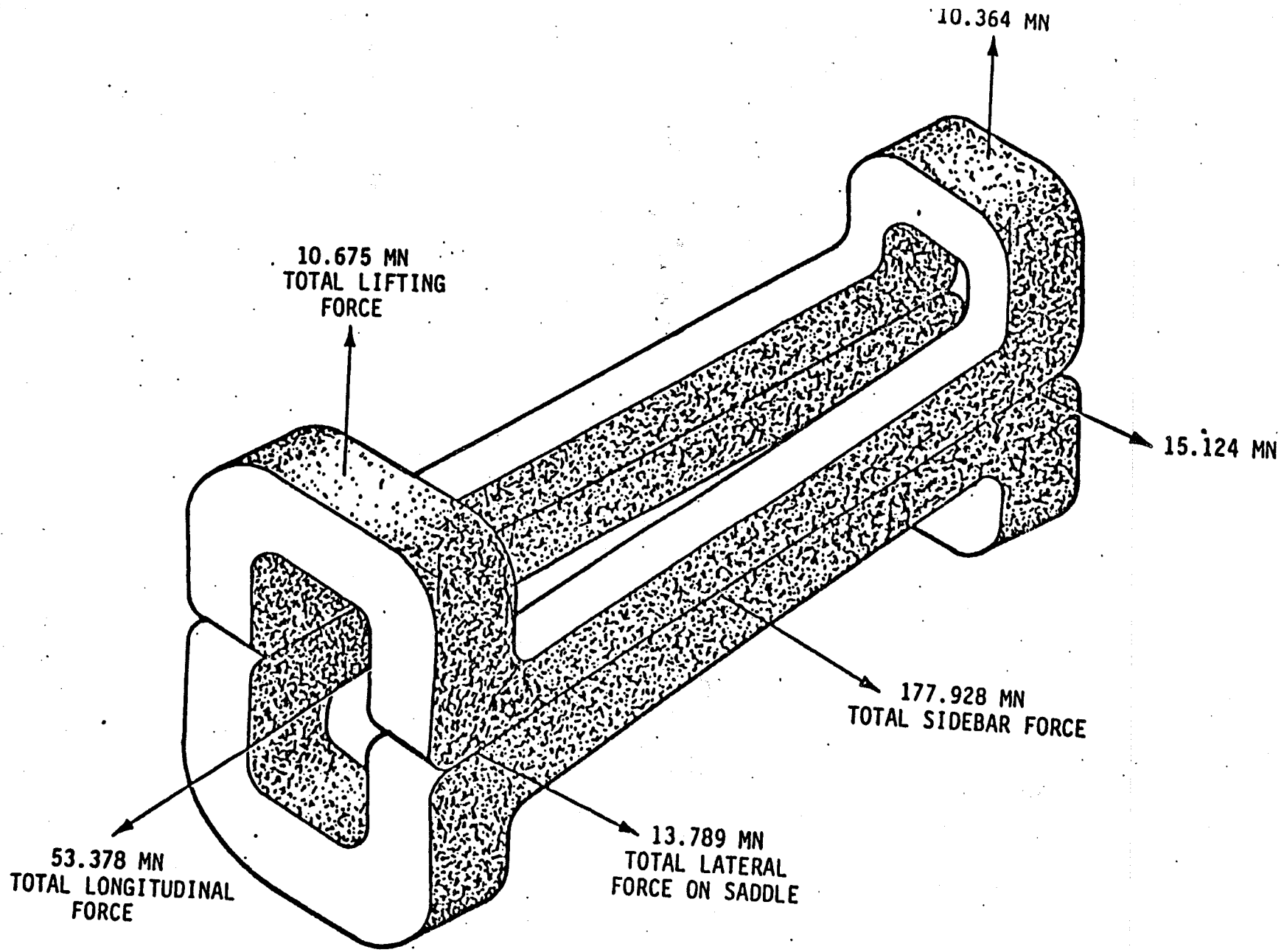

Figure 4.2 HPDE Saddle Magnet Coils: 6.8 T Design Lorentz Forces

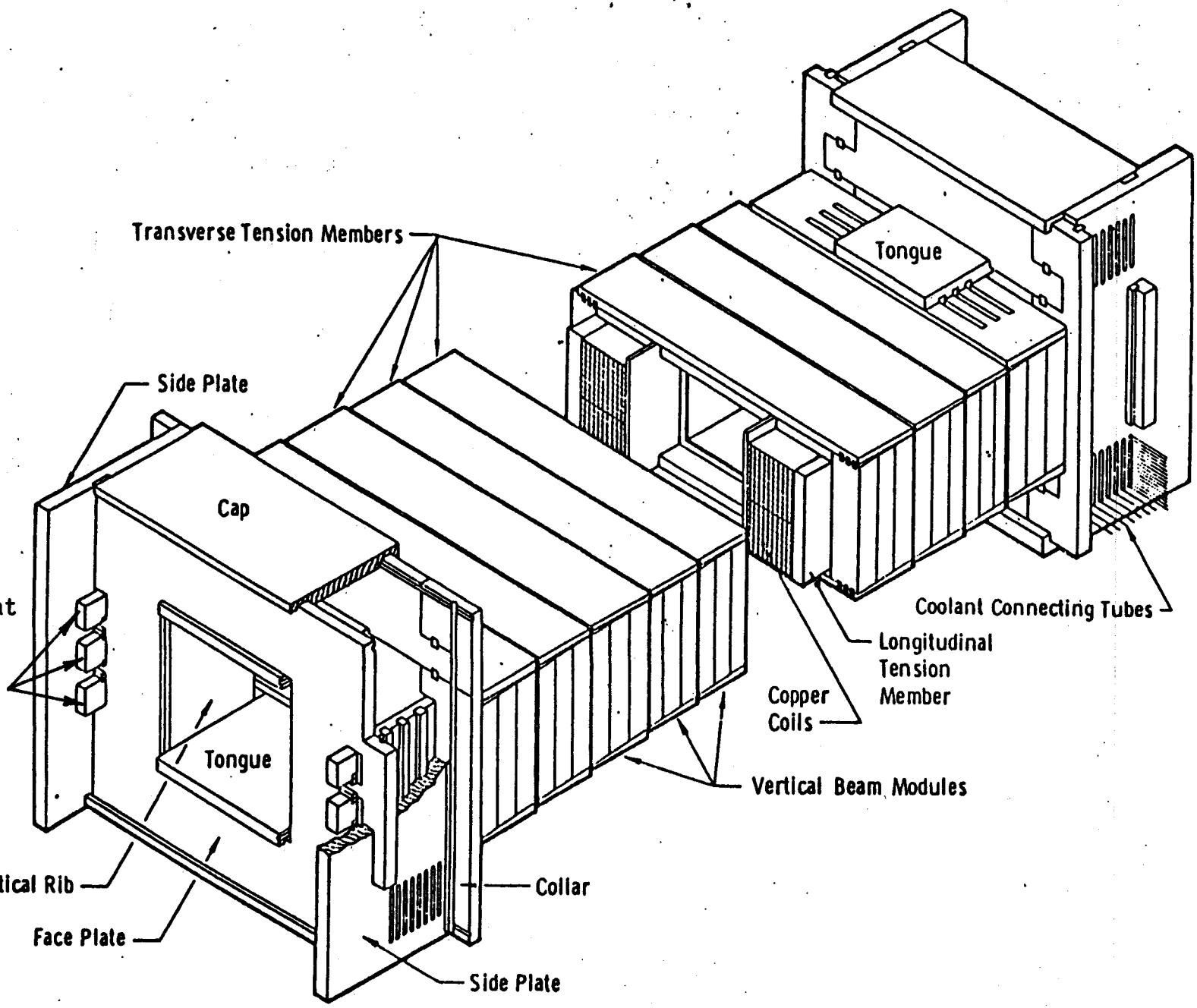

Figure 4.3 Aluminum Force Containment Structure (FCS)

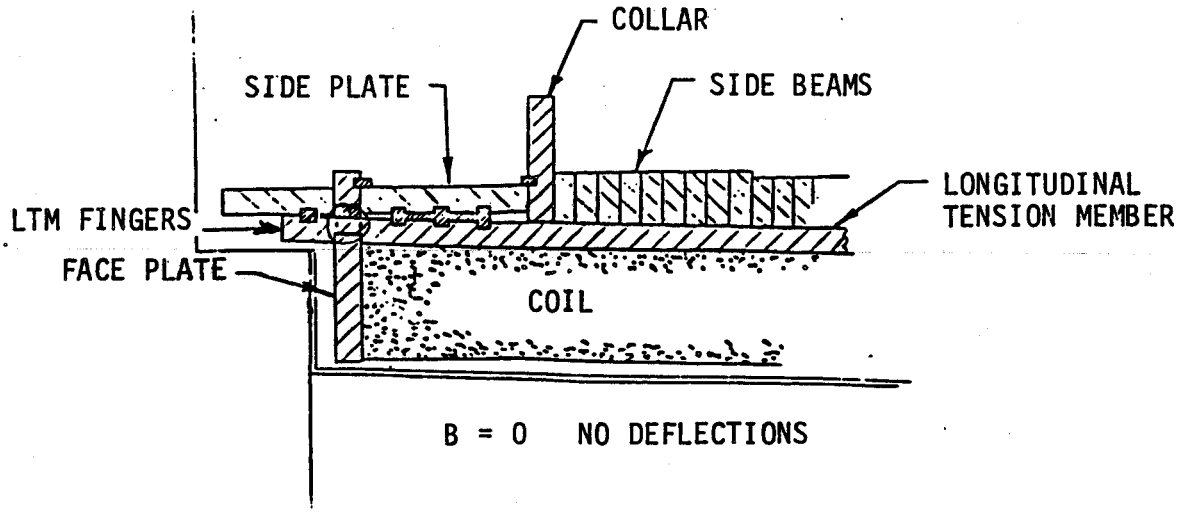

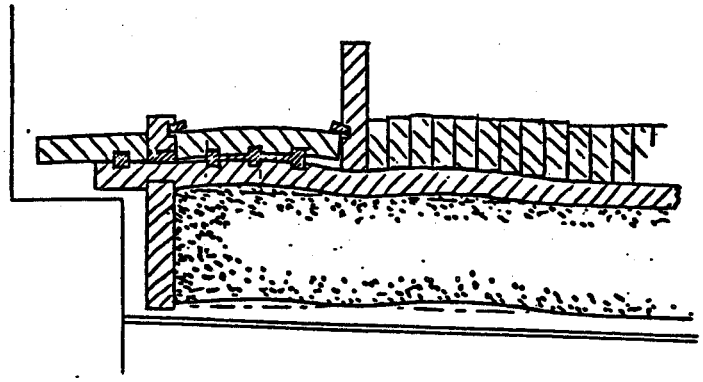

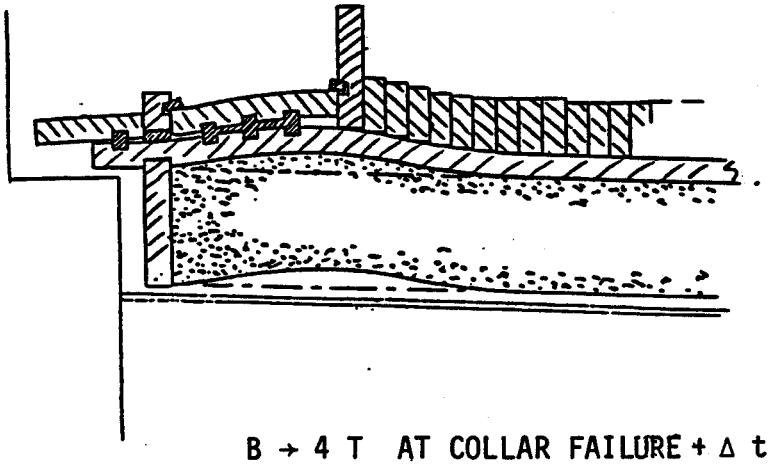

Figure 4.4 Exaggerated depiction of LTM-related deflections at the magnet midplane

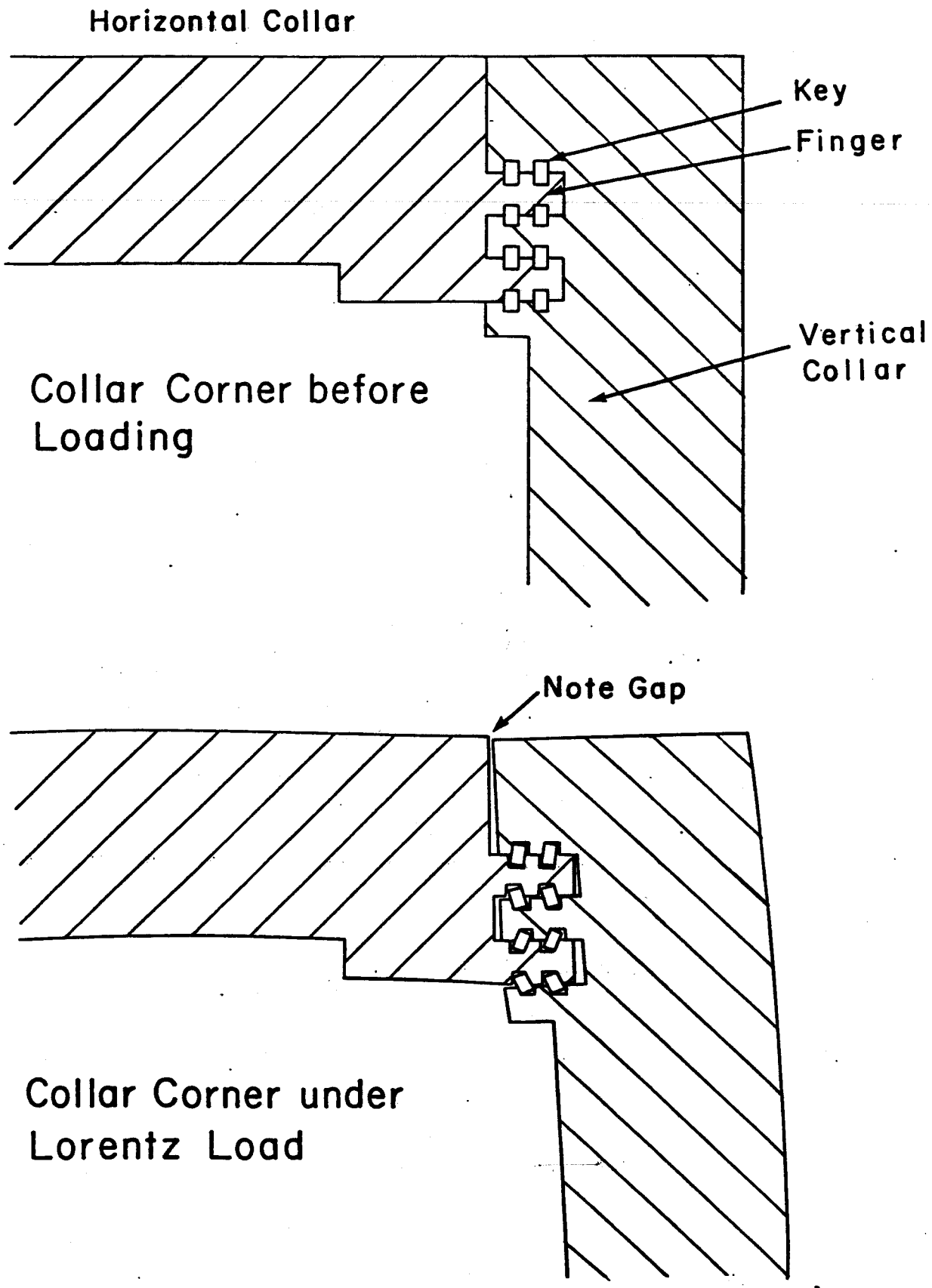

Figure 4.5 Collar corner behavior

4.3 Update of Preliminary Structural Failure Analysis

During FY84, key elements of the preliminary failure analysis were reviewed and updated. The principal focus of the effort was to recalculate the magnetic fields and forces using up-to-date tools and techniques since the preliminary failure analysis had been based on the original design calculations which were performed during the mid-1970's.

To recalculate the magnetic fields and forces, a current level corresponding to a peak on-axis field of 4 T was used, since this was approximately the field strength (and force level) at which failure occurred. A three-dimensional filamentary model of the coil was constructed using a 2 x 2 matrix of filaments per coil. The coil model closely approximated the actual coil configuration in that the bore taper was accurately included in the model. Two detailed filamentary models of the iron return frame were also constructed. These were three dimensional in that they were of finite length. However, the taper was not included in these models, one of which consisted of the dimensions of the iron at the inlet end of the magnet, while the other used the outlet end dimensions. The differences in fields between these two iron models were not significant, particularly since the fields (and forces) on the coil outlet end turns were of primary interest. The coil outlet end turn fields and forces were of primary interest because the structural failure was initiated in the outlet end turn region of the magnet.

Separate models of the coils and iron were used so that the effects of the iron on the total coil forces could be determined accurately. This was necessary so that force scaling with current level could be easily accomplished, because the total force on the coil over a given region of the

coil can vary more (or less) strongly than the square of the current level depending on whether the field within the coil due to the iron subtracts from (or adds to) the field due to the coil itself. This is true because, above saturation, the force on the coil due to the iron is approximately directly proportional to the current level, whereas the force on the coil due to the coil itself is directly proportional to the square of the current level. This can be expressed as

$$F = kI^2 \pm IB_i \qquad (4.1)$$

where

F	=	total force on coil region
I	=	current level
KI^2	=	force on coil due to coil
IB_i	=	force on coil due to iron
k, B_i	=	proportionality constants

and the negative sign is used if the iron field subtracts from the coil field (within the coil), while the positive sign is used if the iron field adds to the coil field (within the coil). Because the first term in this equation typically dominates in these configurations, it can be shown that the negative sign leads to a total force which varies more strongly than the square of the current level, while the positive sign leads to a total force which varies less strongly than the square of the current level.

Using these models to determine the forces in the outlet end of the coil yielded the following results (values are forces expressed in MN at a current level corresponding to a peak on-axis magnetic field of 4 T):

	AXIAL	LATERAL	VERTICAL
Coils Only	17.3	2.5	2.5
Coils and Iron	16.4	2.9	3.5

Appropriate scaling of these forces with current level allows comparison with the original design force calculations summarized in Fig. 4.2. This was a valuable process, as it uncovered a mistaken assumption that had been used for the preliminary structural failure analysis. Because the design peak on-axis magnetic field of the magnet was 6 T, it was assumed that the forces of Fig. 4.2 corresponded to a 6 T field condition. The presentations in the original references were unclear on this point. It was discovered, however, that the Fig. 4.2 forces in fact correspond to a peak on-axis magnetic field of 6.8 T rather than 6 T. The 6.8 T field level was a performance goal in effect during the early stages of the magnet design. This goal was relaxed to 6 T during the design process, although the force and coil pressure distributions that were presented in the original references (the final design report) remained unchanged, corresponding to the current level for a 6.8 T peak on-axis field. (This discrepancy has been promulgated in several places.[1-3] Consequently, the coil forces used in our preliminary structural failure analysis were in error. The force values were scaled from 6 T to 4 T assuming that they were directly proportional to the square of the field, when in fact they should have been used closer to 0.30 based on the more recent calculations described hereinabove.

The actual force levels at failure were therefore considerably less (by a third) than those used for our preliminary structural failure analysis. However, we have reviewed the failure analysis in view of the reduced force levels and find that while the specific numerical values

change, all of the conclusions of the preliminary failure analysis remain valid since the maximum stresses would be of the order of 130 ksi which exceeds the ultimate strength of 2219 aluminum alloy.

A final comment on the significance of this failure is in order. Subsequent to the failure, the structure was considered beyond repair. The coil windings were considered to be repairable without prohibitive time, effort, or cost assuming reduced performance requirements (single mode operation only, pulsed from room temperature). The magnet could have been rebuilt without an infusion of substantial additional funds by performing the repair and rebuild using the anticipated future operating funds slated for the facility. The experiment was unique in size and field strength, and at the time of the failure had just begun to obtain significant data on new MHD phenomena (the so-called magnetoaerothermal instability), which may be of significance to the overall development and commercialization of MHD. The MHD community was therefore strongly in favor of repairing the magnet so that these unique experiments could continue. Nevertheless, the magnet repair was in fact not initiated, and at this time the facility remains shut down and mothballed with all of the personnel disbanded to work on other (non-MHD) projects. These facts underscore the significance of this failure and the criticality of the magnet system as a component to those large scale technologies which require them.

Additional comments on this magnet failure (among others) were included in a workshop on magnet failures held during the MT-8 Conference in Grenoble.[4]

4.4 Reference for Section 4

1. R.J. Thome, R.D. Pillsbury, Jr., W.G. Langton, et al., "Safety and Protection for Large Scale Superconducting Magnets - FY83 Report," MIT Plasma Fusion Center, Cambridge, MA, December 1983.

2. R.M. James, et al., "Investigation of an Incident During Run M1-007-018 MHD High Performance Demonstration Experiment (PWT) on December 9, 1982," ARVIN/CALSPAN Field Services, Inc., AEDC Division, Arnold Air Force Station, TN, April 1983.

3. H. Becker, J.M. Tarrh, and P.G. Marston, "Failure of a Large Cryogenic MHD Magnet," presented at the MT-8 Conference, Grenoble, September 1983, published in Journal de Physique, Colloque C1, supplement au n^{o} 1, Tome 45, Janvier 1984.

4. P.G. Marston, et al., "Magnet Failure Workshop," Journal De Physique, Colloque C1, supplement au n^{o} 1, Tome 45, Janvier 1984.

5.0 TFCX MAGNET OPTIONS - R.J. Thome, U.R. Christensen, M. Pelovitz and W.G. Langton

A preliminary study of fault load conditions was carried out for three of the options under consideration for TFCX. The specific characteristics of the cases are defined in this chapter and the alterations in electromagnetic loads under specific TF and PF fault conditions are compared. A large number of faults were evaluated, but the study was by no means complete. In many instances, loads are nontrivial, but are believed to be manageable through proper structural and protection circuit design. They indicate a need for ultimate specification of a list of credible faults and their consideration in the design process.

5.1 Option Definition

The TFCX preconceptual design effort defined four options[1] which could satisfy the same physics mission. They consisted of machines using copper or superconducting TF coils based on "nominal" or "high performance" design criteria. In all cases, the PF coil system was superconducting. Early in the effort, a hybrid system consisting of a nested set of copper TF coils within a set of superconducting TF coils was also considered.

This study was initiated before the last TFCX preconceptual design iteration; hence, the specific machine characteristics are somewhat different from those in the design reports.[1] The features of the three systems are summarized in the elevation views in Fig. 5.1 which shows the TF winding outline and PF coil cross sections for one quadrant of the machine. All coil systems are symmetric relative to the z = 0 plane and consist of TF coils in planes equally spaced around the z axis and PF coils coaxial with the z axis. The top figure has a maximum toroidal field of 8.45 T

Fig. 5.1 - Comparison of TF Coil Characteristics

E = 4250 MJ
MAT = 4.38
F_c = 69.4 MN
F_v = 42.3 MN
M_r = 67.8 MN-m

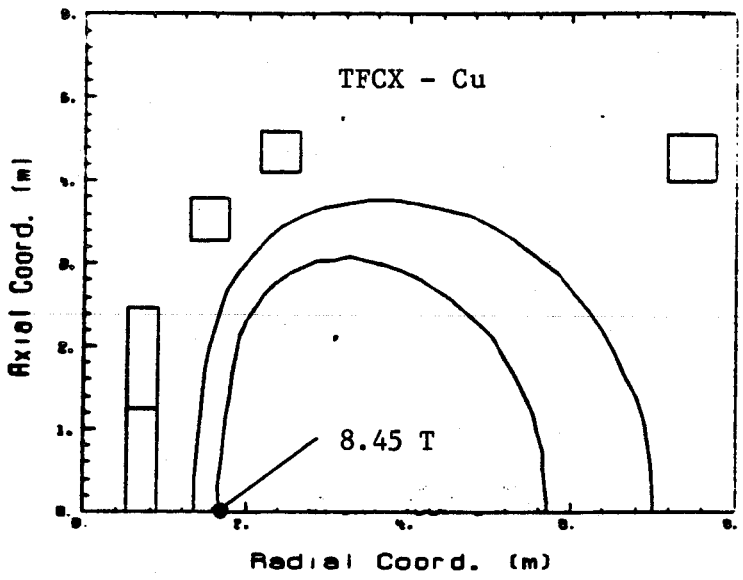

bore ∿ 4.1 x 6 m
(∿ nom Cu)

TFCX - SUPERCONDUCTING

E = 7460 MJ
MAT = 5.36
F_c = 140 MN
F_v = 74.6 MN
M_r = 114.6 MN-m

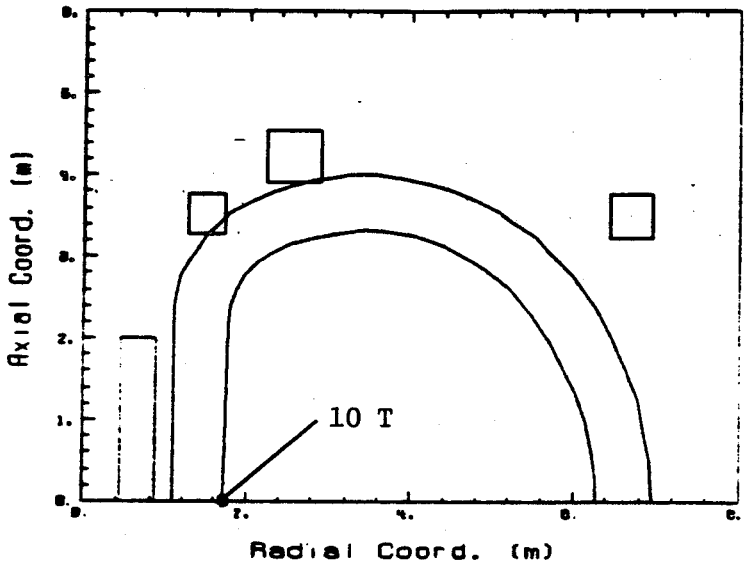

bore ∿ 4.4 x 6.4 m
(∿ Hi Perf SC)

TFCX - HYBRID

E = 3280 MJ
MAT = 3.88 + 1.43 = 5.31
F_c = 68.0 + 2.8 = 70.8 MN
F_v = 32.1 + 18.1 = 50.1 MN
M_r = 61 + 12.6 = 73.6 MN-m

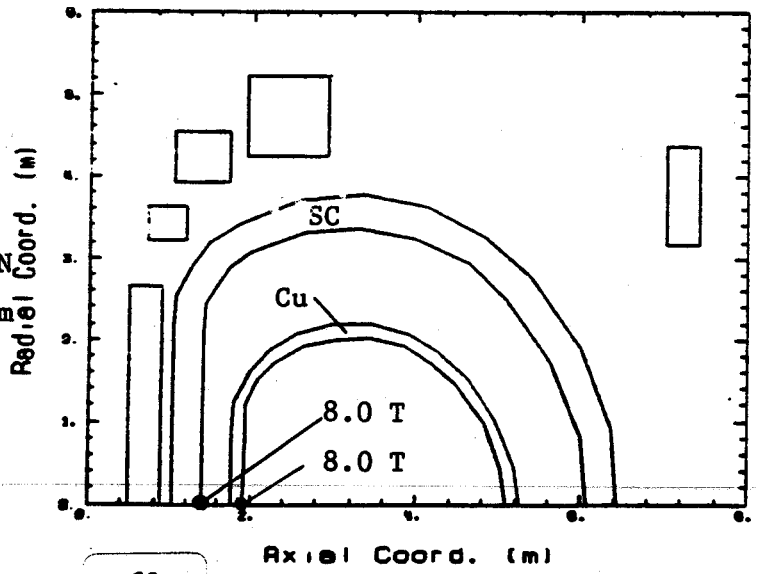

bore ∿ 3.4 x 4 m
(- - - -)

at the winding and is similar to the "nominal" copper design for TFCX; the center figure has a maximum field of 10 T and is similar in size and TF level to the "high performance" superconducting design although the plasma current and PF system were not yet optimized at this stage; the lower figure is a "hybrid" of 16 copper coils nested in 16 superconducting coils with a maximum field of 8.0 T and was under consideration early in the TFCX design effort, but ultimately discounted as an option. The figure also summarizes selected characteristics under usual operating conditions, that is: E = stored energy in the TF coils; MAT = megampere-turns per TF coil; F_c = net load per TF coil toward the machine axis (centering force); F_v = vertical load tending to separate the top half of a TF coil from the bottom half (sum of tension in inboard and outboard legs at the mid-plane); and M_r = overturning moment on a TF coil about the r axis due to the interaction of the TF coil current with the poloidal field. The figures are drawn to scale and indicate the similarity in machine size; note, however, that the stored energy and loads differ by factors of the order of two. This is primarily due to the differences in field level, bore size and average radius. The differences in overturning moment are also due to these factors and to differences between PF systems.

Figure 5.2 summarizes the megampere turns in each of the PF coils at the start of burn and with the plasma current indicated. Vectors are drawn to scale on each PF coil to illustrate the local load per unit coil circumference due to the PF system and the plasma. These loads are axially symmetric and uniformly distributed. In addition, the PF coils (ring coils in particular) experience a spatially periodic load (not shown) due to the ripple and stray field from the toroidal field coils.

Fig. 5.2 - EM loads per unit length on PF coils at start of burn with plasma; forces are to scale and values are megamp-turns in PF coils

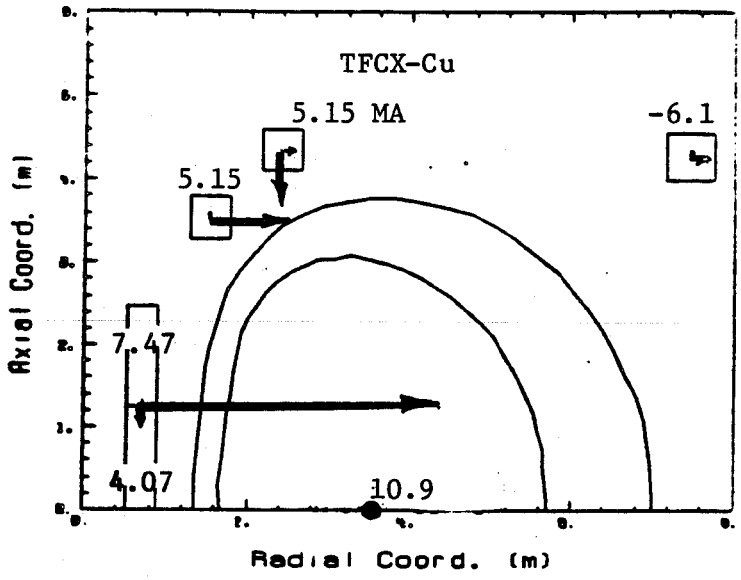

TFCX - SUPERCONDUCTING

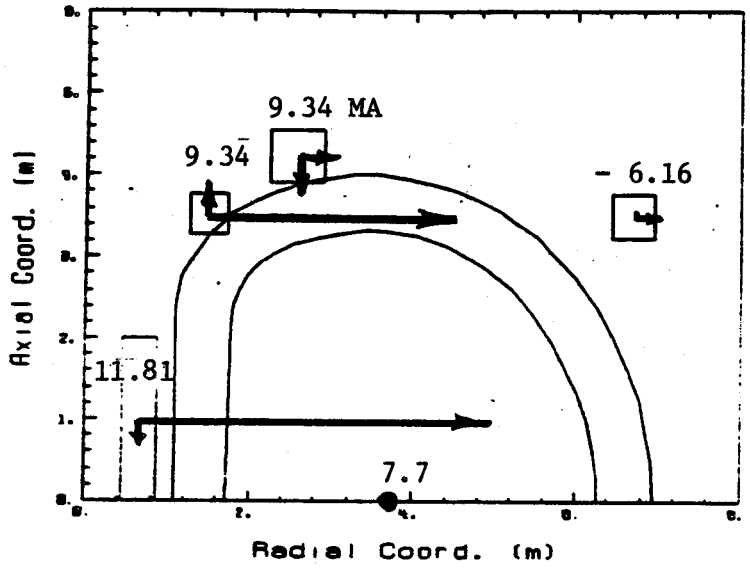

TFCX - HYBRID

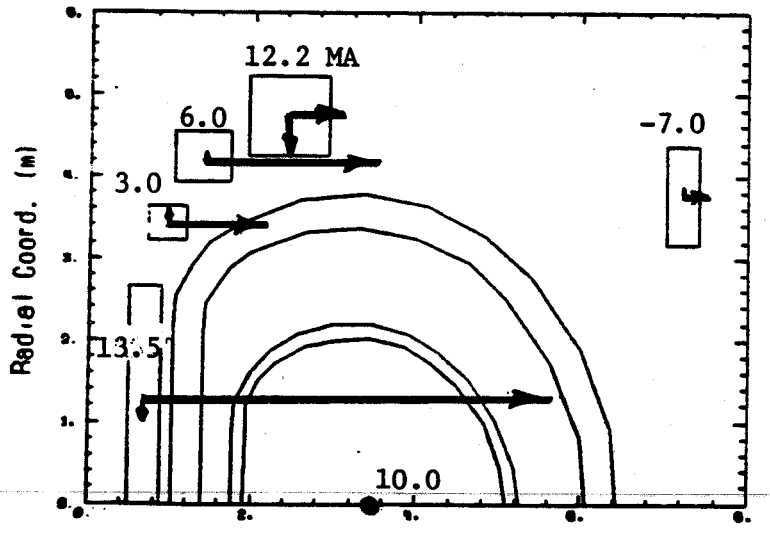

The OH solenoid in the top figure consists of two coils with the MAT distribution shown so that there are 5 coils with mirror images below the z = 0 plane in the top system. There are 4 PF coils (8 total) in the superconducting system in the center sketch and 5 PF coils (10 total) in the hybrid system in the lower figure. The machines are close to the same size and represent different stages in three designs on the way toward satisfaction of the same physics mission, but the load patterns are similar and of the same order of magnitude although differences of order 2-3 are evident. These differences between options as well as those for the TF coils are partially due to the fact that all three cases have not been optimized to the same level. They all represent load levels which are feasible from the engineering standpoint.

5.2 Fault Conditions

The only fault conditions considered in this preliminary study were changes in electromagnetic loads due to abnormal current distributions in the coil systems. The conditions illustrated in Figs. 5.1 and 5.2 were assumed to be the usual or "normal" operating conditions. Excursions from these current distributions among coils were then postulated in the form of discharging one (or more) coils and the plasma, then finding the new coil currents assuming their circuits maintained a constant flux condition. The new currents were then used to recalculate the load patterns and to ratio the resultant forces to their counterparts under usual operating conditions. The ratios then indicate when a load exceeds the usual operating conditions (i.e.- ratio > 1) or when it reverses direction relative to the usual condition (i.e. ratio < 0).

5.2.1 PF Fault Influence on PF Coils

The first class of conditions considered in this part of the study assumed that each PF coil pair (one above and one below the z = 0 plane) was in an independent circuit since it would be likely that independent control for plasma shaping and other experiments would be necessary. One circuit (and the plasma) are then discharged to zero because of a fault in that circuit and the others are assumed to maintain constant flux. This is a symmetric PF coil fault since a pair of coils is discharged and field symmetry with respect to the z = 0 plane is retained. A typical result is illustrated in Fig. 5.3 which shows one of the ring coil pairs (shaded) discharged to zero current. The number adjacent to the other coils is the ratio of the final to initial current in that circuit based on a constant flux assumption. In all three cases, discharging the coil shown leads to current increases in the inboard coils and a decrease in the outboard coils. The latter occurs because the outboard coils carry a current of opposite sign under usual conditions (see Fig. 5.2). Two questions now arise: (1) are the individual coil loads now greater than or reversed in sign relative to those under the usual condition, and (2) is the change in current level sufficient to induce a normal region in a coil which is still "on" because its critical current is exceeded?

Cases were considered where each of the circuits was symmetrically discharged as described earlier and two sample cases were considered where only one coil (e.g. - above the z = 0 plane) was discharged to gain insight into an asymmetric fault. For each case and each coil, the ratio of final to initial current was calculated together with the ratios of final to initial radial and axial forces. Initial states were as defined in Fig. 5.2 and results are summarized in Tables 5.1 and 5.2 with coils denoted as in Fig. 5.4.

Fig. 5.3 - Typical case of symmetric PF coil fault and PF circuit current changes

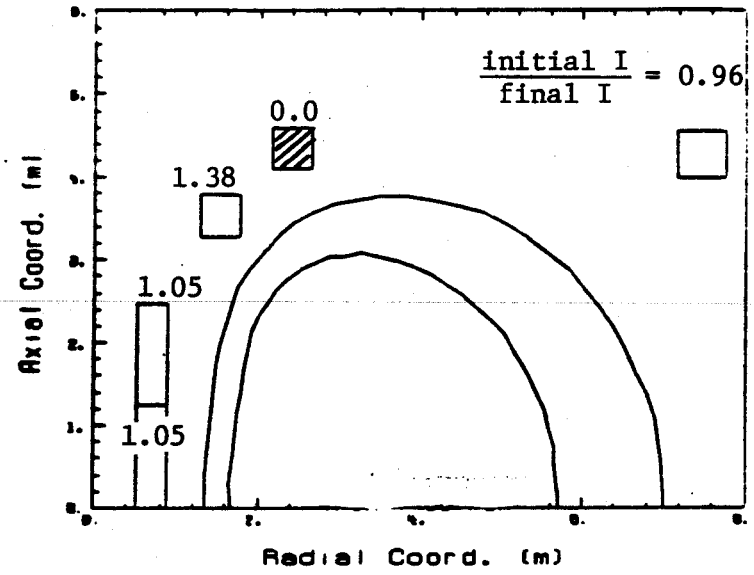

$$\left.\frac{M_{rf}}{M_r}\right|_{TF} = 1.24$$

TFCX - SUPERCONDUCTING

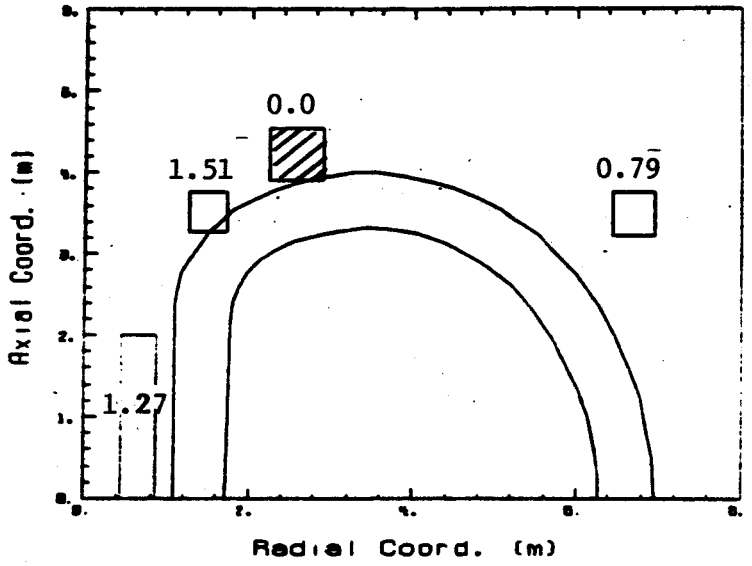

$$\left.\frac{M_{rf}}{M_r}\right|_{TF} = 1.52$$

TFCX - HYBRID

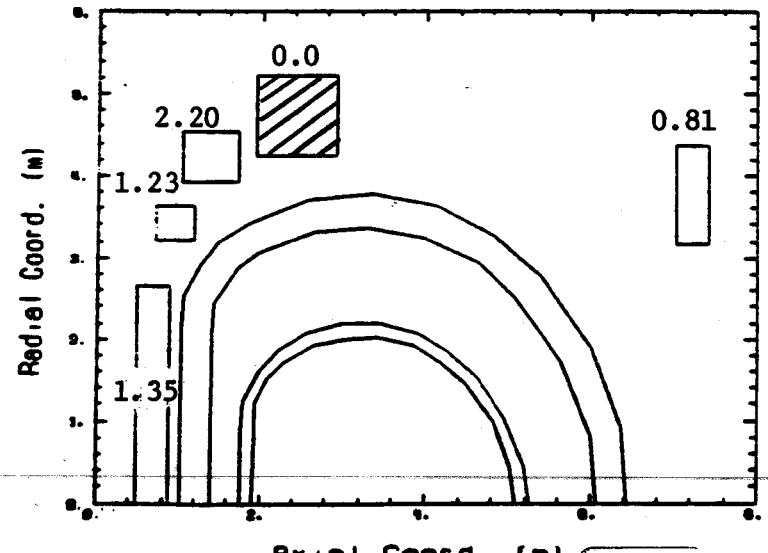

$$\left.\frac{M_{rf}}{M_r}\right|_{TF\ SC} = 1.76$$

$$\left.\frac{M_{rf}}{M_r}\right|_{TF\ Cu} = 0.74$$

Fig. 5.4 - PF coil designations for fault study responses (Table 5.1)

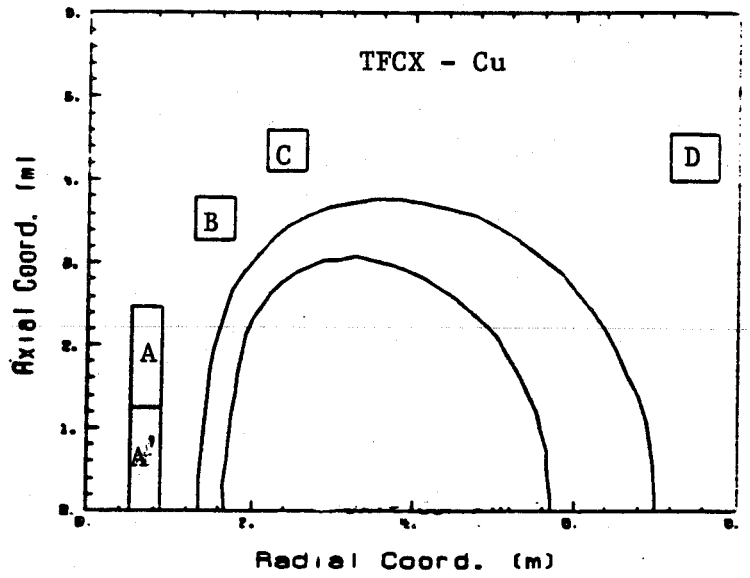

TFCX - SUPERCONDUCTING

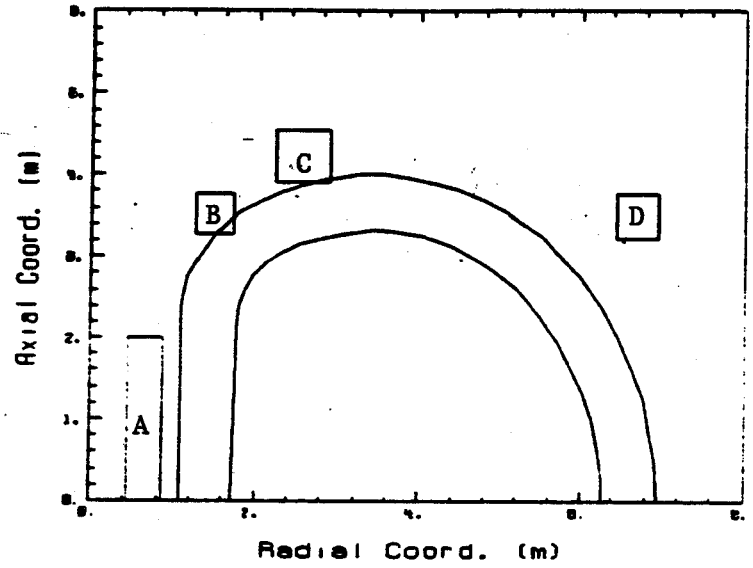

TFCX - HYBRID

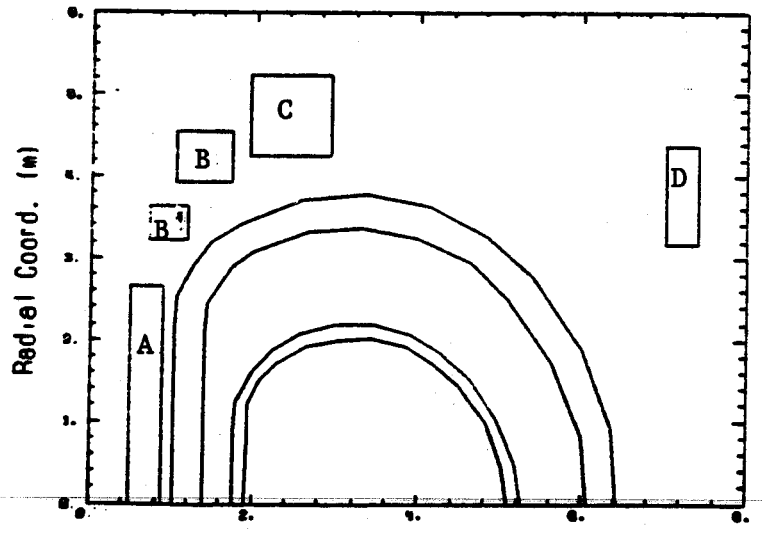

TABLE 5.1

RATIO OF NUMBER OF "LARGE" EXCURSIONS* TO NUMBER OF FAULTS FOR PF INTERACTIONS WITH PF COILS

SYSTEM	FAULT FACTOR	COIL DESIGNATION A'	A	B'	B	C	D
COPPER	F_R	0	0	NA	0	2/5	0
	F_Z	4/5	4/5	NA	3/5	0	4/5
	I_R	1/5	2/5	NA	1/5	1/5	0
SUPERCONDUCTING	F_R	NA	0	NA	0	2/5	0
	F_Z	NA	3/5	NA	2/5	0	4/5
	I_R	NA	2/5	NA	1/5	1/5	0
HYBRID	F_R	NA	1/6	3/6	1/6	3/6	0
	F_Z	NA	1/6	3/6	3/6	0	5/6
	I_R	NA	4/6	4/6	2/6	1/6	0

NA = Coil not in system (See Fig. 5.4).

* = "Large" Excursion, implies a case where a ratio was greater than unity or less than zero; the corresponding range of the ratios in each case is given in Table 5.2.

NUMBER OF FAULTS =
- 5 = 5 symmetric for Cu option
- 5 = 4 symmetric + 1 asymmetric for SC option
- 6 = 5 symmetric + 1 asymmetric for hybrid option

TABLE 5.2

RANGE OF FAULT FACTORS FOR PF INTERACTIONS WITH PF COILS

SYSTEM	FAULT FACTOR	COIL DESIGNATION A'	A	B'	B	C	D
COPPER	F_R	0	0	NA	0	-0.26,-0.22	0
	F_z	-3.5,2.51	-4.17, 1.8	NA	2.67,12.6	0	-1.14,-0.99
	I_R	1.34	1.12,1.17	NA	1.38	1.2	0
SUPERCONDUCTING	F_R	NA	0	NA	0	1.55, 2.59	0
	F_z	NA	1.5, 2.15	NA	-0.42,1.77	0	-2.17,-0.96
	I_R	NA	1.27, 1.3	NA	1.51	1.29	0
HYBRID	F_R	NA	1.13	1.36,1.59	1.29	1.23, 1.8	0
	F_z	NA	1.76	1.76,2.38	-3.75,3.28	0	-5.19, 4.08
	I_R	NA	1.15,1.35	1.23,1.86	1.19, 2.2	1.2	0

NA = Coil not in system (see Fig. 5.4)

Three ratios or fault factors were evaluated. In summarizing results in Tables 5.1 and 5.2, excursions in forces or currents which were greater than 10% (i.e. - fault factor > 1.1) were considered "large" as well as cases where force directions reversed (i.e. - force fault factor < 0). The former implies a potential problem in terms of exceeding the critical current or structural capability and the latter implies a reversal in load direction relative to the usual case (Fig. 5.2). The coil designators in Table 5.1 correspond to those in Fig. 5.4 and the table summarizes the number of "large" excursions in force or current experienced by the coils relative to the number of faults considered. Table 5.2 gives the range of the ratios for the calculated faults in each case. Since the number of fault conditions was limited and the three systems were not initially optimized to the same level, the systems should not be compared, but certain common trends are indicated:

(a) all coils except the outboard ring coil experienced substantial changes in current relative to their operating levels.

(b) coils can experience loads which are significant multiples of their usual loads or load reversals under selected conditions.

Although the excursions are large, they should be considered manageable from the design standpoint provided a sufficiently thorough fault condition analysis is ultimately performed and protective circuits are employed if required.

Sixteen fault conditions were considered relative to usual operating conditions at start of burn. Other points in the start-up, burn and shut-down scenario require analysis at a later stage in design and could yield fault factors which meet or exceed the ranges given. The process is straightforward, but tedious, and requires development of codes which

can allow a large number of cases to be treated without the interactions now required for transcription and reduction of inputs and outputs.

5.2.2 PF Fault Influence on TF Coils

Under usual operating conditions in a symmetric system, the PF interacts with the TF coils such that each TF coil experiences out-of-plane forces which have no resultant, but which generate a moment about the r-axis in its plane. This is illustrated in the top sketch in Fig. 5.5 and in the event that a symmetric PF coil system fault occurs, the magnitude of this moment will change. For example, Fig. 5.3 gives the ratio of the overturning moment on a TF coil for the PF coil fault indicated to the value of the overturning moment under usual conditions. As shown, the ratios are typically of order 1 to 2. These moment ratios were found to exceed unity in five out of the fourteen symmetric fault conditions considered.

In the event that an asymmetric PF coil fault occurs, the out-of-plane forces will change such that the overturning moment discussed earlier will change and the forces will have a resultant through the machine axis. This is shown in the center sketch in Fig. 5.5. There is, therefore, no net moment about the machine axis, but the resultant is equivalent to the case in the lower sketch which shows a net out-of-plane force at the average coil radius and a z-directed moment about an axis parallel to the z-axis and located at the average radius. To illustrate the relative magnitude of this type of fault, two sample cases with asymmetric PF faults were calculated. They indicated that the resultant out-of-plane force was a few percent of the net centering force under usual operating conditions and that M_{za} as defined in the lower sketch in Fig. 5.5 was 25-35% of M_r under usual conditions. Loads of this magnitude are nontrivial and indicate the need for considering a broad range of faults at some later time; however, they are not so large as to imply lack of

Fig. 5.5 - Illustration of PF interactions with a TF coil.

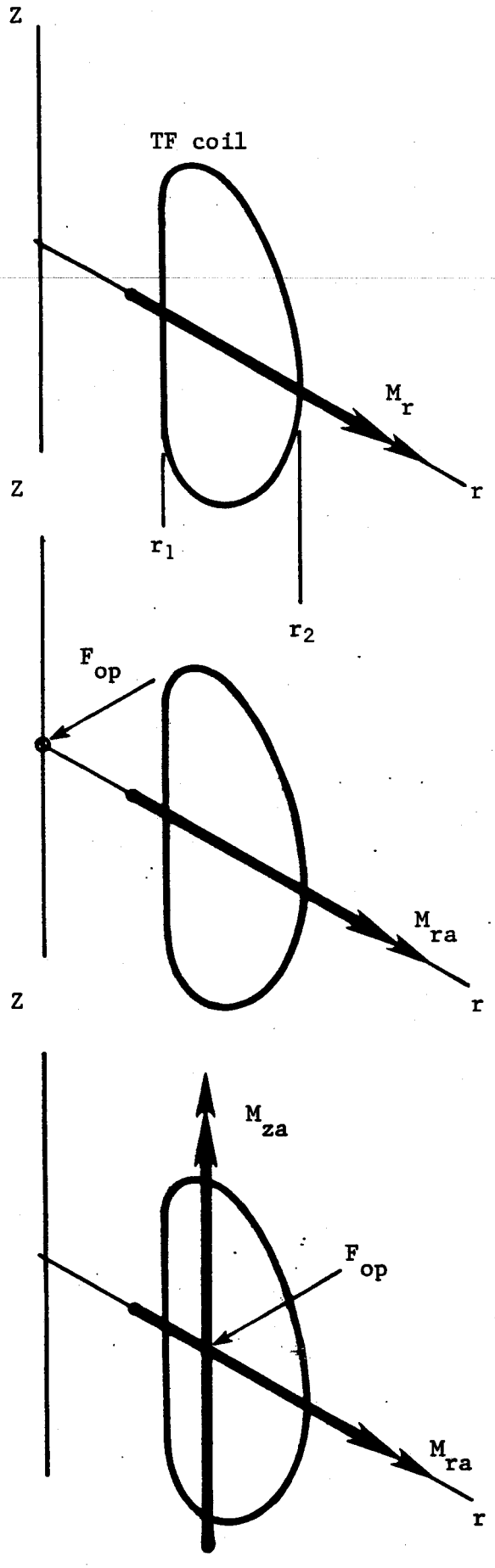

- symmetric PF produces moment M_r under usual conditions

- symmetric PF coil fault changes M_r

- asymmetric PF coil fault changes M_r to M_{ra}

- asymmetric PF coil fault gives net out-of-plane force through z - axis resulting in no moment about the z-axis

- above figure is equivalent to resultant F_{op} at $(r_1+r_2)/2$ and a moment = F_{op} $(r_1+r_2)/2$ but the choice of radius to F_{op} can be arbitrary

feasibility. As in the previous section, a sufficient number of faults was not investigated to indicate a trend between options nor were the initial designs optimized. However, results imply a need for thorough fault analysis and definition of load excursions for consideration in the design process.

5.2.3 TF Fault Influence on TF Coils

The magnitude of fault loads in the TF system were estimated for one case in the TFCX Cu option. This was an extreme situation in which one coil was completely discharged while the others altered their current to maintain constant flux linkage. The result is that:

(a) the coil adjacent to the discharge coil experiences a net out-of-plane force comparable in magnitude to the centering force it experiences during usual operation;

(b) the current in the remaining coils increases about 7%;

(c) the centering force on the coil adjacent to the discharged coil rises less than 1% and the total vertical load in the coil legs at the mid-plane falls to about 70% of the value before the load.

Item (a) is by far the most significant since a TF coil in a symmetric PF experiences no net out-of-plane loads under usual conditions. However, this type of result is common among options, so it will require further consideration during design when it must be determined to be either: (1) a condition with vanishing probability because of system configuration; or (2) an allowable overload for a specified number of fault cycles.

5.2.4 TF Fault Influence on PF Coils

The change in loads on the PF coils due to TF coil faults were not calculated for the TFCX options. In general,[2] a TF coil system fault which is symmetric relative to the machine axis will alter the load distribution and the associated local bending moments on a PF coil. If the TF system fault is asymmetric, a PF coil could also experience a moment tending to rotate it about a line which passes through the machine axis and the faulted coil, as well as a net force in its plane.

5.3 Summary

This study represents the first step fault analysis for TFCX and indicates that ratios of fault currents and loads under selected conditions are nontrivial; however, no fundamental advantage was apparent among the copper, superconducting and hybrid options considered. This was partially due to the limited number of cases (17) considered, partially due to the fact that fault factor ratios are probably similar in devices of similar size and field level, and partially due to the differences in level of design detail available for the cases considered. In general, it will be necessary to evaluate a much larger number of cases at a later stage in the design. The process is straightforward, but the codes required for systematic evaluation, transcription of inputs/outputs and summarizing fault factors need further development.

5.4 References for Chapter 5

1. "TFCX - Preconceptual Design Report - Vol. I, II," PPPL, F-Axxx-8407-006, F-Axxx-8407-007, July 1984.

2. R.J. Thome, J.M. Tarrh, "MHD and Fusion Magnets:Field and Force Design Concepts, Wiley, 1982, p. 198.

6.0 SAFETY RELATED EXPERIMENTS

6.1 ICCS Small Football Coil - J.V. Minervini and P. Rezza

A small football coil made of internally-cooled cabled superconductor (ICCS) was constructed in 1983 and safety related experiments were performed in March 1984. The coil was originally constructed to measure the effects of strain, cyclic fatigue, and conductor motion on the conductor characteristics including critical current and stability. The tests described here were performed to investigate failure mechanisms in coils wound with ICCS conductors.

The coil and conductor were described in the FY83 Report[1] but the characteristics are repeated here for convenience. The conductor was made up of a 27 strand cable of bronze matrix Nb_3Sn in a sheath of JBK-75 superalloy. The conductor characteristics are summarized in Table 6.1 and a photograph of the conductor cross section is shown in Fig. 6.1. The coil and mandrel are shown in schematic in Fig. 6.2. The photograph in Fig. 6.3 shows the coil with the side support plates in place but for the tests described here the plate on the side opposite the terminations was removed. This was done in order to increase the chance for failure.

The experiments were performed in a uniform DC background field provided by the 6-inch bore Bitter magnet at the Francis Bitter National Magnet Laboratory. The test consisted of three parts:

(1) measurement of critical current
(2) measurement of quench voltage and pressure
(3) attempt to quench to failure of the winding

TABLE 6.1

SMALL FOOTBALL COIL CONDUCTOR PARAMETERS

Material	Nb_3Sn, Copper Stabilized
Cu: Noncopper Ratio	1.8
Void Fraction	32%
Sheath	JBK - 75
Sheath Wall Thickness	0.015 in. (0.38 mm)
Sheath Dimensions	0.192" x 0.192" sq. (4.88 mm sq)
Strands	27
Strand Diameter	0.7 mm

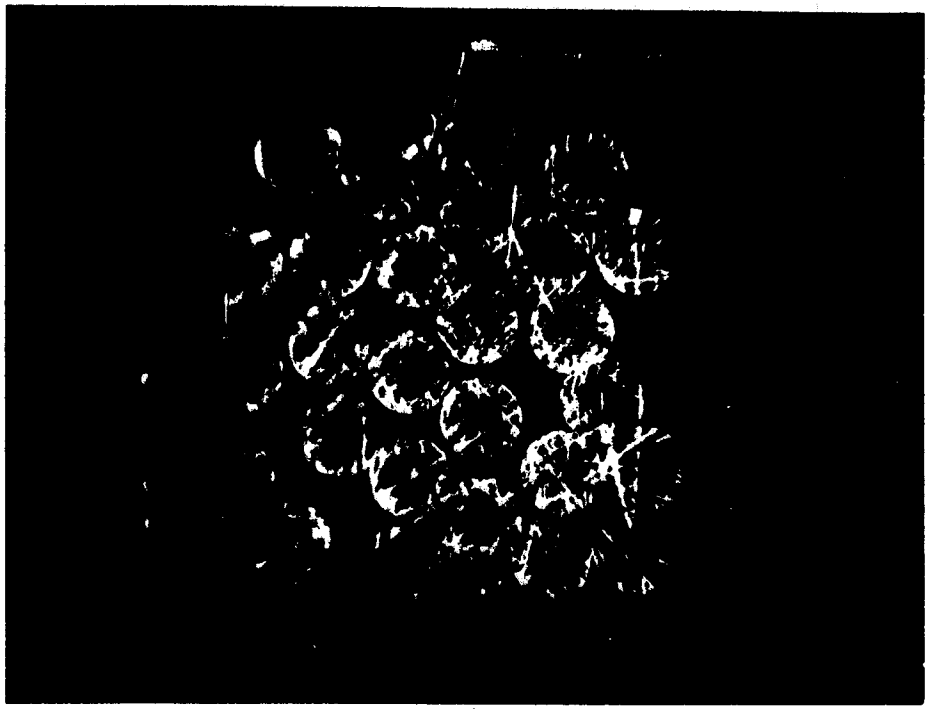

Figure 6.1 Cross section of conductor used in small football test.

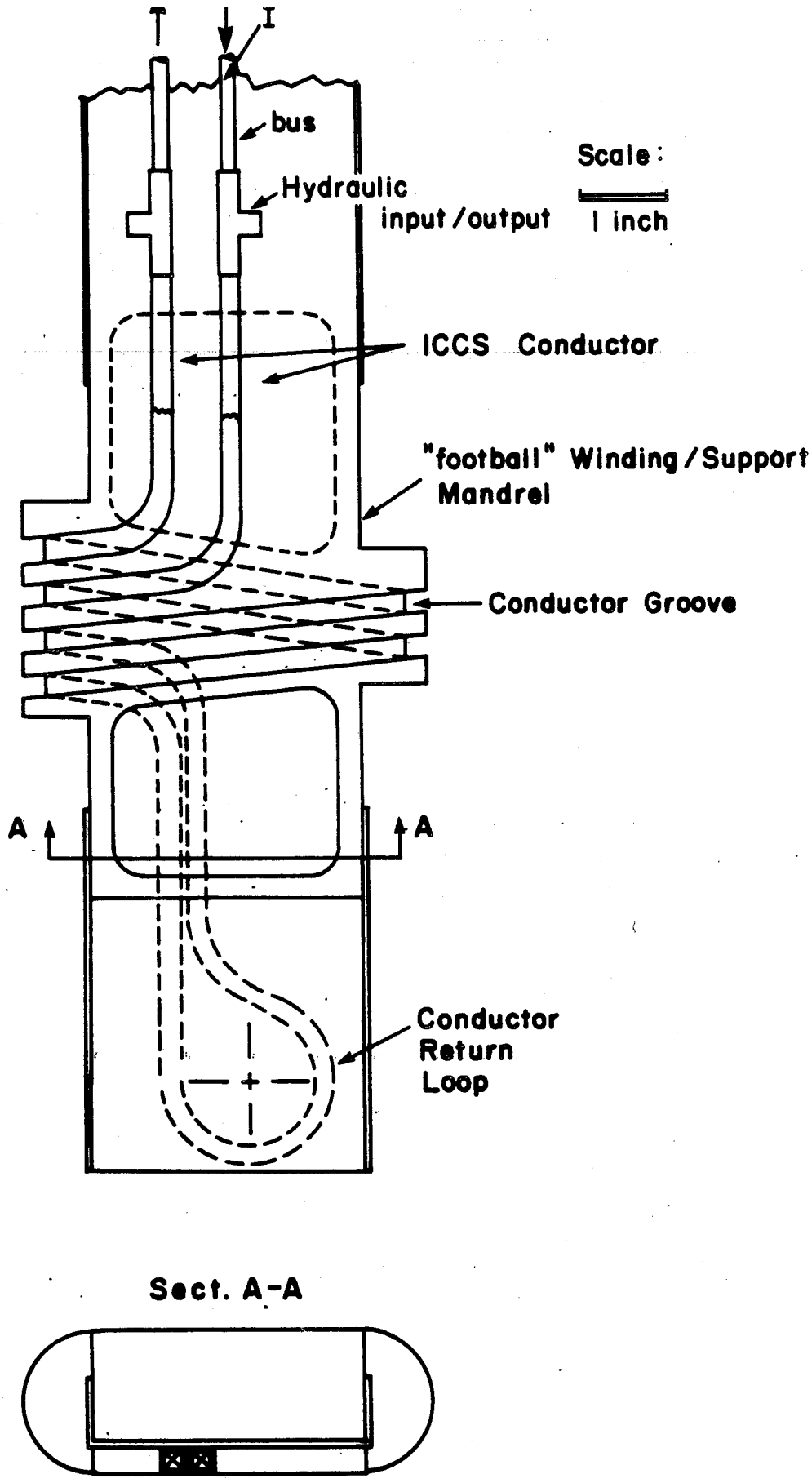

Figure 6.2 Outline of mandrel for small football test.

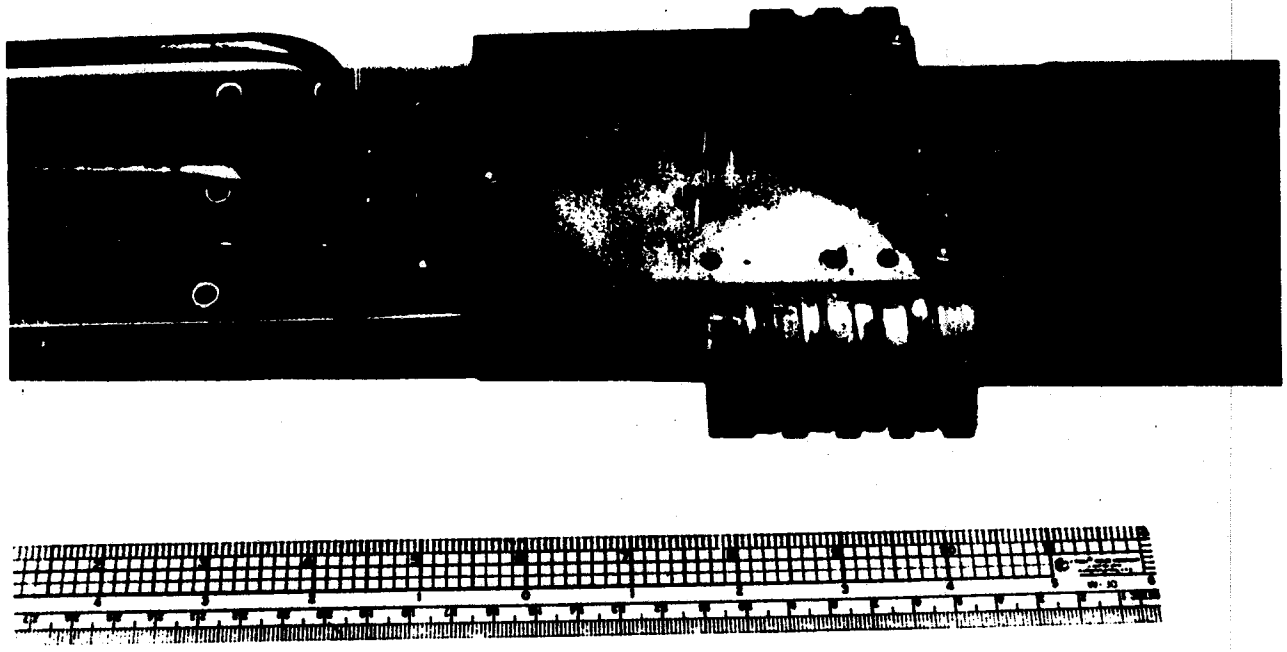

Figure 6.3 Photo of small football coil wound on mandrel with side support plates in place.

A schematic of the helium flow configuration is shown in Fig. 6.4 and a schematic of the instrumentation set-up is shown in Fig. 6.5.

6.1.1 Measurement of Critical Current

The critical current as a function of field was measured in order to compare with data taken previously. Apparently the critical current varied somewhat between experiments and so the I_c versus B measurements were taken to get a datum. The results are shown in Fig. 6.6. The data of this experiment (3/14/84) compare very well with the most recent data taken on 11/29/83 even though one support plate had been removed for this test. Both sets of data are slightly higher than that taken on 11/25/83. This is probably not significant. In all cases the data were recorded on an x-y recorder using an electric field criterion of 1.5 μV/cm to determine the critical current.

6.1.2 Measurement of Quench Voltage and Pressure

A principal goal of this test was to measure pressure in the coil during a quench. The peak quench pressure could have a significant impact on any magnet design since it could determine the maximum helium flow length and if the coil is connected to a refrigerator, the sudden expulsion of high pressure helium could have serious consequences for the turbo-expander. These units are delicate and expensive and would have to be protected from pressure surges by check valves and expansion chambers.

Of course the ultimate coil failure would be caused by the pressure bursting the conduit or one of the many joints in the helium flow path. The maximum quench pressure can be estimated from an expression given by Miller and Lue[2]:

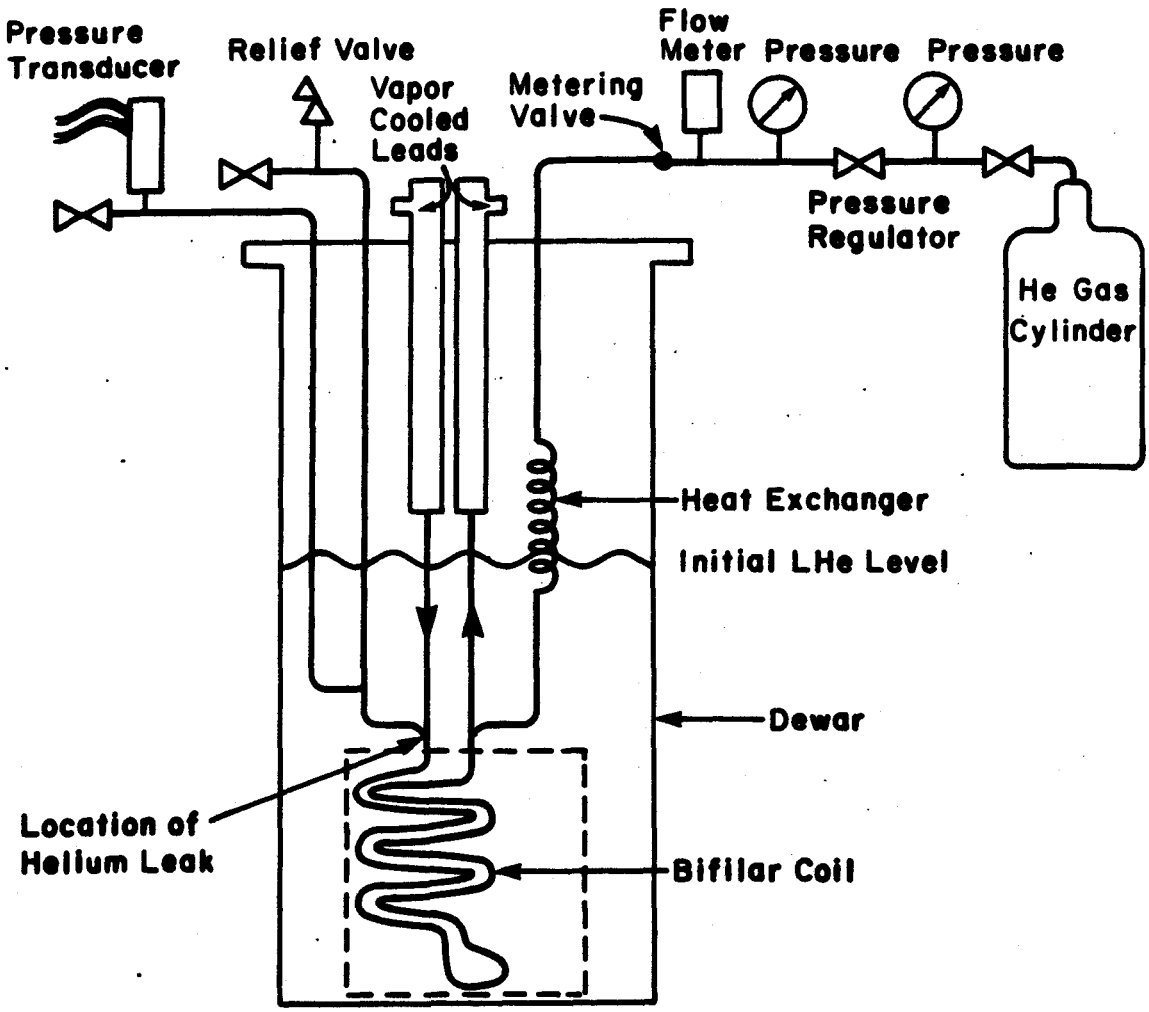

Fig. 6.4 Schematic of helium flow path for small football coil test.

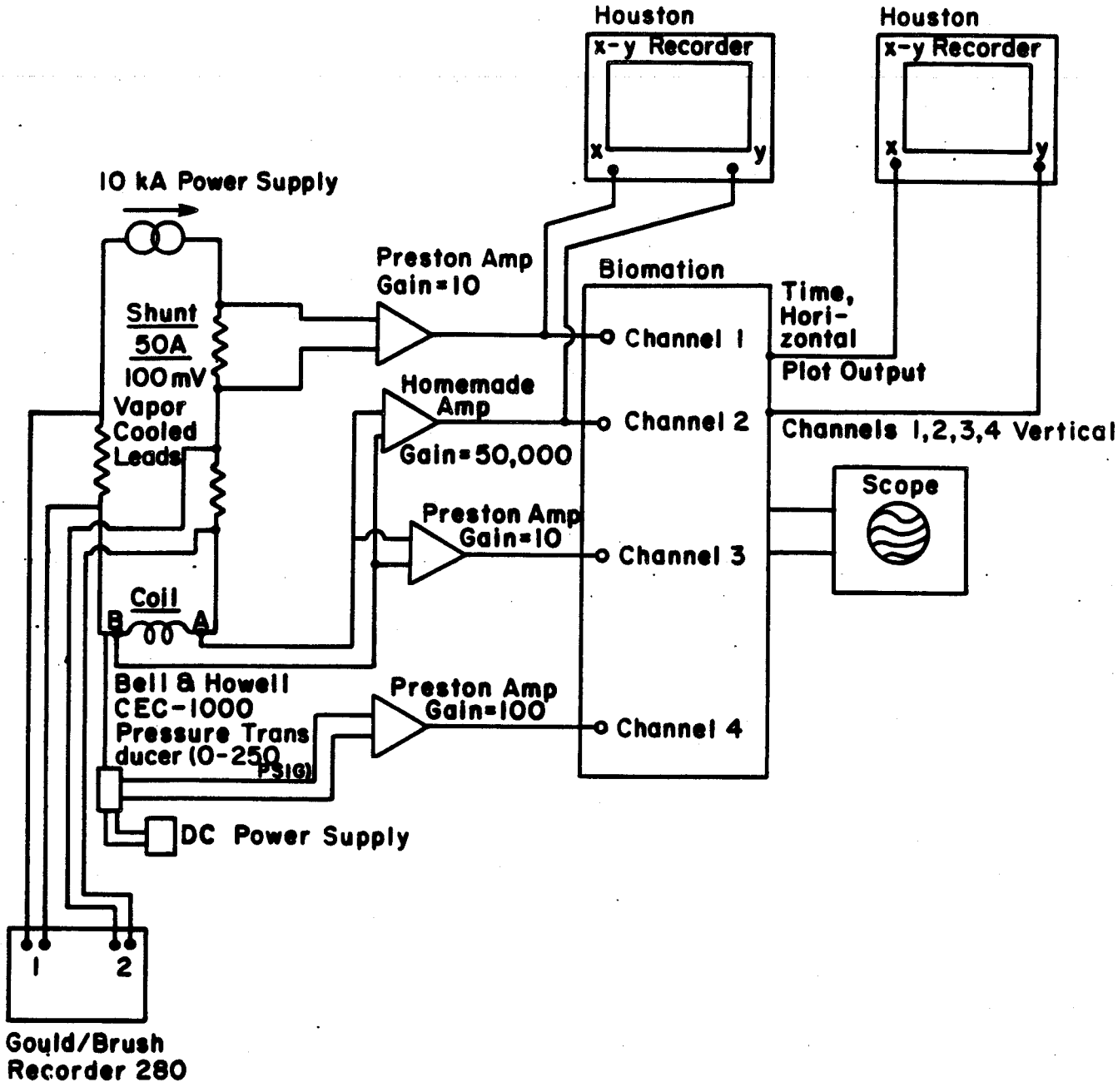

Fig. 6.5 Schematic of experimental set-up.

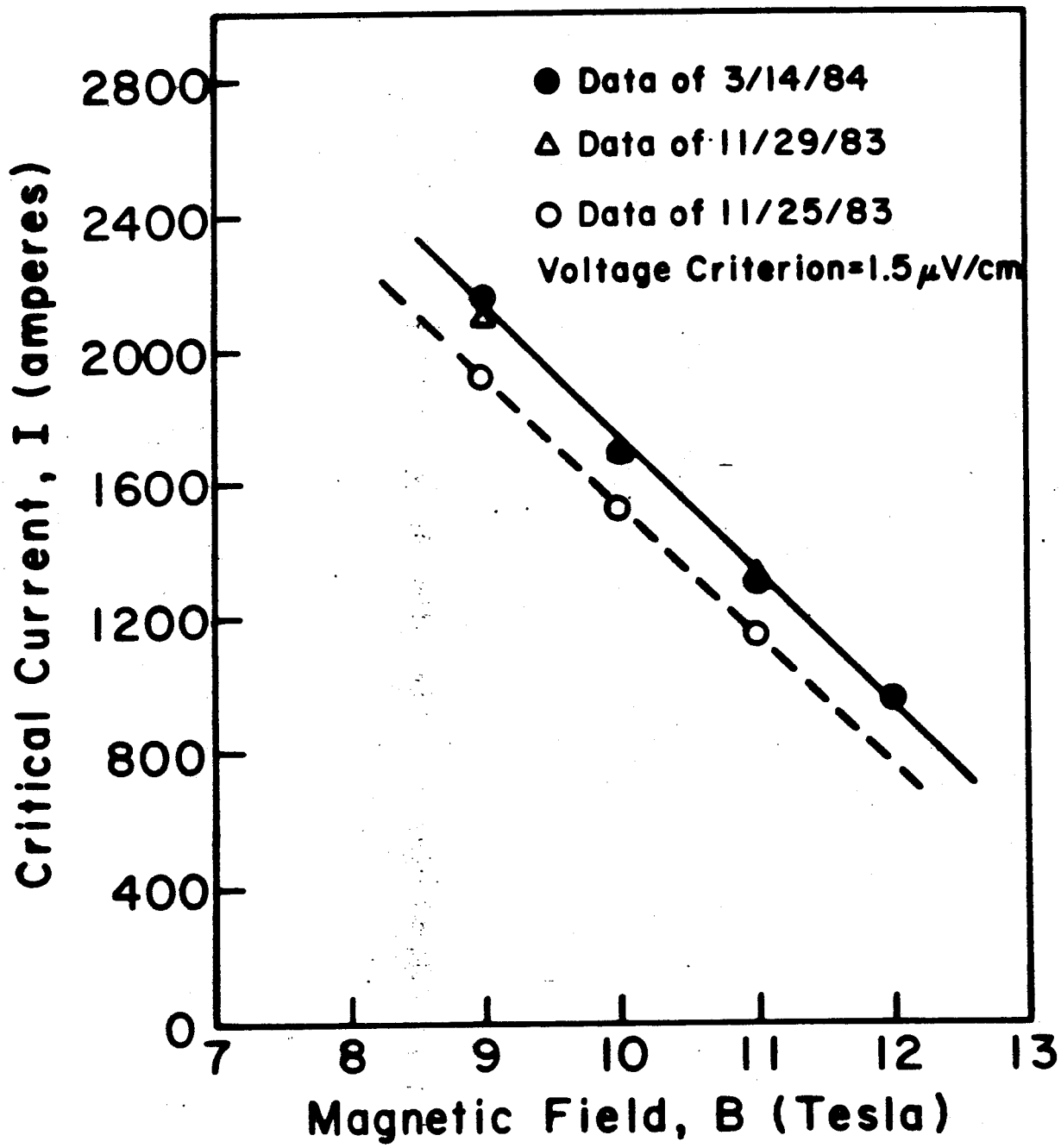

Fig. 6.6 Critical current results of small football coil.

$$P_{max} = 0.10\left(\frac{Q^2 \ell^3}{D_h}\right)^{0.36}$$

where Q is the initial joule heating rate per unit volume of helium (watts/m^3), ℓ is the half-length of the flow path (m), and D_h is the hydraulic diameter (m). Calculations for full scale magnet designs have indicated that maximum quench pressures could be as high as several hundreds of atmospheres, implying the possible need for periodic pressure relief devices along the flow length.

When this test coil was designed no provisions were made for measuring the pressure in the conduit, hence the add-on instrumentation was less than optimum for this experiment. In addition, a significant problem arose because of a leak that developed in the helium flow circuit at the exit tee on the coil termination. It was in such a position that it could not be adequately sealed. This prevented operation of the coil at the design pressure of 2.5 atmospheres absolute. This pressure was chosen in order to keep the helium in the conduit in the supercritical region. However, this pressure had to be throttled down to something closer to one atmosphere to prevent the warm helium pressurized from the gas bottle from boiling off a significant amount of external liquid helium. The significance of this is that the initial helium state is different than the design condition and thus the thermodynamic history of the fluid follows a path that differs from the modeled path, the final result being that the expression for the maximum quench pressure should not necessarily predict the actual maximum pressure, but probably something higher.

The data were taken over four different current ramps called Events A through D. All data were taken at a magnetic field of 12 tesla in order to keep the critical current low and thus not push the vapor-cooled current leads above their rating of 2,000 amperes. The scenario for the first two events, A and B, was to increase the current in the coil past the critical current and hold it at a fixed coil voltage level until the coil quenched. The circuit breakers were opened when the coil resistance became large enough to cause the current to decrease due to voltage limiting of the power supply. During this period the current, voltage across the entire coil, and pressure at the helium outlet were monitored with the experimental set-up shown in Fig. 6.5. Voltage across the entire coil was monitored on two different channels of the digital waveform recorder to see the event with a fine and a coarse resolution simultaneously. The voltage drops across the vapor-cooled leads were monitored continuously on a brush strip chart recorder in order to insure that they were in no danger of thermal runaway.

The data taken during Event A are shown in Fig. 6.7, which are photographs of the oscilloscope traces on an expanded time scale (SX). The current dropped off from 1046 A to 894 A before the breakers were opened. Voltage across the coil at this point was approximately 0.12 volts. The pressure as a function of time is shown on Channel 4. Before thermal runaway the pressure had a steady average value of about 0.4 psig with a oscillation superimposed of about 1.4 psi at a frequency of about 1 Hz. The pressure oscillation was caused by the steep temperature gradient in the pressure sensing tube between room temperature and the liquid helium.[3,4] In addition to decreasing pressure measurement accuracy, the

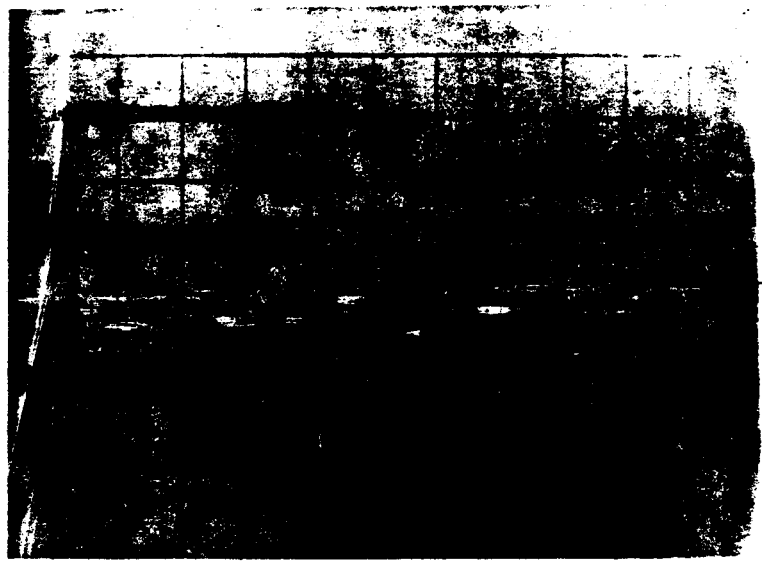

Scales

1	I = 1000 A/Div
3	V = 100 mV/Div
4	P = 3.5 psig/Div
t	4.096 s/Div

Fig. 6.7 Coil current, voltage and pressure traces as a function of time during Event A.

pressure oscillations cause vastly increased heat-leak to the liquid helium. It would be necessary to operate the pressure transducer in the cold region in order to eliminate the oscillations.

The pressure began to rise at the start of the voltage increase on Channel 3 and approached a maximum at about the same time the breakers were opened. The maximum average pressure is about 3.5 psig. The decay time for the pressure is about 30 seconds. The asymptotic steady-state pressure is approximately 0.4 psig less than the pressure when operating at 1046 A. It is interesting to note that after the initial current decay, the resistance change appears to decrease significantly. This may be caused by coil turns shorted to the mandrel.

The scenario for Event B was similar to Event A (Fig. 6.8) except that once thermal runaway began, the breakers were not opened until 11.5 seconds after the initial voltage rise (approximately 2 times the heating of Event A). In this case, current dropped from 1080 A to 937 A and the peak voltage was extrapolated to be about 0.3 volts. It is clear in this case that the pressure peaked before the breakers were opened. The decay time for the pressure was on the order of 80 seconds.

In Event C (Fig. 6.9), the quench began at a current of 1145 A and decayed to 785 A when the breakers were opened after 65 seconds. The pressure appeared to reach an initial average level value of 4.2 psig with a large oscillation of about 4 psig peak to peak, followed by a slow increase to an average pressure of about 7-8 psig which remained steady (with large superimposed oscillations) for a good 60 seconds after the breakers were opened. The decay took an additional 1.5-2.0 minutes. Thus

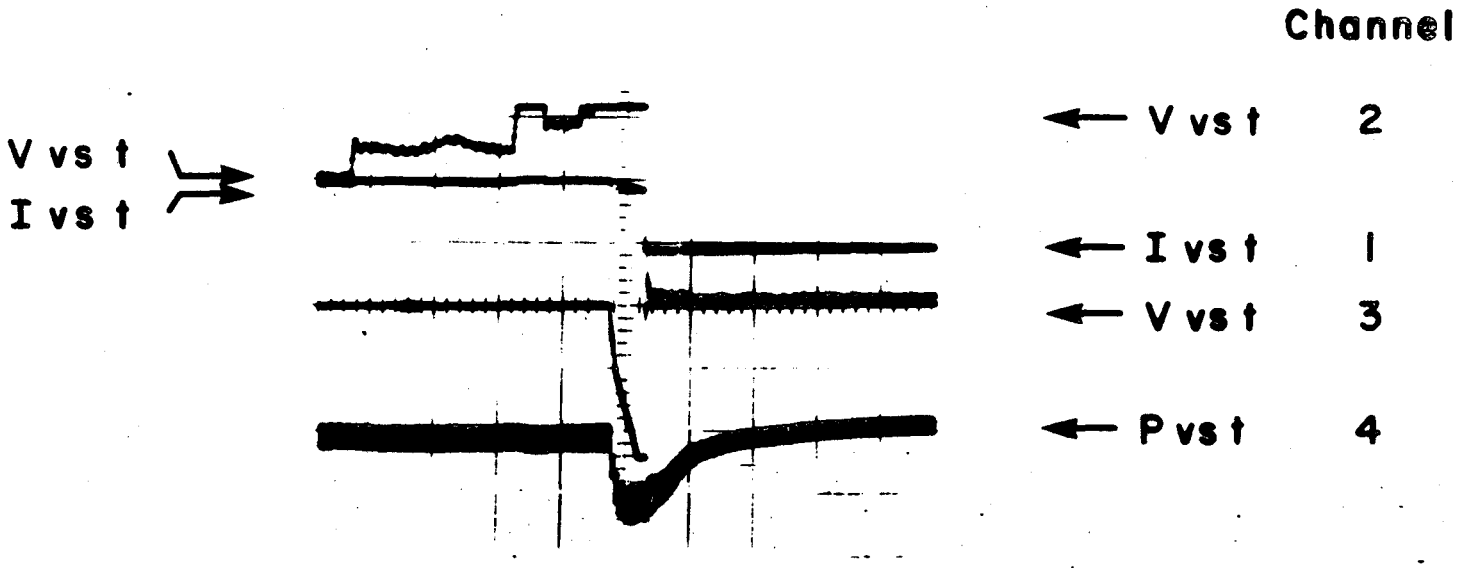

Scales

1	I = 1000 A/Div
2	V = 80 μV/Div
3	V = 100 mV/Div
4	P = 3.5 psig/Div
t	20.48 s/Div

Fig. 6.8 Coil current, voltage, and pressure traces as a function of time during Event B.

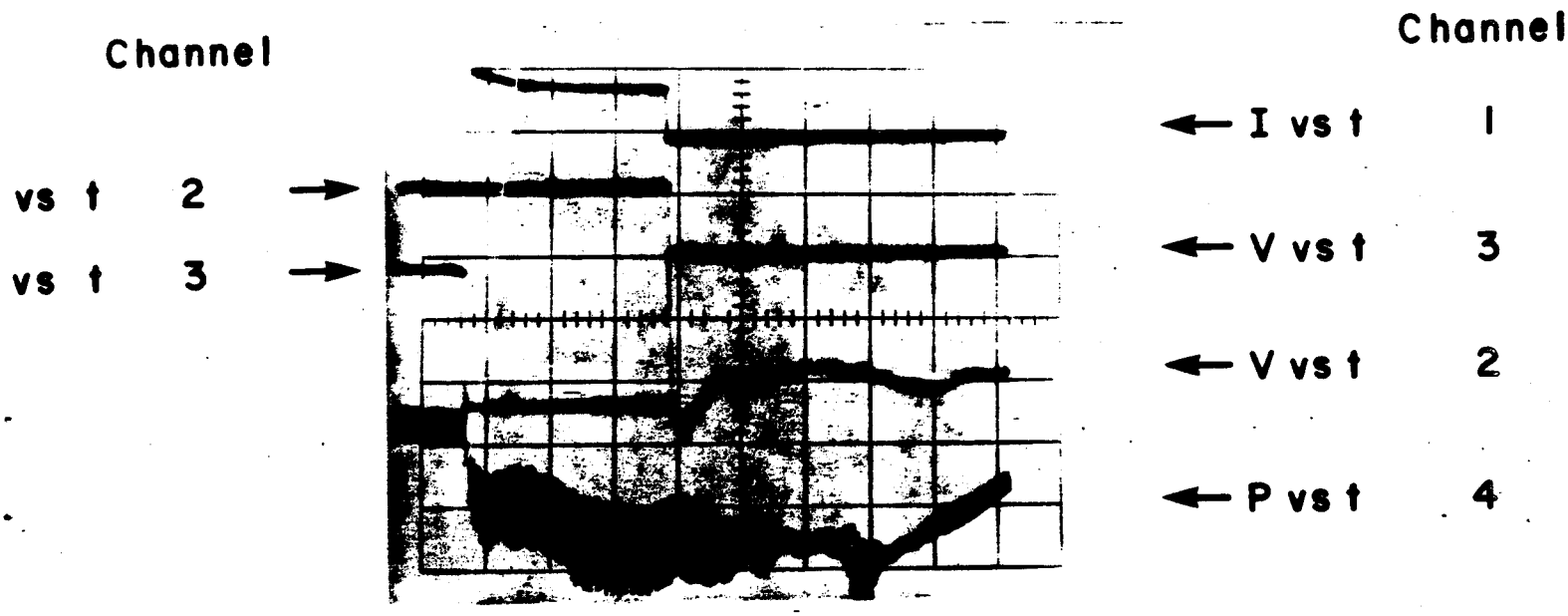

Scales

1	I = 1000 A/Div
2	V = 80 μV/Div
3	V = 200 mV/Div
4	P = 3.5 psig/Div
t	20.48 s/Div

Fig. 6.9 Coil current, voltage, and pressure traces as a function of time during Event C.

the total disturbance lasted on the order of 4 minutes after heating began. This large quench resulted in boiling off most of the helium in the dewar. At the end of this event only a small amount of helium remained near the bottom of the coil center cross-over turn with the bulk of the coil uncovered by liquid.

6.1.3 Attempt to Quench to Failure of the Winding

As a final test an attempt was made to cause the winding to fail, either by overheating the conductor (burnout) or overpressurizing the conduit or joints (blowout). This attempt was called Event D.

The scenario was to energize the coil and leave the current on until it burned out. In actuality, close monitoring of the vapor-cooled lead voltage indicated a possibility of lead failure so the run was aborted on this basis. Total time for initial current ramp to breakers opening was 253 seconds (4.2 minutes) with heating occurring for about 183 seconds (3.1 minutes).

A portion of Event D is shown in Fig. 6.10. There appeared to be a slight pressure rise with the current at 1050 A followed by a rapid increase when the current was increased to 1140 A. Thermal runaway occurred at this point followed by a decay of the current to about 700 A. The instrumentation saturated at a pressure of about 14 psig. However, the maximum pressure was probably on the order of 20 psig. The entire event was too long for the Biomation to capture with the given settings.

The event was ended when the voltage began to run away on the vapor cooled leads. A trace of voltage versus time is shown in Fig. 6.11. One of the leads took most of the flow resulting in the other lead (Channel 1)

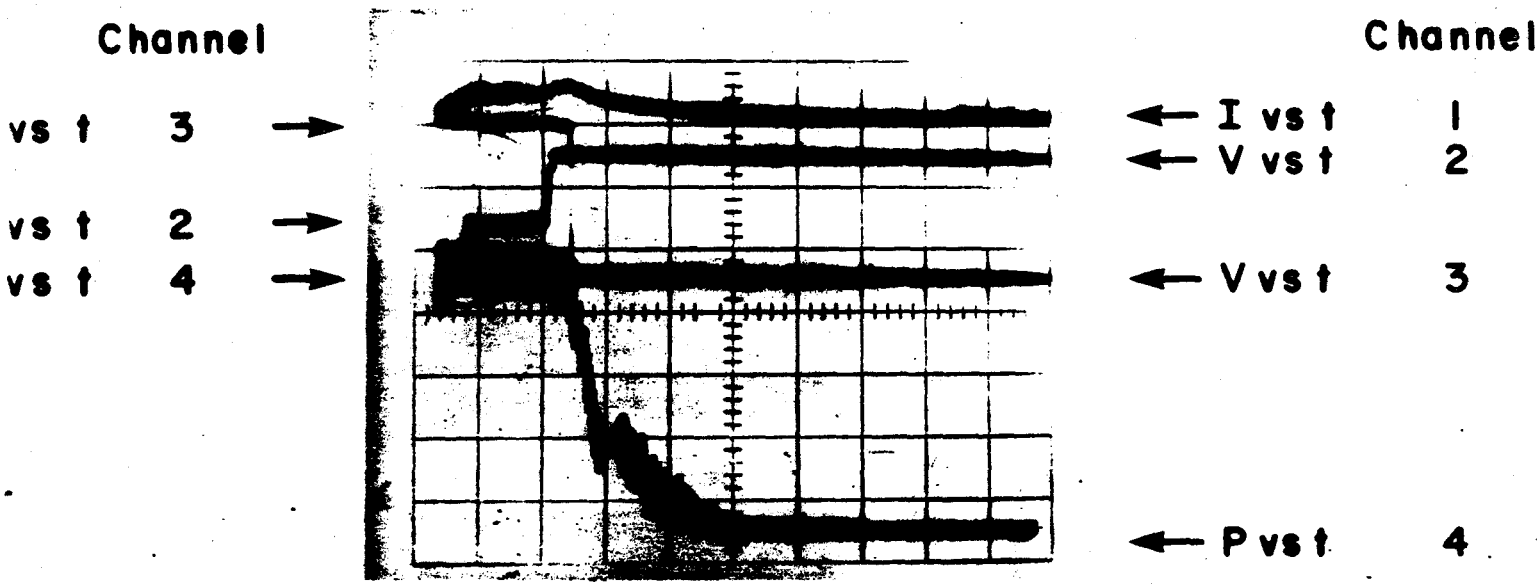

Scales		
	1	I = 1000 A/Div
	2	V = 80 μV/Div
	3	V = 1.0 V/Div
	4	P = 3.5 psig/Div
	t	20.48 s/Div

Fig. 6.10 Coil current, voltage, and pressure traces as a function of time during Event D.

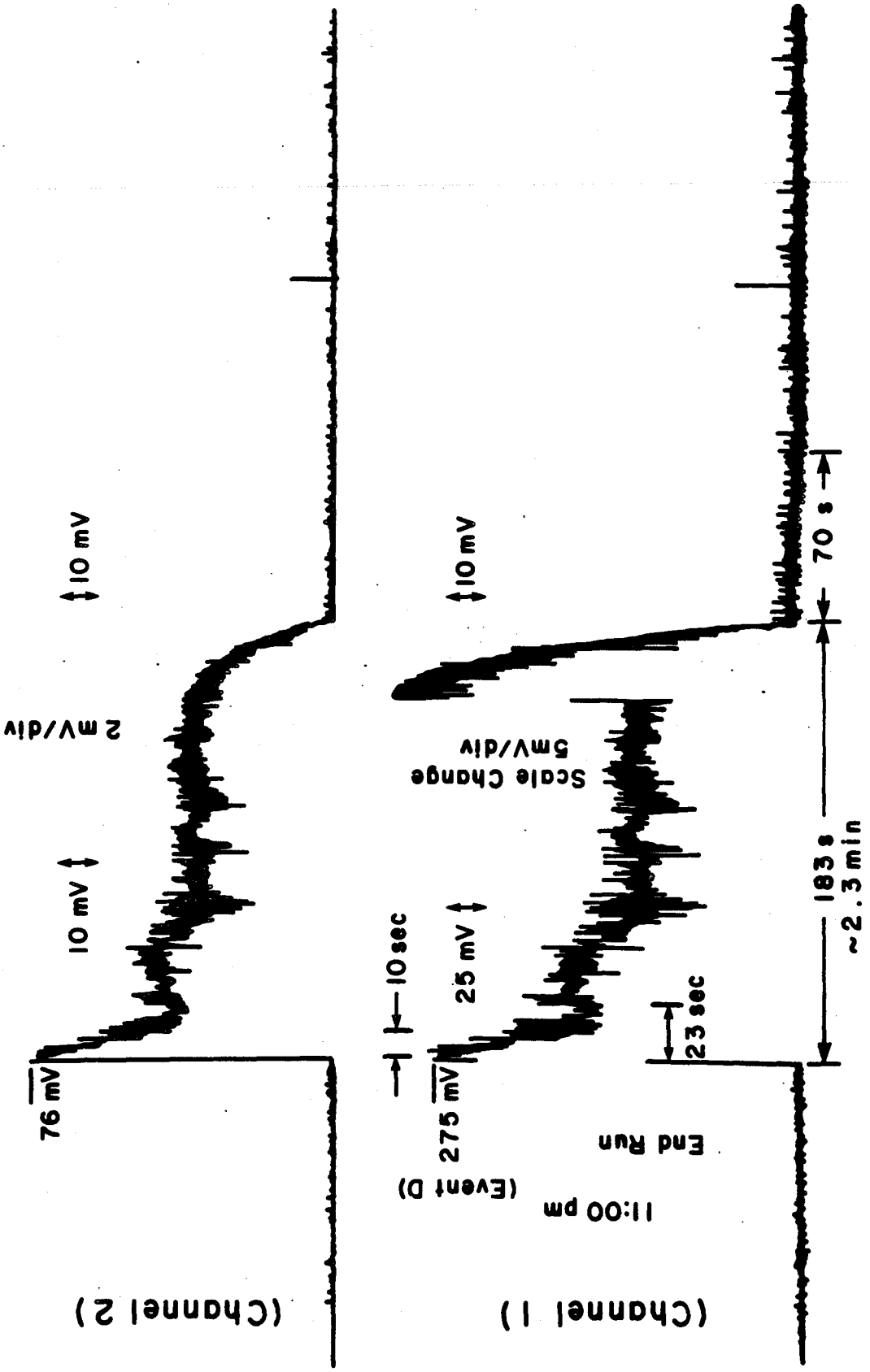

Fig. 6.11 Trace of voltage drop across the vapor-cooled current leads during Event D.

getting hot. After 35 seconds of heating, the scale was changed for Channel 1. After an additional 120 seconds (2 minutes) the voltage on both leads started rising rapidly, probably due to the total absence of helium coolant. The breakers were opened when the lead voltage hit 275 mV. At this point there was no more helium or magnet time remaining and the run was ended. The peak coil voltage was 2.4 volts at saturation of the Biomation scale which is on the order of the current supply limiting voltage.

Immediately following the end of the run, the coil was pulled from the dewar and examined for damage. Although none was visible there was a strong odor of burnt epoxy. Careful examination on the bench after the coil was warm indicated melted solder and burnt epoxy at a voltage tap B which is located at the helium inlet side of the coil just where it disappears beneath the retaining plate. This side of the coil is connected to the vapor-cooled lead on Channel 1 which was the hotter of the pair. The solder used was 50Pb-50Sn which melts at 414^{0} F (485 K). This fixes a minimum temperature at this point. There was no other observable physical damage and resistance checks of the coil and leads indicated no permanent damage.

Section 6.2 of this report describes an experiment that was specifically designed to damage the ICCS conductor by excessive joule heating.

6.1.4 Summary and Conclusions

A small football-shaped coil wound with ICCS conductor was tested in order to measure current, voltage, and pressure during a quench. Also, an attempt was made to determine failure modes by quenching the coil without replenishing the liquid helium. The critical current as a function of magnetic field was measured and agreed well with the most recent previous data. This indicated no degradation occurred due to handling.

During the quench tests the coil pressure appeared to reach steady-state values. This could have been due to either steady-state thermal equilibrium or pressure relief through the cold helium leak. The pressure relief valve was set at 100 psig and should not have affected this result. The maximum pressure was calculated to be 59 psia which is within a factor of 2 of the extrapolated maximum measured pressure of 34 psig. This is a very good agreement, especially considering the problems with helium leaks. It indicates that the simple expression for maximum pressure rise during a quench should be a relatively good tool for design of superconducting coils wound with cable-in-conduit conductors.

Classic pressure oscillations due to a thermal gradient in the pressure sensor tube were observed. Since this tends to reduce the measurement sensitivity, as well as increase the heat leak, any future tests should be performed with cold pressure transducers if at all possible.

An attempt was made to cause the conductor to burn out by keeping the coil energized at approximately 1100 A after a quench was initiated. However, as the conductor heated up, the coil resistance increased with

temperature thus causing the coil voltage to increase at constant current. Unfortunately the power supply could not provide enough voltage to maintain a constant current and thus the joule heating energy input was insufficient to drive the conductor to the melting temperature, approximately 1380 K. The available power supply could only furnish about 3 volts maximum while a required voltage of 8-10 volts was calculated. This coil was fail-safe in this sense but this is an artificial situation because it was wound noninductively. A real coil could have enough inductance and stored energy to actually burn out the conductor with the inductive voltage driving the current.

6.2 ICCS Termination - J.V. Minervini and W. Beck

Part of the experiment described in the previous section was intended to try to damage the ICCS conductor. However, it was determined that the impedance mismatch between the power supply and the test coil rendered the supply incapable of damaging the conductor by burnout. Another experiment was developed specifically to achieve the goal of conductor burnout by joule heating while monitoring the current and voltage history of the sample.

6.2.1 Sample Termination

It appeared that the most vulnerable portion of an ICCS coil was near the conductor termination where current must be transferred between the superconducting cable and the current leads and liquid helium must be brought from an external tube to parallel flow within the ICCS conduit. A sample ICCS termination of a subsize conductor was fabricated and instrumented in order to measure burnout characteristics. The conductor was identical to that described in the previous section (Table. 6.1 and Fig.

6.1) except for the sheath which was round and made of Incoloy 903, a high nickel superalloy. Figure 6.12 shows a photograph of a termination before the electrical and fluid connections were made. It was made by removing the outer sheath from the conductor ends, swaging the bare cable into copper tubes for current transfer and welding the tee block to the sheath and copper tube through transition pieces. The completed test section is shown in Fig. 6.13 with the current transfer blocks and voltage taps in place. The conductor was heated to 750 C for 30 hours to form Nb_3Sn filaments, even though the sample was never energized in the superconducting state. This reaction was carried out so that the electrical and thermal properties of the component materials were truly the same as those in a real coil which must undergo high temperature activation.

The helium connection was not completed nor was any helium used during the experiment since the objective was to burn out the conductor in a relatively adiabatic environment. There would be little difference between a helium or an air environment since convective heat transfer is negligible. In a real coil there would be an additional energy input required to raise the conductor from helium temperature (4.2 K) to room temperature but this amount was calculated and was small relative to the change in enthalpy of the conductor between room temperature (300 K) and burnout (~ 1380 K for copper).

6.2.2 Experimental Set-Up

A schematic of the experimental set-up is shown in Fig. 6.14. The sample was energized with the same power supply that was used for the previous small football coil test. However, this sample was designed so that the maximum resistive voltage was within the power supply limit of about

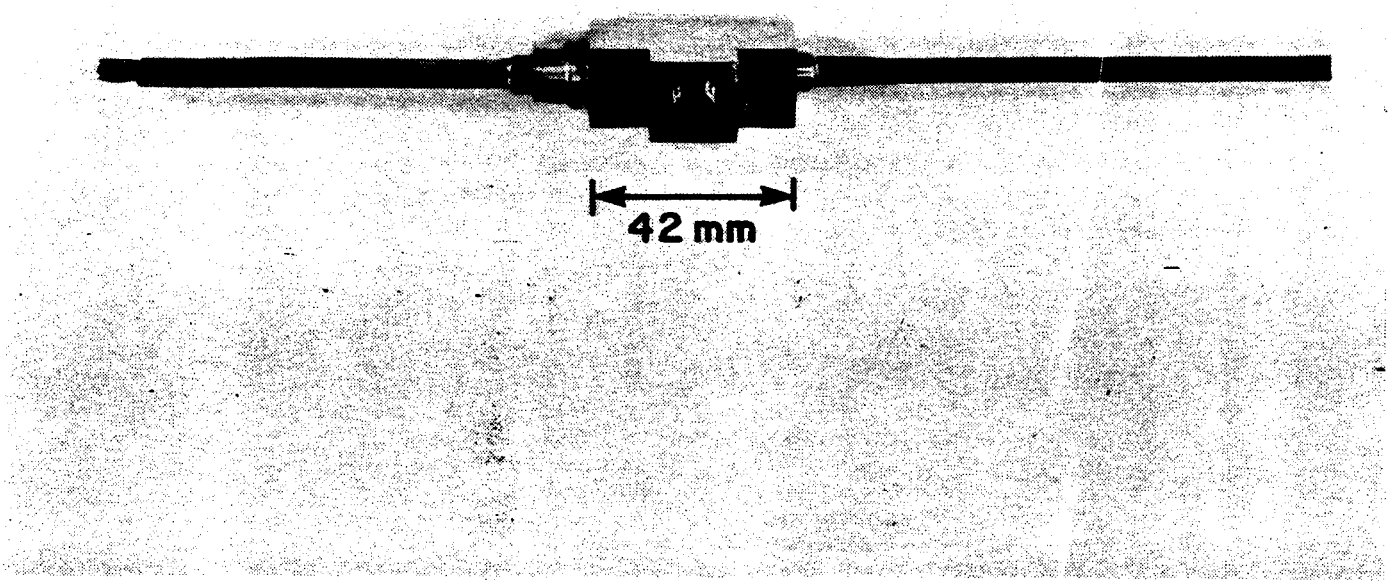

Fig. 6.12 Termination Assembly

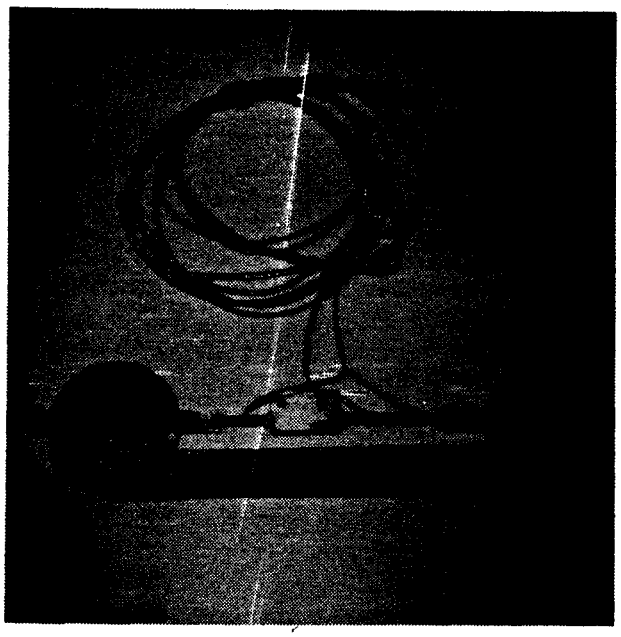

Fig. 6.13 Termination test section with copper current transfer block and voltage taps attached.

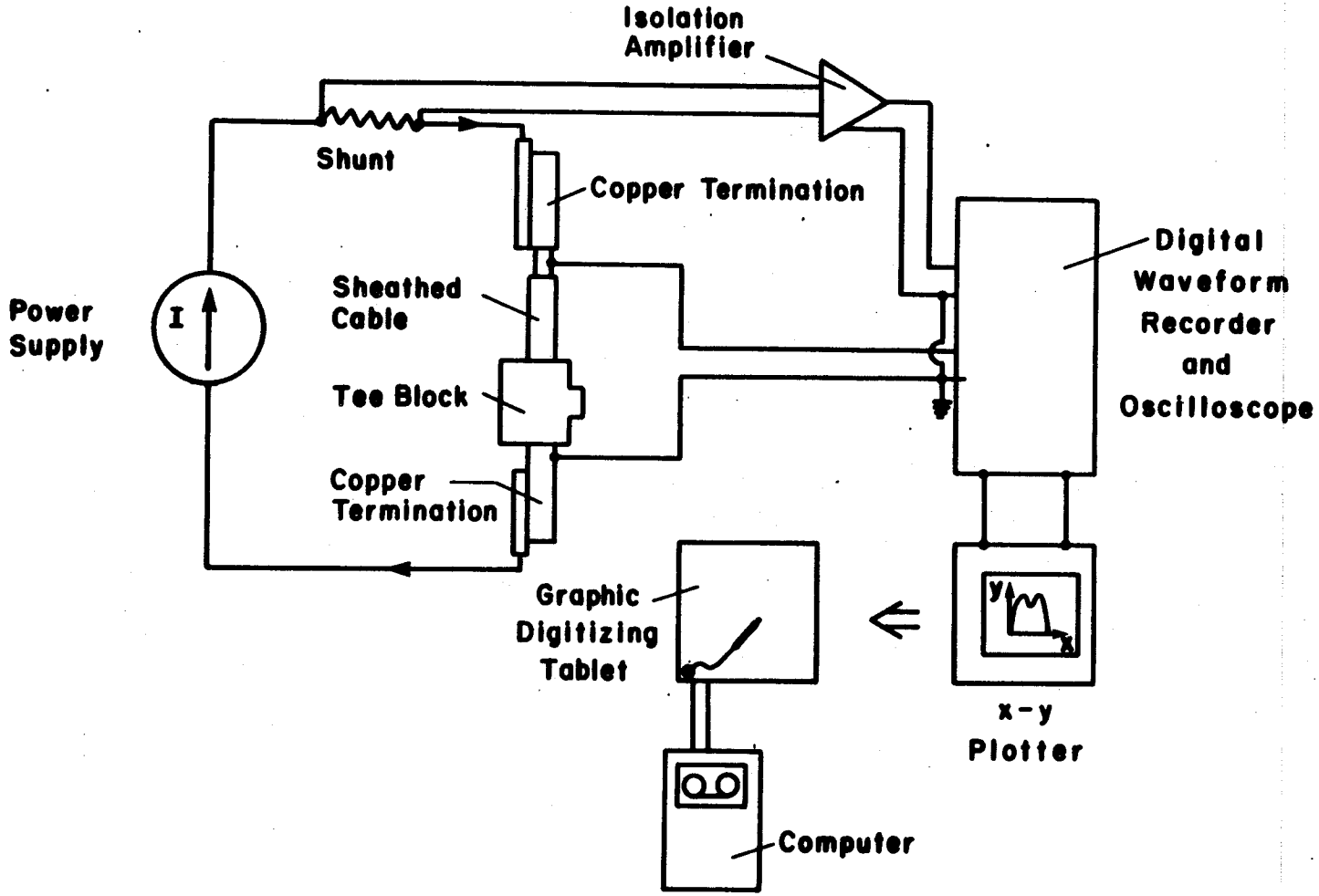

Fig. 6.14 Schematic of experimental set-up for ICCS termination test.

3 volts. Current through the sample was monitored by measuring the voltage across a shunt and sample voltage was monitored by taps across the test length between the current transfer blocks. The initial room temperature resistance of this length was measured to be 0.34 mΩ.

The current and voltage signals were recorded on a digital waveform recorder. After the signals were recorded, the data was saved by photographing the oscilloscope traces and by outputting the data to an X-Y plotter. The plotter traces were later digitized on a graphic digitizing tablet and transferred to a computer for data analysis.

6.2.3 Energy Calculations

If the heating of the conductor is relatively rapid a simple energy balance computation can be made to determine the amount of energy and time required to bring the conductor to the burnout temperature. The model assumes the joule heating energy is input adiabatically. Since the heat transfer by convection to stagnant air is relatively poor, the dominant heat transfer mechanism should be thermal conduction through the ends of the cable to the large copper current transfer blocks which also act as heat sinks. The time constant for thermal diffusion, τ_c, can be estimated from

$$\tau_c = \frac{\ell^2}{\alpha}$$

where ℓ is the half-length of the heated section (~ 7.6 cm) and α is the thermal diffusivity of copper (~ 1.0 cm^2/s). The time for significant heat transfer by this mechanism then is approximately 58 seconds. The adiabatic model should hold as long as the time to burnout is less than this value.

The simplest adiabatic heating model assumes that all the joule energy goes solely into the change of enthalpy of the copper in the conductor. The energy balance equation for a differential energy change is

$$\rho_c J^2 dt = \gamma_c C_{pc} dT \tag{6.1}$$

where

J = current density in the conductor (A/cm^2)

ρ_c = electrical resistivity of copper (Ω-cm)

γ_c = density of copper (g/cm^3)

C_{pc} = specific heat of copper (J/g)

t = time (seconds)

T = temperature (K).

A parameter G can be defined by lumping together the temperature dependent variables in Eq. 6.1 and integrating over time to get

$$G = \int_0^t J^2 dt = \int_{T_i}^{T_f} \frac{\gamma_c C_{pc}}{\rho_c} dT \tag{6.2}$$

where T_i and T_f are the initial and final temperatures respectively. Figure 6.15 shows G plotted versus the final temperature for copper with magnetic field as a parameter. The factor G is 1.2×10^9 for copper between 300 K and 1380 K. If the current flows solely in the copper cable at a constant value of 1000 amperes then the time to burn out the cable can be computed to be approximately 12 seconds. This should be a minimum value because some of the current could be carried by the sheath, thereby lowering the current density. Also, some of the heat energy goes into raising the enthalpy of sheath and some energy is conducted out the ends of the cable.

The simplest adiabatic heating model assumes that all the joule energy goes solely into the change of enthalpy of the copper in the conductor. The energy balance equation for a differential energy change is

$$\rho_c J^2 dt = \gamma_c C_{pc} dT \tag{6.1}$$

where

J = current density in the conductor (A/cm^2)

ρ_c = electrical resistivity of copper (Ω-cm)

γ_c = density of copper (g/cm^3)

C_{pc} = specific heat of copper (J/g)

t = time (seconds)

T = temperature (K).

A parameter G can be defined by lumping together the temperature dependent variables in Eq. 6.1 and integrating over time to get

$$G = \int_0^t J^2 dt = \int_{T_i}^{T_f} \frac{\gamma_c C_{pc}}{\rho_c} dT \tag{6.2}$$

where T_i and T_f are the initial and final temperatures respectively. Figure 6.15 shows G plotted versus the final temperature for copper with magnetic field as a parameter. The factor G is 1.2×10^9 for copper between 300 K and 1380 K. If the current flows solely in the copper cable at a constant value of 1000 amperes then the time to burnout the cable can be computed to be approximately 12 seconds. This should be a minimum value because some of the current could be carried by the sheath, thereby lowering the current density. Also, some of the heat energy goes into raising the enthalpy of sheath and some energy is conducted out the ends of the cable.

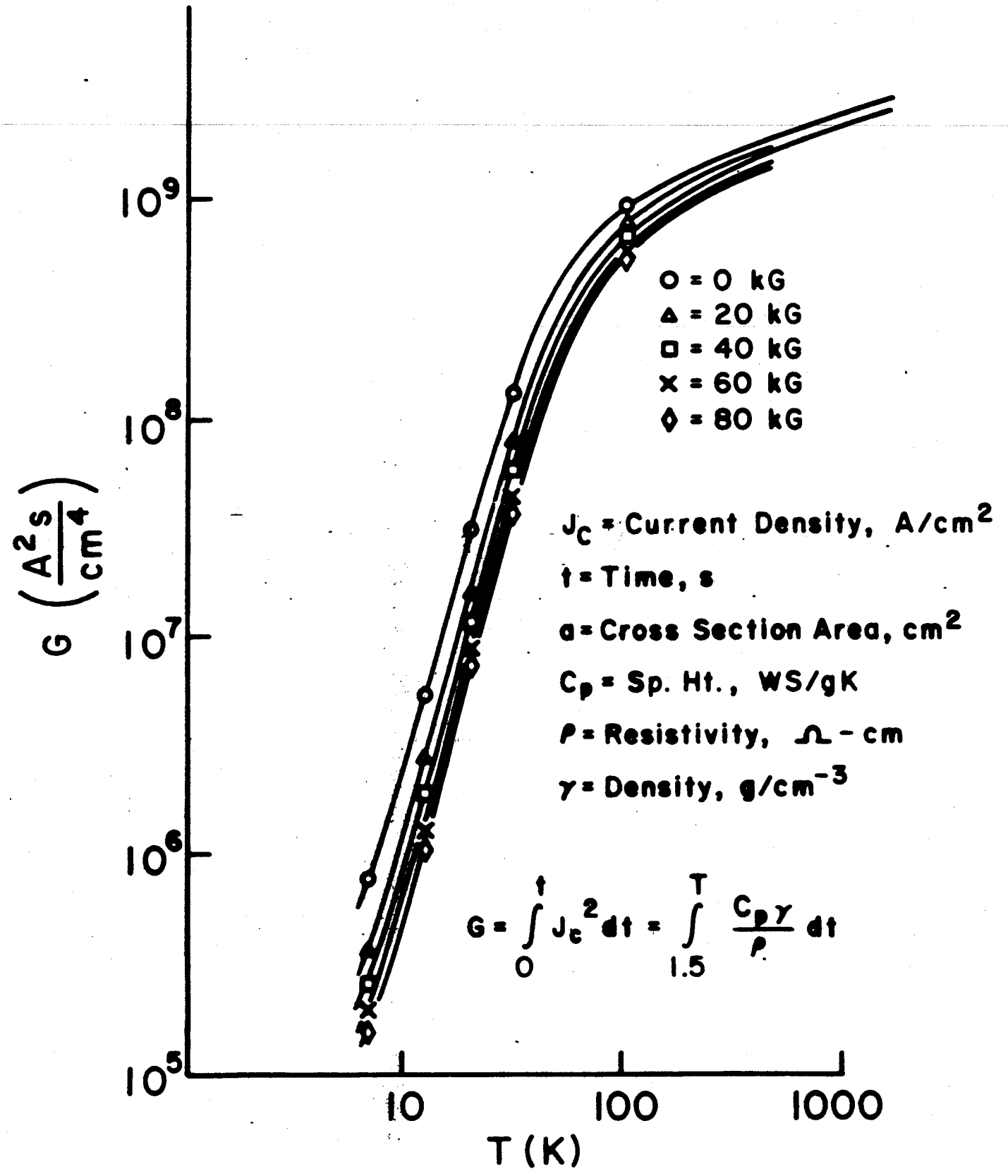

Fig. 6.15 Adiabatic heating of copper.

6.2.4 Test Results

Figure 6.16 shows the conductor current and voltage as a function of time. The current was ramped up to approximately 1000 amperes. When the voltage was held constant the current dropped back because the cable resistance increased with the higher temperature caused by the joule heating. Figure 6.17 shows the conductor resistance versus time history. The current was brought back to 1000 amperes. The voltage required to maintain this current increased to the point where the power supply could not quite keep up with the constant current requirement. At this point the cable burnt out, as is indicated by the sudden increase in resistance and voltage, while the current dropped to zero. The total time that elapsed from initial energization to burnout was 35 seconds with the current approximately constant at an average value of 950 amperes for about 18 seconds. A plot of the instantaneous power dissipated as a function of time is shown in Fig. 6.18.

A photograph of the termination after burnout is shown in Fig. 6.19. It shows that both the cable and the sheath burned completely through. This proves that a significant amount of energy went into the sheath. The total energy dissipated was computed from the time integral of the power curve (Fig. 6.18) to be 18.1 kJ, and the actual factor G (Eq. 6.2) was computed to be 2.1×10^9. The difference between this value and the estimated value can be attributed to the presence of sheath material.

6.2.5 Discussion and Summary

An ICCS termination was fabricated and tested to investigate failure behavior due to conductor overheating. The conductor was energized to 1000 amperes at room temperature and burned through in 35 seconds. The

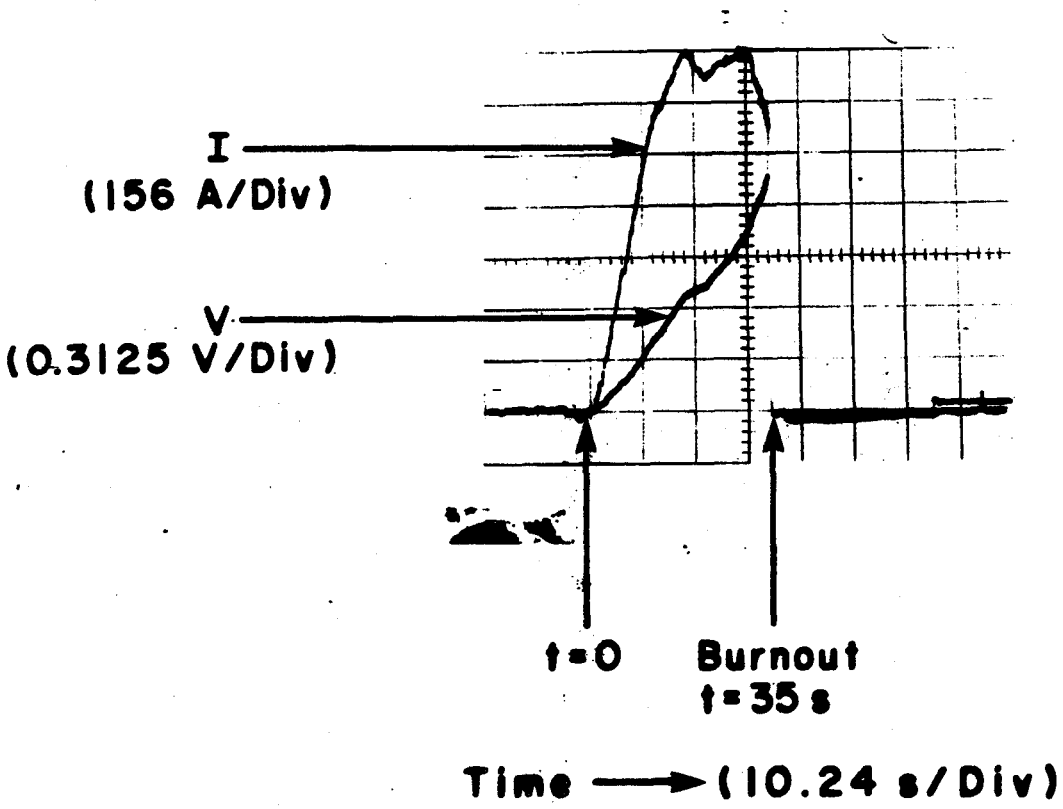

Fig. 6.16 Oscilloscope traces of conductor current and voltage versus time.

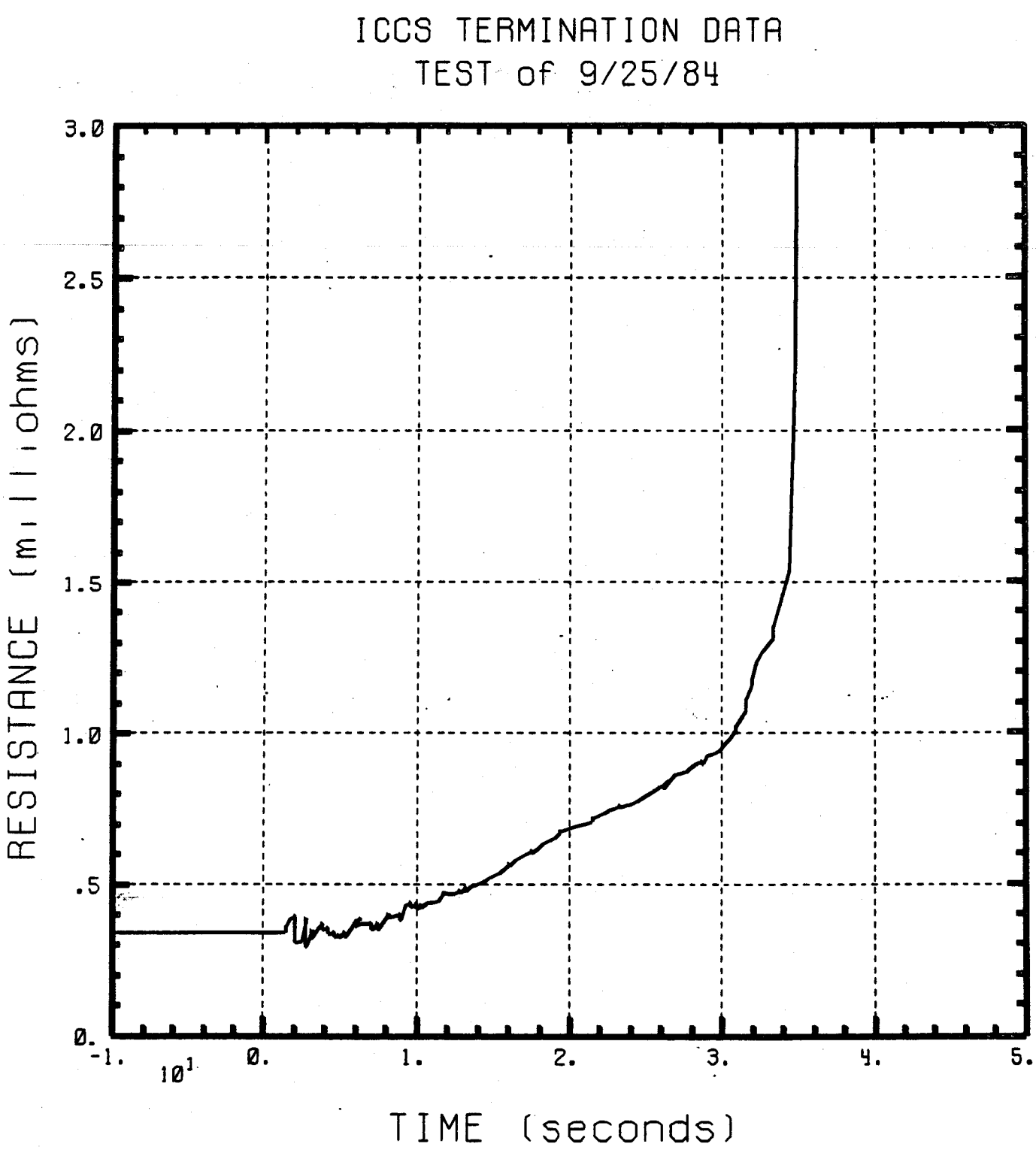

Fig. 6.17 Conductor resistance versus time.

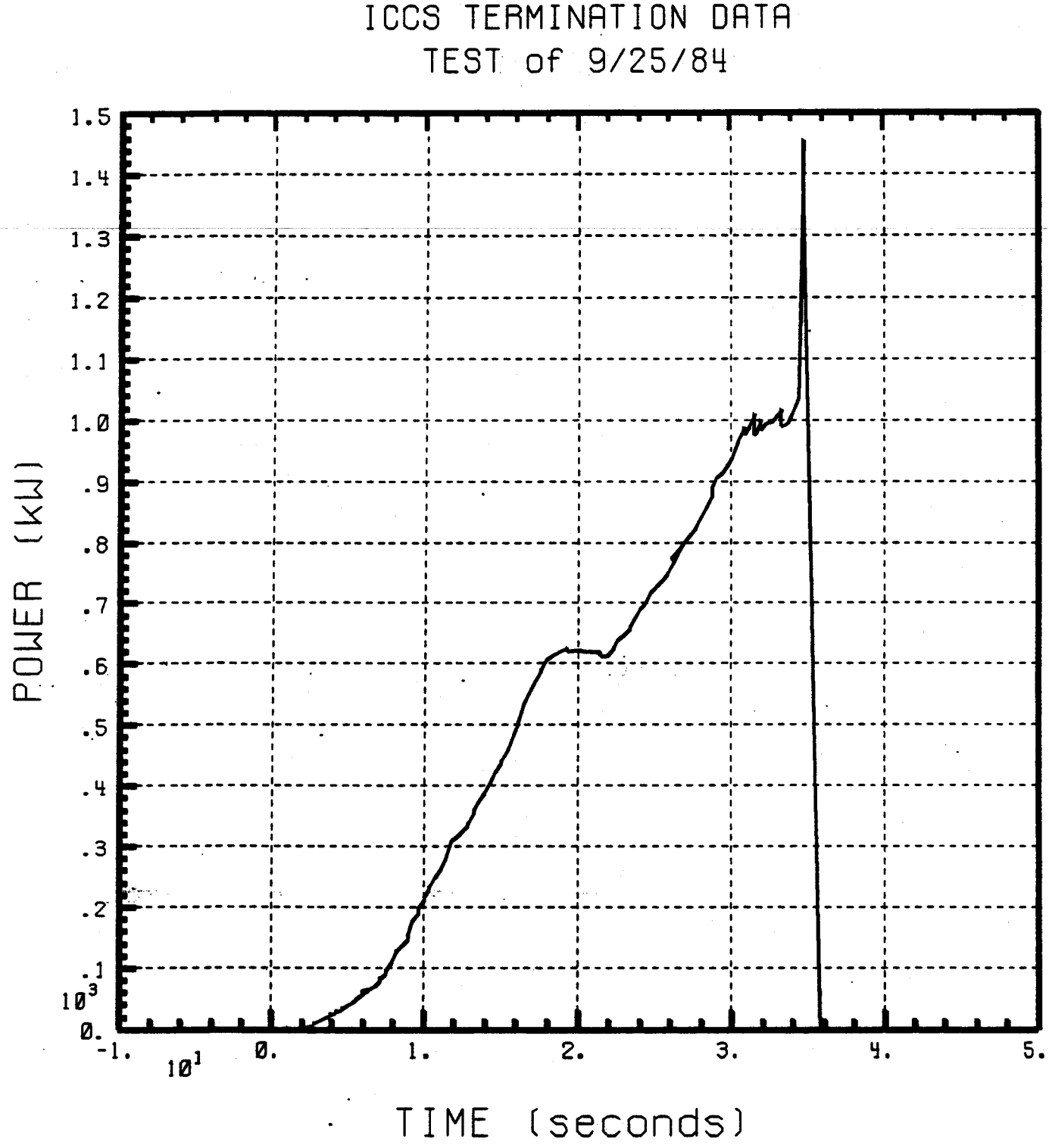

Fig. 6.18 Power dissipated versus time.

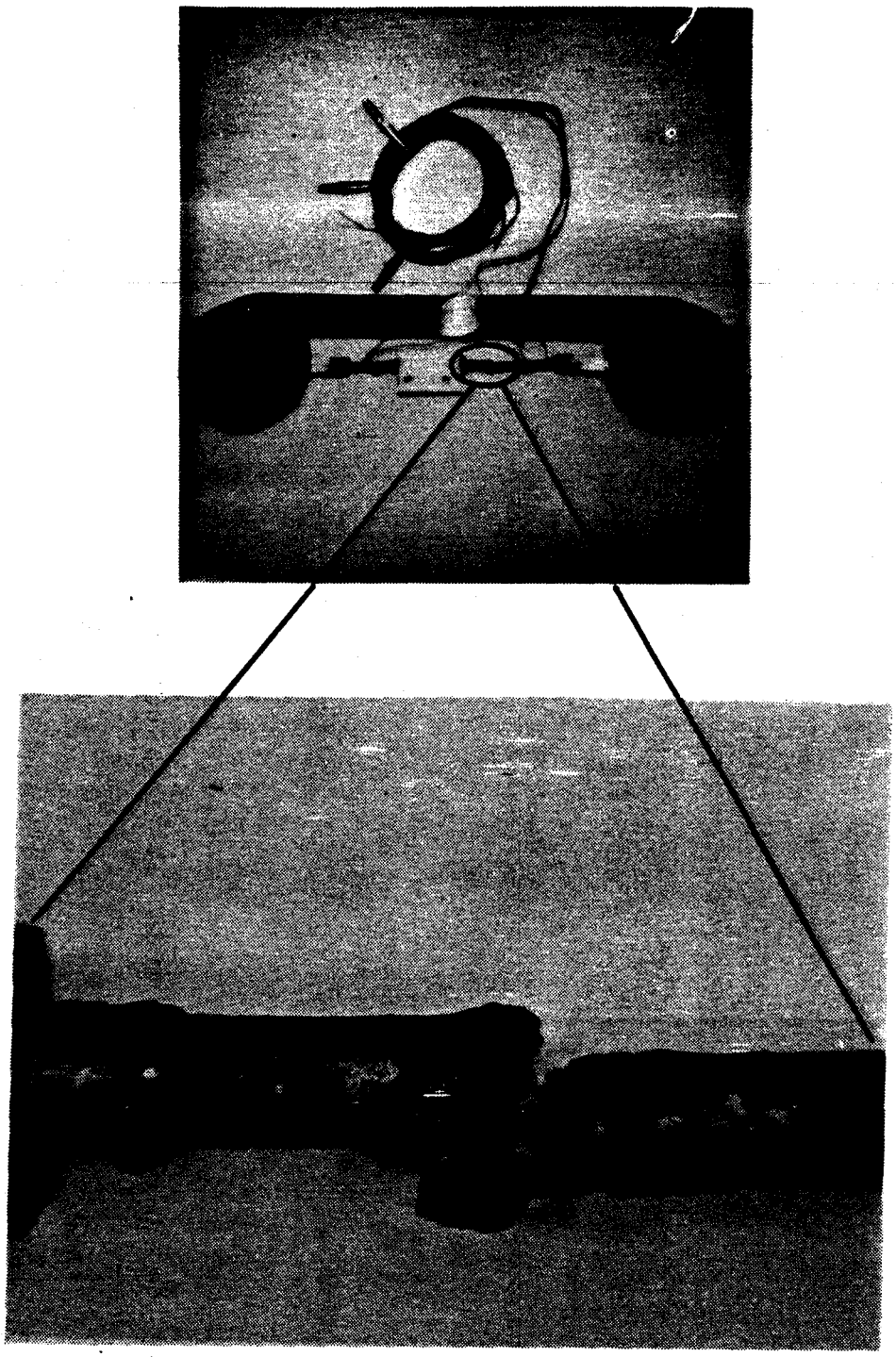

Fig. 6.10 Termination test section after burnout showing cable burned completely through.

conductor failed in the middle of the sheathed section between the tee block and current bus connection. This should be expected to be the weakest point in the test section because it is furthest away from low current density current bus connections and the extra heat capacity of the helium tee block steel. The implication for a real superconducting coil is that current burnout would probably occur between tee block and the beginning of the coil winding, since this section would probably have the least heat capacity and the highest current density in the coil.

The adiabatic heating curve for copper (Fig. 6.15) was used to estimate the time to burnout and was found to be within a factor of 2 of the actual value. The discrepancy can be attributed principally to the presence of the sheath material and implies that all materials that have significant heat capacity or current sharing capability, and are in close contact with the conductor, should be included in the computation. Then the adiabatic heating curve for copper and/or other materials should be a relative good predictor of conductor heating behavior.

6.3 References for Section 6

1. R.J. Thome, et al., "Safety and Protection for Large Scale Superconductivity Magnets - FY83 Report, MIT Plasma Fusion Center Report No. PFC/RR-83-33, December 1983, pp. 111-117.

2. J.R. Miller and J.W. Lue, "Designing Internally Cooled Superconductors for use in Large Magnets," Proceedings of the Workshop on Stability of Superconductors in Helium I and Helium II, Saclay, France, November 16-19, 1981, pp. 247-254, International Institution of Refrigeration, Refrigeration Science and Technology.

3. P. Thullen and J.L. Smith, Jr., "Model for Thermally Sustained Pressure Oscillations Associated With Liquid Helium," Advances in Cryogenic Engineering, Vol. 13, pp. 215-222, Plenum Press, N.Y. 1968.

4. T. Yazaki, A. Tominaga, and Y. Narahara, "Large Heat Transport Due to Spontaneous Gas Oscillation Induced in a Tube With Steep Temperature Gradients," Journal of Heat Transfer, November 1983, Vol. 105, pp. 889-894.

7.0 LABORATORY LIQUID HELIUM DEWAR FAILURE - J.V. Minervini and R.J. Thome

Liquid cryogens are required to maintain superconducting magnets in the superconducting state so it is not unusual to find large dewars of liquid helium and liquid nitrogen located in experimental areas and laboratories where superconducting devices are operated. It is more unusual, however, to hear reports of significant dewar failures.

On March 19, 1984 the Francis Bitter National Magnet Laboratory experienced a major dewar failure in one of the laboratory rooms. This section describes that dewar failure, its probable causes, and some safety precautions that should always be taken. In addition, a thermodynamic analysis of dewar pressurization is given that provides insight into the fundamentals of safe dewar operation.

7.1 Dewar Failure

The dewar that failed was a typical, transportable, 25 liter liquid helium storage dewar. A simplified cross section of the dewar is shown in Fig. 7.1. The principal components are the spherical helium vessel, the spherical annular liquid nitrogen shield and an outer spherical vacuum shell. These components are all suspended from a thin wall neck. They are fabricated from copper hemispheres and the halves joined by solder at the equator. An outer stainless steel casing protects the inner vessels from mechanical damage. The annular gaps between the spherical shells are evacuated and filled with aluminized mylar superinsulation. The sketch in Fig. 7.1 shows a helium pressure gauge and pressure relief valve but these were not present on the dewar that failed. The absence of these safety

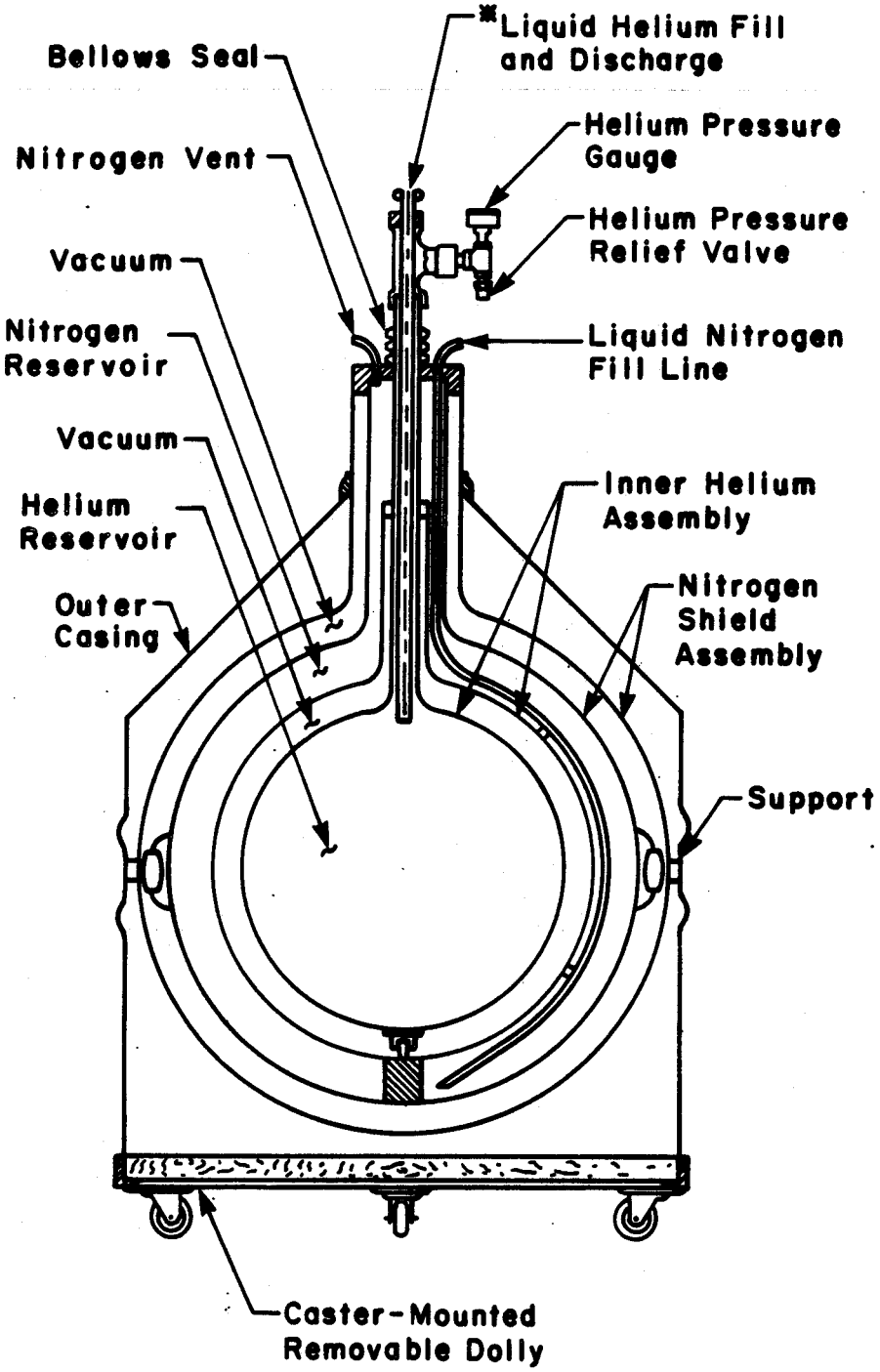

* Standard Opening 5/8" O.D. x 0.020" Wall
Larger Neck Openings Available on Special Order

Fig. 7.1 Simplified cross section of liquid helium dewar.

devices is not uncommon on many of these dewars. The dewar sits on a frame with casters so it can be easily rolled around.

The dewar was sitting in a laboratory and exploded during the middle of a work day. It was totally destroyed and there was significant damage to the room. The room was unoccupied at the time of the explosion. Figure 7.2 shows a photograph of the dewar and Fig. 7.3 shows a photograph of the room after the explosion. The damage to the dewar was complete, with all of the spherical shells being broken either by failure at the hemispherical solder joint or by actual tearing of the metal.

Most of the damage to the room occurred because the dewar separated into two halves with the top half projected vertically up into the ceiling and the bottom half driven into the floor. The main projectiles were vertical because the weak seam was horizontal. Thus, most of the damage was limited to a cylindrical volume about 8 feet in diameter between the floor and the ceiling. Most of the room damage derived from the dewar tearing out a cable tray and flourescent light fixture above with the reaction force driving the casters into the linoleum floor below.

The probable cause of the failure was an ice blockage in the dewar neck. The normal method of pressure venting in these dewars is by pressure buildup lifting off a brass plug that sits on top of the fill and discharge tube. This plug should always be in place except when a transfer tube is inserted for filling or discharging. When the plug is left out, the ambient temperature air fills the neck tube, condenses on the cool tube walls and freezes. Eventually, enough air can freeze to completely block the neck. The steady-state heat leak into the closed helium

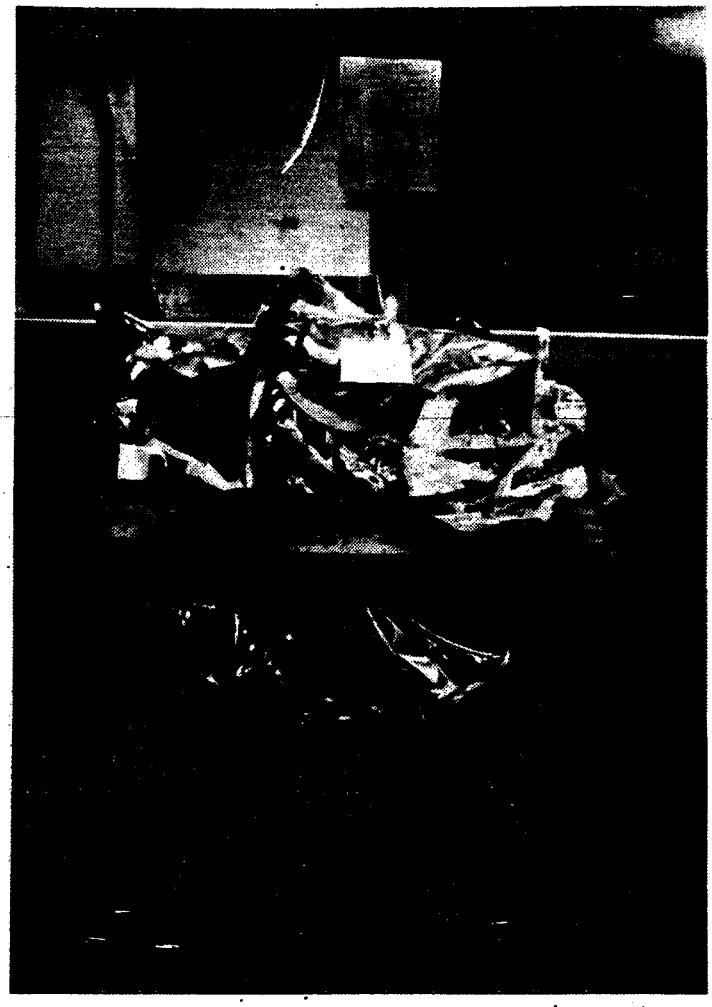

a)

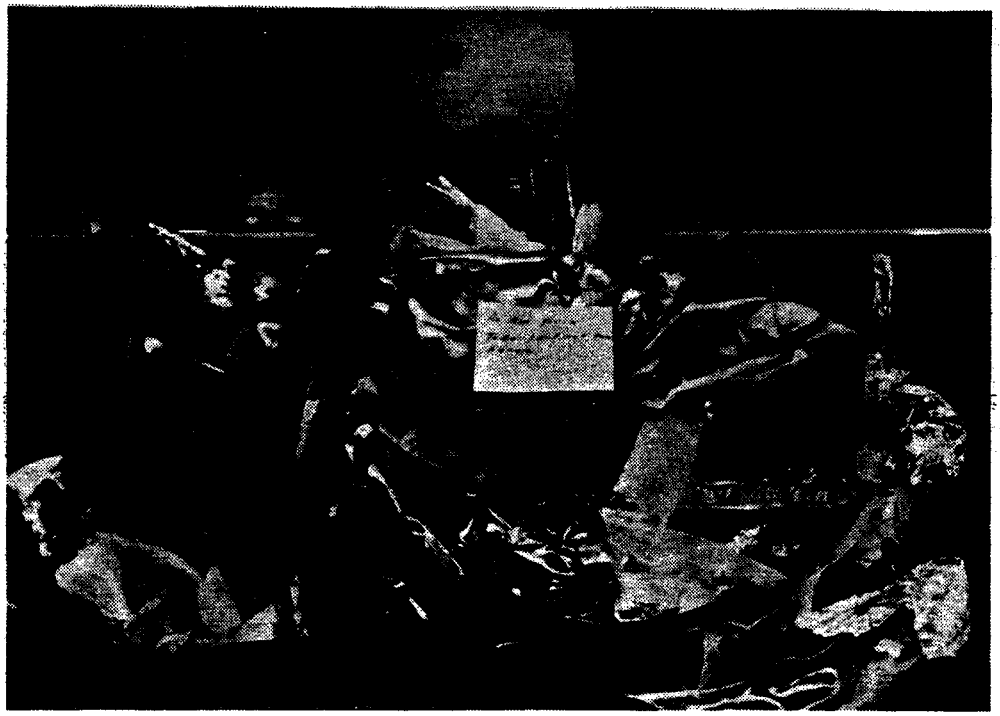

b)

Fig. 7.2 Two views of dewar after explosion showing
(a) copper shells and stainless steel outer jacket, and
(b) close-up of inner copper shells and superinsulation.
Note the separated solder joint.

Fig. 7.3 View of dewar and laboratory damage after explosion. The inner copper shells and overhead cable tray are visible.

volume drives up the pressure. The next section contains a thermodynamic analysis of this situation. Without pressure relief, either through a relief valve or burst disk, the pressure will continue to build up, with possible failure resulting, as happened in this case. The time required to completely plug up the neck with freezing air can be deceptively short and is a cumulative process between dewar warm-ups or neck reaming.

Several safety precautions may be taken to prevent such accidents. These precautions include:

(1) keep neck plug in place except when transferring helium,

(2) maintain liquid nitrogen in shield (suggested interval 3 days or less),

(3) check for ice blockage in neck of any dewar left unused for 2 to 3 days,

(4) ream dewar neck on a regular basis (every day or so).

These procedures should be followed for all small laboratory dewars but they are particularly important for dewars that do not have pressure relief valves or burst disks.

7.2 Thermodynamic Analysis of Pressurized Dewars

If a dewar is unvented, either by design or accident, the thermodynamic analysis of the pressure rise becomes quite simple. Assume that the thermodynamic system consists of a mass of helium inside a closed tank and that the initial state is two-phase helium at a temperature of 4.2 K and 1 atmosphere pressure, with a vapor volume fraction of specified value x. Then any heat energy that leaks into the dewar goes into raising the internal energy of the helium. The temperature and pressure at any time after the dewar is sealed is determined by the total amount of energy per

unit mass input to the system and the initial vapor volume fraction. This is illustrated in Fig. 7.4 which was generated from the thermodynamic properties of helium.[1] As an illustration, note that a vessel which is initially full of liquid, x = 0, will experience a relatively large increase in pressure for a relatively small heat input per unit mass. Hence, it is not desirable to fill a container completely and then seal it. Of course, the purpose of the dewar is to carry liquid helium, so it suggests leaving a small amount of ullage, that is, x may be small, but must be nonzero for safety.

Another simple analysis can be done to determine burst disk dimensions for limiting the maximum pressure in the dewar. A preliminary analysis may be carried out by assuming that during a sudden energy input the pressure inside the dewar becomes greater than 2.05 times the pressure outside the vessel. The flow will then be sonic at the point of minimum area in the vent or burst disk and the flow rate will be determined on this basis.

The mass flow per unit area under these conditions is:

$$\frac{W}{A} = \sqrt{\frac{k}{R}\left(\frac{2}{k+1}\right)^{\frac{k+1}{k-1}}}\;\frac{P_o}{\sqrt{T_o}} \qquad (7.1)$$

W = mass flow rate
A = cross-sectional area of vent passage
k = ratio of specific heats
R = gas constant
P_o = stagnation pressure
T_o = stagnation temperature

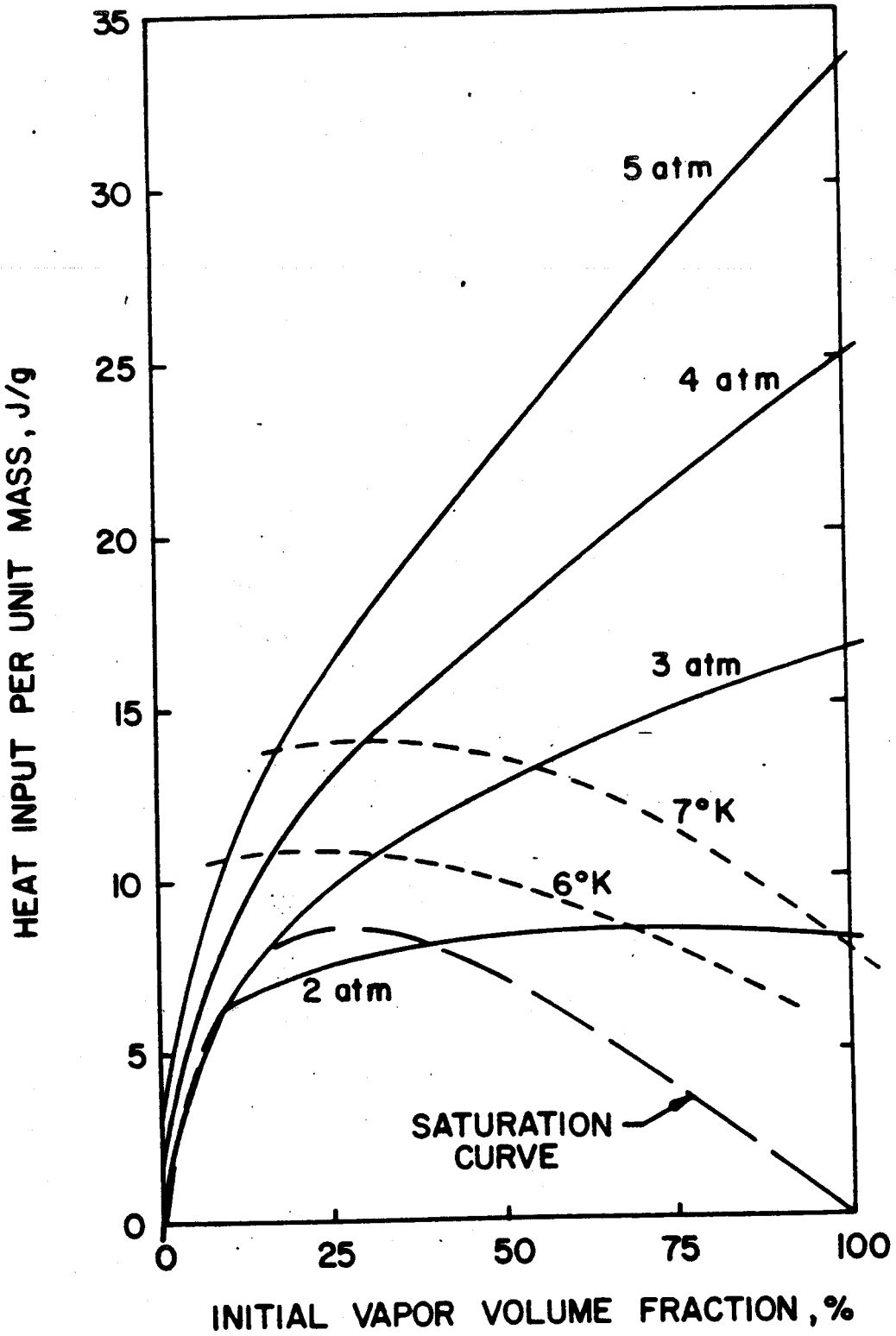

Fig. 7.4 Temperature and pressure in a container filled with enough liquid helium to reach a given vapor volume fraction, then sealed at 15 psia and subjected to a given total heat input per unit mass.

We can express W in terms of the gas produced and by an equivalent number of liters of liquid helium being vaporized. In these terms, the above formula can be simplified to the following for helium:

$$\frac{W}{A} = 30.2 \frac{P_o}{\sqrt{T_o}} \qquad (7.2)$$

W = liters of liquid helium per second which are vaporized and vented
A = cross-sectional area ($in.^2$)
P_o = stagnation pressure (psi)
T_o = stagnation temperature (K)

If a pressure limit of 50 psi is chosen then:

W = 478 A at 10 K
W = 87 A at 300 K

This implies that (if the gas temperature is no higher than 10 K) a 1 $in.^2$ vent will exhaust 478 liters per second of vaporized helium. At 300 K this drops to 87 liters per second. Both rates are adequate from the standpoint of safety and lower pressures may be had with larger vents.

The helium venting process may also be considered as the removal of energy from the system at a certain rate as illustrated in Fig. 7.5. The heat of vaporization of liquid helium is 2580 joules per liter of liquid. The latter weights 125 grams. The specific heat of helium gas is 2.32 joules/g K so that for the 125 g in a liter of liquid helium, the specific heat would be 290 joules/liter K.

The rate of energy removal from the system is then:

$$\frac{dQ}{dt} = W \left[2580 + 290 \, (T_o - 4.2)\right] . \qquad (7.3)$$

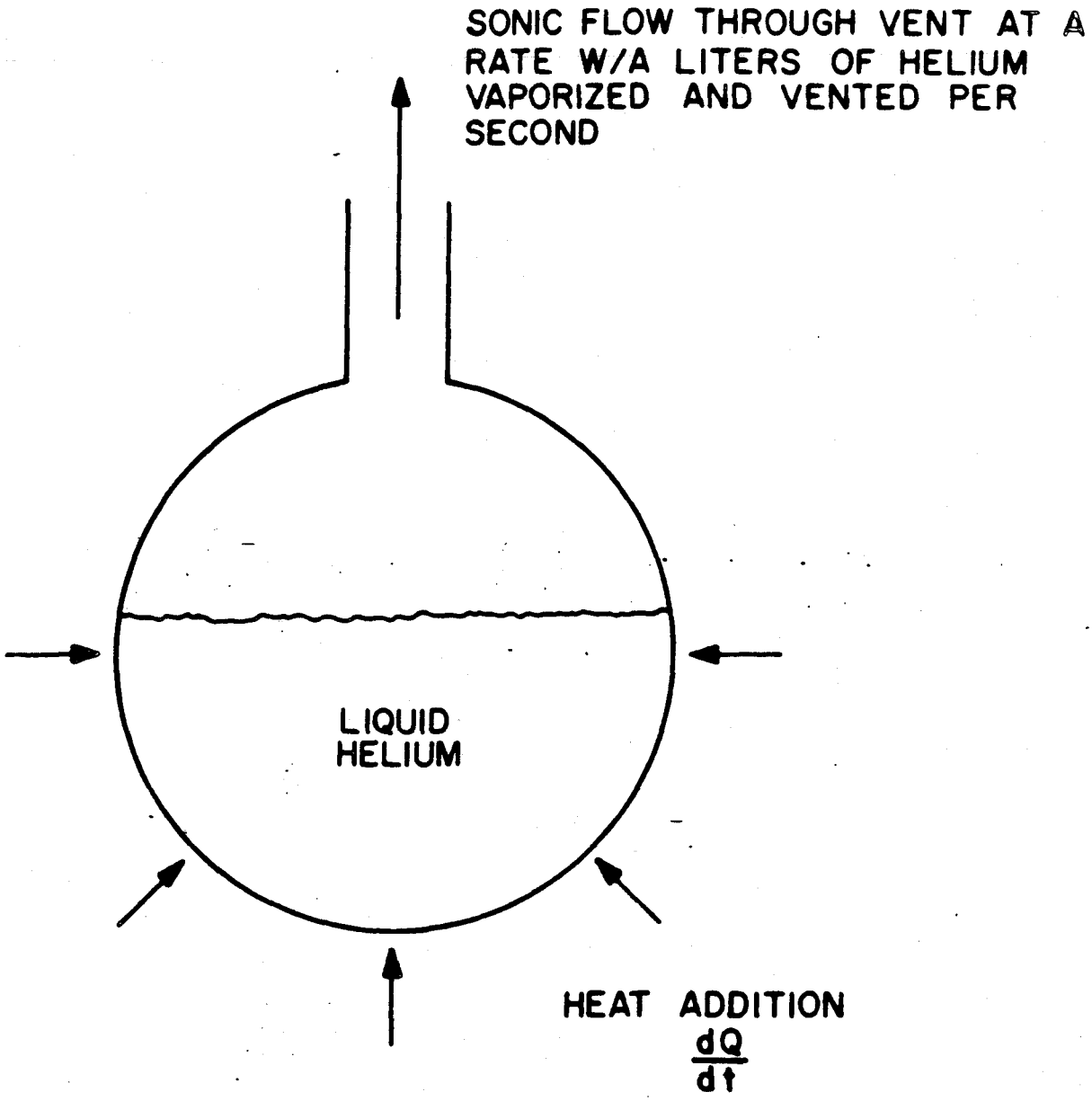

Fig. 7.5 Model of helium flow through burst disc for a given heat input rate.

where W is in liters of helium per second. Substitution for W from the previous equation gives:

$$\frac{1}{A}\frac{dQ}{dt}\frac{\text{WATTS}}{\text{in.}^2} = 30.2\,\frac{P_o\ (\text{psi})}{\sqrt{T_o(^oK)}}\left[2580 + 290\ (T_o(^oK) - 4.2)\right] \qquad (7.4)$$

This relationship is shown plotted for 30 and 50 psi dewar pressures as a function of T_o in Fig. 7.6. This figure indicates that each square inch of vent area is capable of venting several hundred kilowatts of heat generated in the cold area. For a 2×10^6 joule magnet transferring heat to the helium liquid for 10 seconds, a one square inch vent would be able to handle the boil off at an internal pressure of 30 - 50 psia.

While the above analysis is only approximate, it does show that relatively small vents can handle large amounts of heat influx into the low temperature region. Alternately, it can be concluded that overpressures can be kept to values of a few psi if desired, by using larger vent areas.

7.3 Summary

A small laboratory dewar suffered a catastrophic failure due to excess pressure buildup after an ice blockage closed off the vent area of the neck. This was the result of improper dewar usage. Some recommendations for safe operating procedures were given but these rules should be transmitted to laboratory personnel and reinforced on a regular basis.

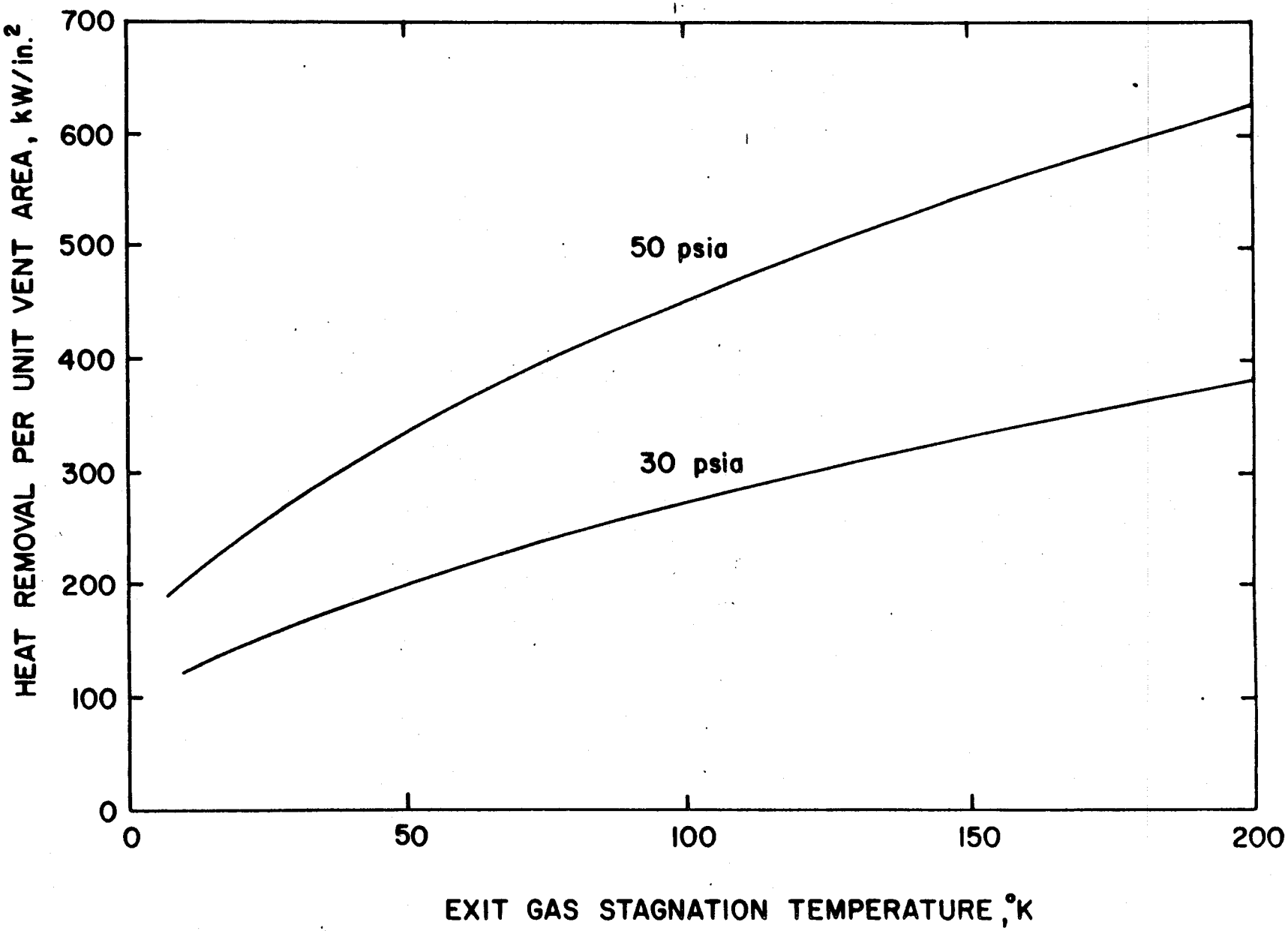

Fig. 7.6 Heat removed per unit burst disc area as a function of pressure rise in the container and stagnation temperature of the flow.

A simple thermodynamic analysis was developed in order to estimate maximum dewar pressures in a sealed system and burst disk size to gain insight into the fundamental requirements for safe operation. Manufacturers instructions and code requirements should, however, always be followed.

8.0 SAFETY RELATED ACTIVITIES - R.J. Thome

8.1 Publications

The following papers were published in FY84 and present work which was partially supported by the PFC contract monitored by INEL (DOE Contract No. DE-AC02-78ET51013).

1. R.J. Thome, J.M. Tarrh, R.D. Pillsbury, Jr., W.R. Mann and W.G. Langton, "Protection of Toroidal Field Coils Using Multiple Circuits," 10th Symposiuum on Engineering Problems of Fusion Research, Proceedings, IEEE Contract Number 83CH1916-6 NPS, Vol. 2, Philadelphia, Penn., December 1983, pp. 2059-2063.

2. R.J. Thome, R.D. Pillsbury, Jr., W.G. Langton and W.R. Mann, "Magnetic to Kinetic Energy Conversion Following Structural Failure," 1984 Applied Superconductivity Conference, to be published in IEEE Trans. Magnetics, MAG-21 (January 1985, Tentatively) San Diego, CA, September 1984.

8.2 MESA Subcontract

The MIT Plasma Fusion Center is under subcontract to MESA Corporation, Ogden, Utah to support their contract "Experience With Magnet Accidents." The period of performance for the MIT contract is February 1984 through February 1985.

As part of the activity, MIT has prepared a survey which was distributed to the major centers of magnet activity in the U.S. The purpose of the survey is to gather data on magnet failure experience and classify results. Results will be analyzed by MESA Corporation with the help of MIT and will be presented in a separate report.